

UNIVERSITY OF OKLAHOMA

GRADUATE COLLEGE

This is the thesis title

A DISSERTATION

SUBMITTED TO THE GRADUATE FACULTY

in partial fulfillment of the requirements for the

Degree of

DOCTOR OF PHILOSOPHY

By

YU-TING SHEN

Norman, Oklahoma

2018

This is the thesis title

A DISSERTATION APPROVED FOR THE
HOMER L. DODGE DEPARTMENT OF PHYSICS AND ASTRONOMY

BY

Dr. Patrick Skubic, Chair

Dr. Michael Strauss

Dr. Ron Kantowski

Dr. Deborah Watson

Dr. S. Lakshmivarahan

© Copyright by YU-TING SHEN 2018
All Rights Reserved.

'Blood, sweat & respect. First two you give, last one you earn.'

- Dwayne Johnson

Acknowledgements

I would like to thank everyone who have helped me.

Especially thanks to my advisor Patrick Skubic, SS/3L + jets analysis convenor Ximo Poveda Torres, and post doctor Judita Mamužić. Patrick gave me enough freedom and space to work on the project related to the analysis I was interesting in. He helped me to handle all the things related to the university when I based at CERN for the past three years. He also guided me, discussed with me on every Tuesday and Thursday, gave me a lot of useful feedback, and provided me the financial support for my entire Ph.D. life. Ximo is a very good mentor and friend while I was at CERN. When I got stuck in some technical parts in doing the analysis, Ximo always used his abundant experiences and knowledge to help me to solve the problem. Not only helping me in the research, Ximo also helped me to accommodate myself to the new life at CERN. Without Ximo's great help, I couldn't finish my dissertation smoothly and successfully. Judita kindly agreed to help me working on the NUHM2 interpretation in the Higgsino LSP research after I finished the study on the SS/3L + jets analysis. She used the experiences about the NUHM2 study, which she accumulated in Run 1 $\sqrt{s} = 8$ TeV, providing me many instructions about doing the NUHM2 analysis and writing the note and my dissertation. Especially, she spent a lot of time to prepare the NUHM2 compressed + compressed MC sample productions, to develop the script using HiggsinoFitter, to answer various

questions from the editorial board. With her supports, I can finish the NUHM2 study in a very short period.

Thanks to all my friends at CERN and OU for the good times we enjoyed together in exploring delicious food, traveling, hiking, bouldering, skiing, and boxing. Thanks to my ex-girlfriend to warm my heart, to encourage me, and to love me, making me felt happiness in the first half of my Ph.D. life. Thanks to my brother taking care of my parents when I am far away from Taiwan. Finally, many thanks to my parents for everything they bestowed on me.

Contents

	Page
List of Tables	ix
List of Figures	xii
1 Introduction	1
2 The Standard Model	5
2.1 The Standard Model of Particle Physics	5
2.1.1 Particle Content	6
2.1.2 Local Gauge Theory	9
2.1.3 Strong interaction	10
2.1.4 Electroweak interaction	11
2.1.5 The discovery of Higgs boson	16
2.2 Beyond the Standard Model	17
2.2.1 Hierarchy problem	18
2.2.2 Dark matter and dark energy	18
2.2.3 Grand Unification	19
2.2.4 More questions	20
3 Supersymmetry	21
3.1 Why supersymmetry	21
3.2 Introduction of the supersymmetry	24
3.2.1 Superalgebra	24
3.2.2 Superspace and superfields	26
3.2.3 <i>R</i> -parity	28
3.2.4 Supersymmetry breaking	28
3.2.5 The Minimal Supersymmetry Standard Model	29
3.3 The radiative natural SUSY	30
3.4 The non-universal Higgs model with two extra parameters	33
4 The ATLAS Experiment at LHC	36
4.1 The Large Hadron Collide	37
4.2 The ATLAS experiment	40
4.2.1 The ATLAS coordinate system	41
4.2.2 The inner detector and tracking system	42
4.2.3 The calorimeters	45
4.2.4 The muon spectrometer	49
4.2.5 The trigger system and data acquisition	52

5 Data set and simulated events	54
5.1 Collision data	54
5.2 Monte Carlo simulated event samples	55
5.2.1 The SM background samples	56
5.2.2 The SUSY signal samples	56
6 Event reconstruction and selection	66
6.1 Object selections	66
6.1.1 Electrons	67
6.1.2 Muons	68
6.1.3 Taus	69
6.1.4 Photons	70
6.1.5 Jets	71
6.1.6 Missing transverse energy	72
6.1.7 Overlap removal	72
6.2 Signal region selection	73
6.2.1 Discriminating variables	73
6.2.2 Signal region	76
7 Background estimation	83
7.1 Control and validation regions	83
7.1.1 The concepts	83
7.1.2 Specific to this analysis	84
7.2 Irreducible background	86
7.3 Reducible background	86
7.4 Systematic uncertainties	86
8 Results	87
9 Conclusion	88
Appendix	90
A Cross-sections of NUHM2	90
B Electron isolation	99
B.1 Electron reconstruction	99
B.2 Electron identification	100
B.3 Electron isolation	100
C The distributions	101
D Search for strongly-produced SUSY in final states with two same-sign or three leptons and jets using $36.1 \text{ fb}^{-1} pp$ collision data at $\sqrt{s} = 13 \text{ TeV}$ with the ATLAS detector	114
D.1 Samples used for strong interaction	114
E Real lepton efficiency	117
E.1 The Z tag-and-probe method	117
E.2 Background subtraction	119
E.3 Cut efficiencies	121
E.4 Real lepton efficiencies	122

E.4.1	Tag-and-probe method and truth matching comparisons	123
E.4.2	Data-to-MC comparisons	123
E.4.3	Real lepton efficiency versus pileup	124
E.5	Sources of systematic uncertainties	124
E.5.1	Measurement systematics	124
E.5.2	Trigger bias	126
E.5.3	Extrapolation to signal regions	127
E.5.4	Final uncertainties	130
References		147

List of Tables

	Page
2.1 The Standard Model fermions with charges and masses [29].	7
2.2 The four fundamental forces with the relative strength, interaction range, describing theory, and the mediator with its mass. The gravitational force is not a part of the SM and the graviton is a theoretical particle.	8
3.1 Chiral supermultiplets and gauge supermultiplets in the MSSM. In the chiral supermultiplets, the spin 0 fields are complex scalars and the spin 1/2 fields are left-handed two-component Weyl spinors.	30
4.1 Resolution requirements for the different calorimeters of the ATLAS detector [66].	49
4.2 A summary of the muon spectrometer components.	51
5.1 The inclusive E_T^{miss} triggers used in this analysis. The E_T^{miss} threshold varies from 70 to 110 GeV depending on the run period.	55
5.2 The MC simulated samples of SM background process.	57
5.3 The masses of $\tilde{\chi}_1^0$, $\tilde{\chi}_2^0$, and $\tilde{\chi}_1^\pm$ and the ratios of the mass difference between $(m_{\tilde{\chi}_2^0} - m_{\tilde{\chi}_1^\pm})$ and $(m_{\tilde{\chi}_1^\pm} - m_{\tilde{\chi}_1^0})$. The $m_{\tilde{\chi}_1^\pm}$ doesn't set to the middle between $m_{\tilde{\chi}_1^0}$ and $m_{\tilde{\chi}_2^0}$	59
5.4 The possible $\tilde{\chi}_2^0$ decays in NUHM2 model with $m_{1/2} = 600$ GeV. The $\tilde{\chi}_2^0 \rightarrow \gamma \tilde{\chi}_1^0$ has the lowest branching ratio hence it is not considered in our study. The rest of the decays are categorized into 4 types as shown in the third column.	61
5.5 The 2 leptons filter efficiency for 4 kinds of $\tilde{\chi}_2^0$ decay, the number of events for each decay in $0 < m_{\ell\ell} < 50$ GeV, and the contributions to the whole $\tilde{\chi}_2^0$ decay. The transverse momentum of 2 leptons are required to be greater than 2 GeV and no E_T^{miss} requirement is applied in the filter.	62
5.6 The NUHM2 MC sample dataset ID (DSID), productions, cross-sections, and decay processes and its relevant branching ratios, the filter efficiencies, and the uncertainties.	64
5.7 The branching ratios calculated by ISAJET and SUSY-HIT. The difference are calculated with respect to the SUSY-HIT branching ratio results. Good agreement between the results from two branching ratio calculators can be seen. The largest difference between the results calculating by ISAJET and SUSY-HIT is less than 2%.	65
6.1 Summary of object definitions used in this analysis.	67
6.2 Summary of event selection criteria. Signal leptons and signal jets are used when applying all requirements. The SR binning is listed in Table 6.3.	80
6.3 The SR binnings for the electroweakino SRs. The SR is defined by a $m_{\ell\ell}$ range in GeV. The exclusive bins are used to set the exclusion limits on the model and the inclusive bins are used to set the model-independent limits.	80
6.4	81

6.5	82
7.1	The background processes for the 2ℓ analysis and the strategy for estimating the background contamination in the SR.	85
7.2	Definition of control regions and validation regions.	85
A.1	The cross-sections, branching fraction, and filter efficiency for the NUHM2 signal samples $m_{1/2} = 300$ GeV.	91
A.2	The cross-sections, branching fraction, and filter efficiency for the NUHM2 signal samples $m_{1/2} = 350$ GeV.	92
A.3	The cross-sections, branching fraction, and filter efficiency for the NUHM2 signal samples $m_{1/2} = 400$ GeV.	93
A.4	The cross-sections, branching fraction, and filter efficiency for the NUHM2 signal samples $m_{1/2} = 500$ GeV.	94
A.5	The cross-sections, branching fraction, and filter efficiency for the NUHM2 signal samples $m_{1/2} = 600$ GeV.	95
A.6	The cross-sections, branching fraction, and filter efficiency for the NUHM2 signal samples $m_{1/2} = 700$ GeV.	96
A.7	The cross-sections, branching fraction, and filter efficiency for the NUHM2 signal samples $m_{1/2} = 800$ GeV.	97
A.8	The list of various final states.	98
D.1	The simulated signal and background MC samples. The event generator, parton shower, cross-section normalization, PDF set, and the set of tuned parameters for each samples are shown. The $t\bar{t}WW, t\bar{t}WZ, tZ, tWZ, t\bar{t}, WH, ZH$ and triboson background samples are labeled in the "rare" because they contribute a very small amount to the signal region.	115
D.2	116
E.1	The list of single lepton and dilepton triggers used for the real lepton efficiency measurements. The dilepton triggers are used for studying the systematic uncertainties causing by the trigger.	118
E.2	The definition of the background templates for estimating the background contamination associated with the Z tag-and-probe method. The baseline template is used to estimate the background contamination. The variation 1 template has looser requirements and the variation 2 template has tighter requirements. They are used to assess the systematic caused by the background contamination.	119
E.3	The estimated background contamination in different p_T and $ \eta $ regions. The p_T and $ \eta $ binnings correspond to the one used for the final measurements.	121
E.4	The real electron efficiencies before and after performing the background subtraction in different p_T and $ \eta $ regions are shown in percentage.	121
E.5	The systematic uncertainties for real electron efficiencies. For the electron case, the background subtraction is applied on the first two p_T bins ($p_T < 20$ GeV). There are 3 sources of the systematic uncertainties: varying templates (t), varying fitting ranges (f), and varying $m_{\ell\ell}$ windows (m). When $p_T > 20$ GeV, only $m_{\ell\ell}$ window variation is considered.	125
E.6	The systematic uncertainties for real muon efficiencies. Only the $m_{\ell\ell}$ window variation is considered because no background subtraction is applied on the muon case.	126
E.7	The systematic uncertainties for real electron efficiencies due to the different trigger strategies. The uncertainties of each trigger strategy are calculated with respect to the one applied single lepton trigger with tag trigger matched. The total uncertainties are the quadratic sum of the uncertainties of each trigger strategy.	128

E.8 The systematic uncertainties for real muon efficiencies due to the different trigger strategies. The uncertainties of each trigger strategy are calculated with respect to the one applied single lepton trigger with tag trigger matched. The total uncertainties are the quadratic sum of the uncertainties of each trigger strategy.	129
E.9 The systematic uncertainties of the real lepton efficiency in busy environment using $\tilde{g} \rightarrow t\bar{t}\tilde{\chi}_1^0$.	144
E.10 The final uncertainties of the real electron efficiencies. TThe final uncertainties are the quadratic sum of the statistical uncertainties and the systematic uncertainties. The systematic uncertainties include the measurement uncertainty, the trigger uncertainty, the uncertainty comes from the differences between Z tag-and-probe method and truth matching. The uncertainties in the busy environment do not incorporate in the final uncertainties calculation because it is measured as a function of p_T and ΔR . The trigger uncertainties are measured using $p_T > 20$ GeV only.	145
E.11 The final uncertainties of the real muon efficiencies. TThe final uncertainties are the quadratic sum of the statistical uncertainties and the systematic uncertainties. The systematic uncertainties include the measurement uncertainty, the trigger uncertainty, the uncertainty comes from the differences between Z tag-and-probe method and truth matching. The uncertainties in the busy environment do not incorporate in the final uncertainties calculation because it is measured as a function of p_T and ΔR .	146

List of Figures

	Page
1.1 The scatter plot in the $m(\tilde{\chi}_1^0)$ vs $m(\tilde{\chi}_1^\pm)$ plane. The color encode the $\tilde{\chi}_1^0$ composition. The Higgsino-dominated LSPs are colored in yellow and along the $\tilde{\chi}_1^0$ - $\tilde{\chi}_1^\pm$ diagonal. The figure is taken from [13].	2
1.2 The Feynman diagrams representing the two leptons final statw of (a) $\tilde{\chi}_2^0 \tilde{\chi}_1^\pm$, (b) $\tilde{\chi}_1^\pm \tilde{\chi}_1^\mp$, (c) $\tilde{\chi}_2^0 \tilde{\chi}_1^0$ productions.	3
2.1 An illustration of the Higgs potential which has the form of a Mexican hat. The figure is taken from [40].	15
2.2 The observed local p -value as a function of m_H for the ATLAS [1] and CMS [2] experiment, respectively. The dashed line shows the expected local p_0 for a SM Higgs boson. The horizontal lines denotes the p -values corresponding to significances of 1 to 6σ	17
2.3 The measured running coupling constants in the SM (left) and prediction in the GUT (right). The three lines show the inverse value of the coupling constant for the three fundamental forces. This figure is taken from [46].	19
3.1 The Feymann diagram for the one loop correction to the Higgs squared mass due to (a) a fermion f and (b) a scalar S . The figure is taken from [9].	22
3.2 Typical sparticle mass spectra of RNS. The figure is taken from [60].	33
3.3 The Δ_{EW} contours in the $m_{1/2}$ vs μ plane of NUHM2 model for $m_0 = 5$ GeV, $\tan \beta = 15$, $A_0 = -1.6m_0$, and $m_A = 1$ TeV. The gray and blue shaded regions are excluded by the LEP1 and LEP2 searches for chargino pair production. The region on the left hand side of the blue solid line is excluded by LHC8 gluino pair searches. This figure is taken from [65].	35
4.1 The accelerator complex at CERN [73].	38
4.2 Overview of the ATLAS detector [66].	40
4.3 Cut-away view of the ATLAS inner detector [66].	43
4.4 Cut-away view of the calorimeter system [66].	46
4.5 Cut-away view of the accordion shaped EMB module with the dimensions for three layers [76].	48
4.6 Sketch of the muon system of the ATLAS detector [66].	51
4.7 The schematic view of the ATLAS trigger/DAQ system in Run-2. The figure is taken from [80].	52
5.1 The mass spectra of the charginos $\tilde{\chi}_{1,2}^\pm$ and neutralinos $\tilde{\chi}_{1,2,3,4}^0$ as a function of $m_{1/2}$ in the NUHM2 model. The $m_{\tilde{\chi}_1^0}$, $m_{\tilde{\chi}_2^0}$, and $m_{\tilde{\chi}_1^\pm}$ are roughly flat when $m_{1/2} > 500$ GeV. The $m_{\tilde{\chi}_3^0}$, $m_{\tilde{\chi}_4^0}$, and $m_{\tilde{\chi}_2^\pm}$ are heavier and increase with $m_{1/2}$. . .	58
5.2 The mass splitting spectra between charginos and neutralinos in the NUHM2 model. The mass differences $\Delta m(\tilde{\chi}_3^0, \tilde{\chi}_{1,2}^0)$ and $\Delta m(\tilde{\chi}_3^0, \tilde{\chi}_1^\pm)$ increase with $m_{1/2}$. The mass differences $\Delta m(\tilde{\chi}_1^\pm, \tilde{\chi}_1^0)$, $\Delta m(\tilde{\chi}_2^0, \tilde{\chi}_1^0)$, and $\Delta m(\tilde{\chi}_2^0, \tilde{\chi}_1^\pm)$ decreess with $m_{1/2}$. .	59

5.3	The NUHM2 cross-sections for (a) different combinations of compressed + compressed production and (b) all compressed + compressed, compressed + accessible, and accessible + accessible productions.	60
6.1	The illustration of the $Z \rightarrow \tau\tau + \text{jets}$ decay where τ decays leptonically $\tau \rightarrow \ell\nu_\ell\nu_\tau$	75
6.2	The distribution of $E_T^{\text{miss}}/H_T^{\text{lep}}$ as function of $m_{\ell\ell}$ for the electroweakino after applying all the SR common requirements and the $\Delta R_{\ell\ell} < 2$. The red line indicates the SR selection. Events in the region below this line are rejected. The signal events are labeled in colored circles for different mass splitting.	77
6.3	The ‘ $N - 1$ ’ distributions for NUHM2 model with $m_{1/2} = 500$ GeV in SR region $1 < \text{SR}_{\ell\ell} - m_{\ell\ell} < 60$ GeV. The NUHM2 distributions are multiplied by 10 but the number of events in the legend use its actual values.	78
6.4	The ‘ $N - 1$ ’ distributions for NUHM2 model with $m_{1/2} = 500$ GeV in SR region $1 < \text{SR}_{\ell\ell} - m_{\ell\ell} < 60$ GeV. The NUHM2 distributions are multiplied by 10 but the number of events in the legend use its actual values.	79
7.1	A illustration of multiple signal, control, and validation regions. The background contamination in the SRs can be estimated by extrapolating from the CRs and is verified in the VRs which lie in between the SRs and CRs. All regions can be single bin or multiple bins which are indicated by the dashed lines. The figure is taken from [104].	84
C.1	The ‘ $N - 1$ ’ distributions for NUHM2 model with $m_{1/2} = 350$ GeV in SR region $1 < \text{SR}_{\ell\ell} - m_{\ell\ell} < 60$ GeV. The NUHM2 distributions are multiplied by 10 but the number of events in the legend use its actual values.	102
C.2	The ‘ $N - 1$ ’ distributions for NUHM2 model with $m_{1/2} = 350$ GeV in SR region $1 < \text{SR}_{\ell\ell} - m_{\ell\ell} < 60$ GeV. The NUHM2 distributions are multiplied by 10 but the number of events in the legend use its actual values.	103
C.3	The ‘ $N - 1$ ’ distributions for NUHM2 model with $m_{1/2} = 400$ GeV in SR region $1 < \text{SR}_{\ell\ell} - m_{\ell\ell} < 60$ GeV. The NUHM2 distributions are multiplied by 10 but the number of events in the legend use its actual values.	104
C.4	The ‘ $N - 1$ ’ distributions for NUHM2 model with $m_{1/2} = 400$ GeV in SR region $1 < \text{SR}_{\ell\ell} - m_{\ell\ell} < 60$ GeV. The NUHM2 distributions are multiplied by 10 but the number of events in the legend use its actual values.	105
C.5	The ‘ $N - 1$ ’ distributions for NUHM2 model with $m_{1/2} = 500$ GeV in SR region $1 < \text{SR}_{\ell\ell} - m_{\ell\ell} < 60$ GeV. The NUHM2 distributions are multiplied by 10 but the number of events in the legend use its actual values.	106
C.6	The ‘ $N - 1$ ’ distributions for NUHM2 model with $m_{1/2} = 500$ GeV in SR region $1 < \text{SR}_{\ell\ell} - m_{\ell\ell} < 60$ GeV. The NUHM2 distributions are multiplied by 10 but the number of events in the legend use its actual values.	107
C.7	The ‘ $N - 1$ ’ distributions for NUHM2 model with $m_{1/2} = 600$ GeV in SR region $1 < \text{SR}_{\ell\ell} - m_{\ell\ell} < 60$ GeV. The NUHM2 distributions are multiplied by 10 but the number of events in the legend use its actual values.	108
C.8	The ‘ $N - 1$ ’ distributions for NUHM2 model with $m_{1/2} = 600$ GeV in SR region $1 < \text{SR}_{\ell\ell} - m_{\ell\ell} < 60$ GeV. The NUHM2 distributions are multiplied by 10 but the number of events in the legend use its actual values.	109
C.9	The ‘ $N - 1$ ’ distributions for NUHM2 model with $m_{1/2} = 700$ GeV in SR region $1 < \text{SR}_{\ell\ell} - m_{\ell\ell} < 60$ GeV. The NUHM2 distributions are multiplied by 10 but the number of events in the legend use its actual values.	110
C.10	The ‘ $N - 1$ ’ distributions for NUHM2 model with $m_{1/2} = 700$ GeV in SR region $1 < \text{SR}_{\ell\ell} - m_{\ell\ell} < 60$ GeV. The NUHM2 distributions are multiplied by 10 but the number of events in the legend use its actual values.	111

C.11	The ‘ $N - 1$ ’ distributions for NUHM2 model with $m_{1/2} = 800$ GeV in SR region $1 < \text{SR}\ell\ell-m_{\ell\ell} < 60$ GeV. The NUHM2 distributions are multiplied by 10 but the number of events in the legend use its actual values.	112
C.12	The ‘ $N - 1$ ’ distributions for NUHM2 model with $m_{1/2} = 800$ GeV in SR region $1 < \text{SR}\ell\ell-m_{\ell\ell} < 60$ GeV. The NUHM2 distributions are multiplied by 10 but the number of events in the legend use its actual values.	113
E.1	The invariant mass distributions of the tag-and-probe pair computed using $Z+jets$ MC and 2015 + 2016 data. The red color stands for the Z tag-and-probe events, the blue color represents the Z truth matched events, and the black dots are data. The MC distributions are scaled to the data using a Gaussian fit of the Z mass peak $85 < m_{\ell\ell} < 95$ GeV.	131
E.2	The m_{ee} distributions for the baseline, variation 1 and variation 2 background templates. The m_{ee} distributions are computed using the probe electrons with different p_T as indicated in the caption of plots. The variation 1 template has looser calorimeter and track isolation requirements and the baseline and the variation 2 templates have tighter selection criteria. So a peak can be seen in the Z mass region in variation 1 template but not in the baseline and variation 2 templates.	132
E.3	Illustration of the background subtraction procedure. The full black dots and blue squares are the m_{ee} distributions for data before and after performing the background subtraction, respectively. The m_{ee} distribution for $Z \rightarrow ee$ MC, which is labeled by the open black circles, is normalized to the data after the background subtraction using a Gaussian fit of $85 < m_{ee} < 95$ GeV. The lower panels show the data-to-MC ratio where the background subtraction has been applied on data. The background templates and their respective fitting results are indicated by the red triangles and green lines, respectively.	133
E.4	Cut efficiencies of the signal electron and muon definition as a function of p_T . The total real electron and muon efficiencies are presented by black points. The loose to medium likelihood cut efficiency is presented by red squares. The calorimeter and track isolation cut efficiencies are presented by green triangles and blue triangles, respectively. The longitudinal and transverse impact parameters cut efficiencies are presented by magenta diamonds and cyan crosses, respectively.	134
E.5	The real lepton efficiencies as a function of p_T and $ \eta $ measured using the Z tag-and-probe method. For the real electron efficiencies measurement, the $ \eta $ binning in the creak region is removed. A homogeneous $ \eta $ binnings are used for the muon case.	135
E.6	The real lepton efficiencies computed by Z tag-and-probe method (red dots) and truth matching (blue triangles). The electron cases are on the top row and muon cases are at the bottom row. The three columns from the left to the right are the real lepton efficiencies as a function p_T , $ \eta $, and $\Delta R(\ell, \text{jet})$, respectively. The lower pads show the ratio with respect to the Z tag-and-probe method.	136
E.7	The real lepton efficiencies measured on 2015 + 2016 data (black dots) and $Z \rightarrow \ell\ell$ MC samples (red squares) using the Z tag-and-probe method. The electron cases are on the top row and muon cases are at the bottom row. The three columns from the left to the right are the real lepton efficiencies as a function p_T , $ \eta $, and $\Delta R(\ell, \text{jet})$, respectively. The MC samples have been reweighted to the pile-up observed in data.	137

E.8 The real lepton efficiencies as a function of the average interactions per crossing $\langle \mu \rangle$. The data is presented in black dots, $Z \rightarrow \ell\ell$ tag-and-probe is presented in red squares, the truth matching is presented in blue triangles, the $t\bar{t}$ is presented in magenta diamonds, and $\tilde{g} \rightarrow t\bar{t}\tilde{\chi}_1^0$ is presented in yellow crosses. The $ \eta < 2$ requirement has been applied on the $t\bar{t}$ and $\tilde{g} \rightarrow t\bar{t}\tilde{\chi}_1^0$ MC samples for the electron case.	138
E.9 The real electron and muon efficiencies as a function of p_T . The data is presented in black dots, $Z \rightarrow \ell\ell$ tag-and-probe is presented in red squares, the truth matching is presented in blue triangles, the $t\bar{t}$ is presented in magenta diamonds, and $\tilde{g} \rightarrow t\bar{t}\tilde{\chi}_1^0$ is presented in yellow crosses. The differences in the $p_T < 40$ GeV region come from the different event topologies.	139
E.10 The real electron efficiencies as a function of p_T in 3 $ \eta $ regions. Four different trigger strategies are applied. The nominal values are obtained using the single lepton trigger with tag trigger matched. The differences between the nominal values and the values measured using other strategies are assigned as the systematic uncertainties.	140
E.11 The real muon efficiencies as a function of p_T in 4 $ \eta $ regions. Four different trigger strategies are applied. The nominal values are obtained using the single lepton trigger with tag trigger matched. The differences between the nominal values and the values measured using other strategies are assigned as the systematic uncertainties.	141
E.12 The kinematic distributions of the baseline leptons for $Z \rightarrow \ell\ell$, $\tilde{g} \rightarrow t\bar{t}\tilde{\chi}_1^0$, and $t\bar{t}$ processes. The top row is the p_T distributions and the bottom row is the $ \eta $ distributions. The electron case is on the left hand side and the muon case is on the right hand side. The $\tilde{g} \rightarrow t\bar{t}\tilde{\chi}_1^0$ process is more boosted and centralized than the $Z \rightarrow \ell\ell$ and $t\bar{t}$ processes.	142
E.13 The $\Delta R(\ell, \text{jet})$ and the N_{jets} distributions of the baseline leptons for $Z \rightarrow \ell\ell$, $\tilde{g} \rightarrow t\bar{t}\tilde{\chi}_1^0$, and $t\bar{t}$ processes. The top row is the $\Delta R(\ell, \text{jet})$ distributions and the bottom row is the N_{jets} distributions. The electron case is on the left hand side and the muon case is on the right hand side. The statistics of $Z \rightarrow \ell\ell$ processes are populated at higher $\Delta R(\ell, \text{jet}) < 1$ region and lower N_{jets} region. The statistics of $\tilde{g} \rightarrow t\bar{t}\tilde{\chi}_1^0$ are located in $\Delta R(\ell, \text{jet}) < 1$ region and higher N_{jets} region.	143

Chapter 1

Introduction

The Standard Model of particle physics (SM) describes various phenomena of particle physics. The discovery of the Higgs boson (H) by the ATLAS and CMS collaboration at CERN completes the missing part of the SM prediction [1, 2]. However, there are several open challenges that cannot be explained by the SM, such as hierarchy problem [3, 4, 5] and the dark matter candidate. In order to answer those questions, a new theory extending the SM is necessary. Supersymmetry (SUSY) [6, 7, 8, 9] is the most promising extensions of the SM. SUSY, which is a spacetime symmetry, introduces the superpartners of SM particles (sparticles) with spin differing by one-half unit with respect to the SM partners. The sparticles provide a potential solution to the hierarchy problem. If R -parity is conserved [10, 11, 12], the sparticles are produced in pairs and the lightest SUSY particle (LSP) is stable providing the candidate for dark matter.

The charginos $\tilde{\chi}_{1,2}^{\pm}$ and neutralinos $\tilde{\chi}_{1,2,3,4}^0$ are the mass eigenstates in the order of increasing masses and collectively referred to as electroweakinos. They are the mixture of the bino \widetilde{B} , winos \widetilde{W} , and higgsinos $\widetilde{H}_{u,d}$ which are the superpartners of the $U(1)$, $SU(2)$ gauge bosons, and the Higgs bosons, respectively. The charginos and neutralinos can decay into leptons and LSPs via W , Z , H or sleptons $\widetilde{\ell}$. In many SUSY models, the lightest neutralino $\tilde{\chi}_1^0$ is the LSP. The LSP couldn't be detected and results in significant

missing transverse energy E_T^{miss} .

The compressed scenarios refer to the small mass differences between heavier SUSY particles and the LSP. For example, the mass differences between the heavier electroweakino states $\tilde{\chi}_2^0$, $\tilde{\chi}_1^\pm$ and the wino- or higgsino-dominated LSP $\tilde{\chi}_1^0$ range from a few MeV to tens of GeV depending on the composition of the mixture. The \tilde{B} , \tilde{W} , and \tilde{H} composition of the $\tilde{\chi}_1^0$ have an influence on the degree of compression. Figure 1.1 shows the composition of the lightest neutralino in a MSSM scan of the electroweakino sector [13]. Based on naturalness arguments [14, 15], the Higgsino mass parameter μ , the bino and wino mass parameters M_1 and M_2 satisfy $|\mu| \ll |M_1|, |M_2|$ leading to the three electroweakinos $\tilde{\chi}_1^0$, $\tilde{\chi}_1^\pm$, and $\tilde{\chi}_2^0$ being dominated by the Higgsino.

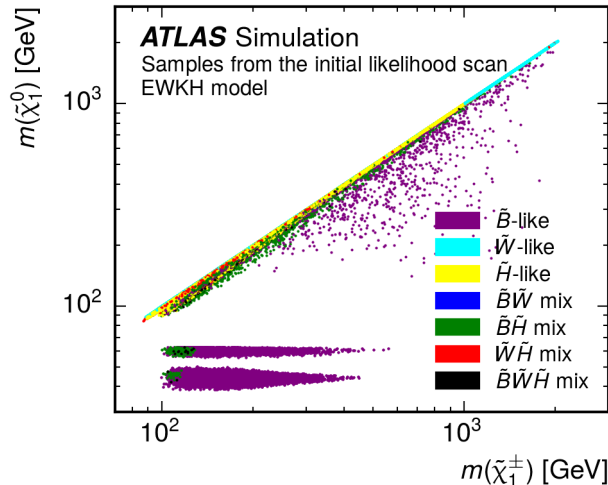


Figure 1.1: The scatter plot in the $m(\tilde{\chi}_1^0)$ vs $m(\tilde{\chi}_1^\pm)$ plane. The color encode the $\tilde{\chi}_1^0$ composition. The Higgsino-dominated LSPs are colored in yellow and along the $\tilde{\chi}_1^0$ - $\tilde{\chi}_1^\pm$ diagonal. The figure is taken from [13].

This dissertation focuses on searching for electroweak production SUSY particles in compressed scenarios with exactly two low-momentum same-flavor opposite-charged leptons in final states and missing transverse momentum $\mathbf{p}_T^{\text{miss}}$. This search uses proton-

proton collision data at $\sqrt{s} = 13$ TeV recorded by the ATLAS detector at the Large Hadron Collider (LHC) [16] in 2015 and 2016, corresponding to a total integrated luminosity of 36.1 fb^{-1} . Figure 1.2 shows the Feynman diagrams representing the electroweakino productions with two leptons final state in association with an initial state radiated jet. Same-flavor opposit-charged leptons come from the $\tilde{\chi}_2^0$ decays in the $\tilde{\chi}_2^0\tilde{\chi}_1^\pm$ and $\tilde{\chi}_2^0\tilde{\chi}_1^0$ productions, and from the $\tilde{\chi}_1^\pm$ decays in $\tilde{\chi}_1^\pm\tilde{\chi}_1^\mp$ production. The two leptons can be reconstructed in the detector and carry small transverse momentum p_T hence they are very soft. However, the two LSPs are invisible and back-to-back in the rest frame of their parent electroweakinos. Because they carry large momentum, the missing transverse energy E_T^{miss} is relatively large.

Similar searches have been performed using $\sqrt{s} = 8$ TeV and $\sqrt{s} = 13$ TeV by the ATLAS [17, 18, 19, 13] and CMS [20, 21, 22] experiments. Combining with the results from the LEP experiments, the mass limits for sleptons and charginos are $m(\tilde{e}_R) > 73$ GeV, $m(\tilde{\mu}_R) > 94.6$ GeV, and $m(\tilde{\chi}_1^\pm) > 103.5$ GeV or 92.4 GeV depending on the $\Delta m(\tilde{\chi}_1^0, \tilde{\chi}_1^\pm)$.

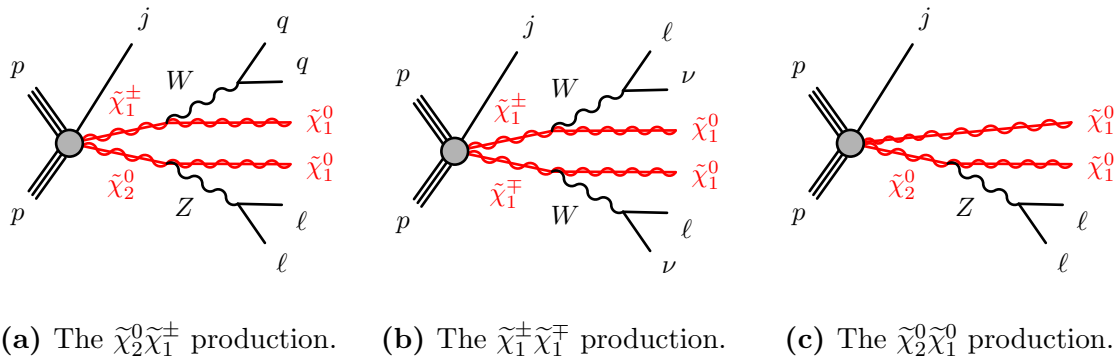


Figure 1.2: The Feynman diagrams representing the two leptons final statw of (a) $\tilde{\chi}_2^0\tilde{\chi}_1^\pm$, (b) $\tilde{\chi}_1^\pm\tilde{\chi}_1^\mp$, (c) $\tilde{\chi}_2^0\tilde{\chi}_1^0$ productions.

This dissertation has the following structure. After introducing the theoretical foundations in the Chapters 2 and 3, the experiment facilities are described in Chapter 4.

The data and Monte Carlo samples used in this analysis are detailed in Chapter 5. The event reconstruction and selection are outlined in Chapter 6. The background estimation and the systematic uncertainties are addressed in Chapter 7. Finally, the results and the conclusions are presented in Chapter 8 and Chapter 9. The search for strongly-produced SUSY particles in final states with two same-sign or three lepton and jets (SS/3L+jets) were also studied and the detail can be found in App. D.

Chapter 2

The Standard Model

This chapter outlines the theoretical and mathematical concepts of the high energy particle physics. The Standard Model of particle physics (SM) [23, 24, 25, 26, 27] is developed since the early 1970s and it has successfully explained almost all experimental results. The SM is a well-tested and the most successful physics theory to describe the nature of the elementary particles and their interactions. An overview of the SM is given in Sect. 2.1. After that, some of the open questions are mentioned in Sect. 2.2.

2.1 The Standard Model of Particle Physics

The Standard Model of particle physics is known as the most accurate theory for describing the elementary particles and the interactions between them. By combining the quantum mechanics and special relativity, the SM is a relativistic *Quantum Field Theory* (QFT) based on a $SU(3)_C \otimes SU(2)_L \otimes U(1)_Y$ symmetry gauge group, where C denotes colour, L represents left chirality, and Y stands for weak hypercharge, respectively. The $SU(3)_C$ group is the basis for *Quantum Chromodynamics* (QCD) which describes the strong interaction and the $SU(2)_L \otimes U(1)_Y$ group is the foundation of the electroweak interaction which unifies the electromagnetic and weak interactions. Therefore, the SM Lagrangian

is invariant under the local gauge transformation. According to *Noether's Theorem* [28], the invariance of an action of a physical system undergoes a symmetry transformation corresponding to a conservation law and vice versa. The gauge invariance of the SM Lagrangian corresponds to the conserved quantum numbers, or the charges, of each interaction. The conserved charges are the three colour charge (red, blue, green) for the strong interaction, the third component of the weak isospin I_3 for the weak interaction, and the electric charge Q for the electromagnetic interaction.

2.1.1 Particle Content

According to the SM, all matter around us is made of elementary particles called *quarks* and *leptons*. The quarks and leptons are called fermions which have half integral spin $s = \frac{1}{2}$, hence the fermions follow the Pauli exclusion principle which says no two fermions have the same quantum state at the same time. Each fermion has an anti-fermion with the equal mass but carries opposite electric charge, weak isospin and colour charge. There are six quarks and six leptons, they are grouped into three pairs, or "generations", ordered by their mass. The lightest and most stable particles constitute the first generation and they are constituents of ordinary matter. The heavier and less stable particles form the second and third generations and the heavier particles quickly decay to the next most stable particles. The three generations of quarks are up (u) and down (d), charm (c) and strange (s), and top (t) and bottom (b) quarks. The up-type quarks (u, c, t) carry $+\frac{2}{3}|e|$ charge and with isospin $+\frac{1}{2}$ while the down-type quarks (d, s, b) carry $-\frac{1}{3}|e|$ charge with isospin $-\frac{1}{2}$. The quarks carry an additional colour charge of either red, green, or blue, and hence they only interact via the strong force. Because the strong force holds quarks together, only non-integer charges of the quark combinations are experimentally allowed. The quark

combinations are called *hadrons* which can be categorised into *mesons* and *baryons*. The meson is composed by a quark and anti-quark pair ($q\bar{q}$) whereas the baryon is made up by three quarks (qqq or $\bar{q}\bar{q}\bar{q}$). Only colourless bound states of hadrons are allowed so the quark and anti-quark pair in a meson should contain colour and anti-colour and the three quarks in a baryon must carry different colours. The leptons are colourless and are therefore participating in the weak and electromagnetic force only. They do not participate in the strong interaction. The electron-type leptons (e, μ, τ) carry an elementary charge $|e|$ and their corresponding neutrinos (ν_e, ν_μ, ν_τ) are neutral. The neutrinos have very little mass and interact via weak force only. A summarised table of the properties of quarks and leptons is given in Table 2.1.

Generation	Fermion	particle	electric charge Q	weak isospin I_3	colour charge C	mass [GeV]
I	Quark	u up quark	$+\frac{2}{3} e $	$+\frac{1}{2}$	r,g,b	0.0023
		d down quark	$-\frac{1}{3} e $	$-\frac{1}{2}$	r,g,b	0.0048
	Lepton	e electron	$-1 e $	$-\frac{1}{2}$	-	0.00051
		ν_e electron neutrino	0	$+\frac{1}{2}$	-	$< 2 \times 10^{-9}$
II	Quark	c charm quark	$+\frac{2}{3} e $	$+\frac{1}{2}$	r,g,b	1.275
		s strange quark	$-\frac{1}{3} e $	$-\frac{1}{2}$	r,g,b	0.095
	Lepton	μ muon	$-1 e $	$-\frac{1}{2}$	-	0.106
		ν_μ muon neutrino	0	$+\frac{1}{2}$	-	$< 1.9 \times 10^{-7}$
III	Quark	t top quark	$+\frac{2}{3} e $	$+\frac{1}{2}$	r,g,b	173.2
		b bottom quark	$-\frac{1}{3} e $	$-\frac{1}{2}$	r,g,b	4.18
	Lepton	τ tau	$-1 e $	$-\frac{1}{2}$	-	1.777
		ν_τ tau neutrino	0	$+\frac{1}{2}$	-	$< 1.82 \times 10^{-5}$

Table 2.1: The Standard Model fermions with charges and masses [29].

There are four fundamental forces in the universe: the strong force, the weak force, the electromagnetic force, and the gravitational force. The first three forces are described in the SM, however, the gravitational force could not yet be included in the SM. Because

the effect of the gravitational force is very weak and can be negligible, the SM works well without considering the gravitational force. Each force has a force-carrier particle called gauge boson and there is a quantum number associate to it. The gauge bosons of the strong force are eight massless *gluons*, g , which associate to colour charge C . The gauge bosons of the weak force are W^\pm and Z^0 bosons which associate to weak isospin I_3 . The gauge boson of the electromagnetic force is massless *photon*, γ , which associates to electric charge Q . Although the gluon and photon are massless particles, the W^\pm and Z^0 bosons are massive. The mass of the W^\pm and Z^0 bosons are $m_W = 80.385 \pm 0.015$ GeV and $m_Z = 91.1876 \pm 0.0021$ GeV [29], respectively. Table 2.2 shows the four fundamental forces, the relative strength and range together with the theories and the mediators.

Force	Rel. Strength	Range [m]	Theory	Mediator	Mass [GeV]
Strong	10	10^{-15}	Chromodynamics	Gluon	0
Weak	10^{-13}	10^{-18}	Flavourdynamics	W^\pm and Z^0 bosons	80.4/91.2
Electromagnetic	10^{-2}	∞	Electrodynamics	Photon	0
Gravitational	10^{-42}	∞	General relativity	Graviton	-

Table 2.2: The four fundamental forces with the relative strength, interaction range, describing theory, and the mediator with its mass. The gravitational force is not a part of the SM and the graviton is a theoretical particle.

2.1.2 Local Gauge Theory

The Lagrangian density of the SM for the free fields¹ listed in the Eq. (2.1) is invariant under local gauge transformation²

$$\mathcal{L} = \bar{\psi}(i\gamma^\mu\partial_\mu - m)\psi + e\bar{\psi}\gamma^\mu\psi\mathbf{A}_\mu - \frac{1}{4}\mathbf{F}_{\mu\nu}\mathbf{F}^{\mu\nu} \quad (2.1)$$

where $\mathbf{F}_{\mu\nu} = \partial_\mu\mathbf{A}_\nu - \partial_\nu\mathbf{A}_\mu$. The local gauge transformation means the scalar field ψ and the vector field \mathbf{A}_μ transform as

$$\psi(x) \rightarrow \psi'(x) = e^{i\theta(x)}\psi(x) \quad (2.2)$$

$$\mathbf{A}_\mu(x) \rightarrow \mathbf{A}'_\mu(x) = \mathbf{A}_\mu(x) + \frac{1}{e}\partial_\mu\theta(x). \quad (2.3)$$

By introducing the gauge term, i.e. the vector field, the interacting force can be obtained by calculating the derivatives of the *Euler-Lagrange equations*. The gauge field can be associated to particular spin one gauge bosons which mediate the force. The number of the mediating gauge bosons is equal to the dimension of the symmetry group. From the group theory, the dimension of an unitary group $U(n)$ is n^2 and the dimension of a special unitary group $SU(n)$ is $n^2 - 1$. Because the SM is based on a $SU(3)_C \otimes SU(2)_L \otimes U(1)_Y$ symmetry gauge group, the number of mediators are 8 for $SU(3)_C$, 3 for $SU(2)_L$, and 1 for $U(1)_Y$ corresponding to 8 gluons for the strong interaction, 3 gauge bosons (W^\pm and Z^0) for weak interaction, and 1 photon for the electromagnetic interaction.

¹This is the Lagrangian density of QED. The three terms are fermion kinematic term, photon kinematic term, and interaction, respectively.

²In Dirac representation, the four contravariant gamma matrices are $\gamma^0 = \begin{pmatrix} 1 & 0 & 0 & 0 \\ 0 & 1 & 0 & 0 \\ 0 & 0 & -1 & 0 \\ 0 & 0 & 0 & -1 \end{pmatrix}$, $\gamma^1 = \begin{pmatrix} 0 & 0 & 0 & 1 \\ 0 & 0 & i & 0 \\ 0 & i & 0 & 0 \\ -i & 0 & 0 & 0 \end{pmatrix}$, $\gamma^2 = \begin{pmatrix} 0 & 0 & 0 & -i \\ 0 & 0 & i & 0 \\ 0 & i & 0 & 0 \\ -i & 0 & 0 & 0 \end{pmatrix}$, $\gamma^3 = \begin{pmatrix} 0 & 0 & 1 & 0 \\ 0 & 0 & 0 & -1 \\ -1 & 0 & 0 & 0 \\ 0 & 1 & 0 & 0 \end{pmatrix}$

2.1.3 Strong interaction

The *Quantum Chromodynamics* (QCD) is the theory to describe the strong interaction.

The gauge bosons are the eight massless gluons which carry three different colours (and anti-colours), red, green, and blue. Quarks interact with gluons hence they also carry colour charge C and can be represented in colour triplets

$$\psi = \begin{pmatrix} \psi_r \\ \psi_g \\ \psi_b \end{pmatrix}. \quad (2.4)$$

The QCD is based on the non-Abelian $SU(3)_C$ group which requires local gauge transformation

$$\psi \rightarrow \psi' = e^{ig_s\alpha_a(x)T^a}\psi \quad (2.5)$$

where the g_s is the strong coupling constant, $\alpha_a(x)$ are arbitrary functions of space-time, and T^a are the generators of the non-Abelian $SU(3)_C$ group and the summation over a with $a = 1, \dots, 8$ is implied. The Lagrangian density is invariant under the local gauge transformation by introducing the new form of the gauge fields and the covariant derivative

$$G_\mu^a \rightarrow G_\mu^a - \partial_\mu \alpha^a(x) - g_s f_{abc} \alpha^b(x) G_\mu^c \quad (2.6)$$

$$\partial_\mu \rightarrow D_\mu = \partial_\mu + ig_s T_a G_\mu^a \quad (2.7)$$

where f_{abc} is the structure constant. The Lagrangian density of QCD is given by

$$\mathcal{L}_{QCD} = \bar{\psi}(i\gamma^\mu \partial_\mu - m)\psi - g_s(\bar{\psi}\gamma^\mu T_a \psi) G_\mu^a - \frac{1}{4} G_{\mu\nu}^a G_a^{\mu\nu} \quad (2.8)$$

where the field strength tensor $G_{\mu\nu}^a = \partial_\mu G_\nu^a - \partial_\nu G_\mu^a - g_s f_{abc} G_\mu^b G_\nu^c$ causing self-interactions between the gluons. The strong force increases with distance between quarks, therefore, the quarks exist only as colourless compounds such as meson or baryon mentioned in

Sect. 2.1.1. The production of a single quark is accompanied by the creation of an anti-quark from vacuum to form a quark and anti-quark pair as a colourless compound. This is called *hadronisation*. The phenomena that confined quarks in the small interaction range is called *confinement*. But at small distance or high energy, the quarks can be considered as quasi-free particles. This is referred to as *asymptotic freedom*.

2.1.4 Electroweak interaction

Fermi formulated the first weak interaction theory in 1933 [30], however, the theory only holds for energies less than 100 GeV. Glashow, Salam, and Weinberg (GSW) proposed a new model [23, 25, 24] which unifies electromagnetic and weak forces to become *electroweak* (EW) force and this new *GSW model* can apply to the energy greater than 100 GeV. The electroweak theory is based on $SU(2)_L \otimes U(1)_Y$ gauge symmetry where the subscripts L denotes the left-handedness because only the left-handed fermions (and right-handed anti-fermions) and Y denotes the weak hypercharge, a new quantum number, which relates to the electric charge Q and the weak isospin I_3 by the *Gell-Mann-Nishijima relation* [31, 32]

$$Y = 2(Q - I_3). \quad (2.9)$$

The left-handed and right-handed fermion field ψ can be decomposed into two components

$$\psi = P_L\psi + P_R\psi \quad (2.10)$$

$$= \psi_L + \psi_R \quad (2.11)$$

where the projection operators P_L and P_R are defined as³

$$P_L = \frac{1}{2}(1 - \gamma^5) \quad (2.12)$$

$$P_R = \frac{1}{2}(1 + \gamma^5). \quad (2.13)$$

The projection operators satisfy $P_L P_R = 0$ and $P_L + P_R = 1$. Experimental observations show the right-handed neutrinos don't participate in all the interactions described in the SM so the ψ_R is a singlet and $I_3 = 0$ ⁴. The local gauge transformations of the $SU(2)_L \otimes U(1)_Y$ are

$$\psi_L \rightarrow \psi'_L = e^{i\alpha_a(x)T^a} e^{i\beta(x)Y} \psi_L \quad (2.14)$$

$$\psi_R \rightarrow \psi'_R = e^{i\beta(x)Y} \psi_R \quad (2.15)$$

where $T^a = \frac{\sigma^a}{2}$ are the generators of $SU(2)_L$ with Pauli matrix σ^a ⁵ and Y is the generator of $U(1)_Y$. The $\alpha_a(x)$ and $\beta(x)$ depend on the space-time. The covariant derivative with respect to the $SU(2)_L \otimes U(1)_Y$ is

$$D_\mu = \partial_\mu + ig_W T_a \mathbf{W}_\mu^a + ig_Y Y \mathbf{B}_\mu \quad (2.16)$$

where g_W and g_Y are coupling constants and \mathbf{W}_μ^a ($a = 1, 2, 3$) and \mathbf{B}_μ are the gauge fields.

The gauge fields \mathbf{W}_μ^a and \mathbf{B}_μ transform under the $SU(2)_L \otimes U(1)_Y$ symmetry as

$$\mathbf{W}_\mu^a \rightarrow \mathbf{W}_\mu^a - \frac{1}{g_W} \partial_\mu \alpha^a(x) - \epsilon^{abc} \alpha^b(x) \mathbf{W}_\mu^c \quad (2.17)$$

$$\mathbf{B}_\mu \rightarrow \mathbf{B}_\mu - \frac{1}{g_Y} \partial_\mu \beta(x) \quad (2.18)$$

where ϵ^{abc} is the Levi-Civita tensor. The Lagrangian density of the electroweak is given by

$$\mathcal{L}_{EW} = \bar{\psi}_L (i\gamma^\mu D_\mu - m) \psi_L + \bar{\psi}_R (i\gamma^\mu D_\mu - m) \psi_R - \frac{1}{4} \mathbf{W}_{\mu\nu}^a \mathbf{W}_a^{\mu\nu} - \frac{1}{4} \mathbf{B}_{\mu\nu} \mathbf{B}^{\mu\nu} \quad (2.19)$$

³ γ^5 is the product of the four gamma matrices. $\gamma^5 = i\gamma^0\gamma^1\gamma^2\gamma^3 = \begin{pmatrix} 0 & 0 & 1 & 0 \\ 0 & 0 & 0 & 1 \\ 1 & 0 & 0 & 0 \\ 0 & 1 & 0 & 0 \end{pmatrix}$

⁴The left-handed fermion state ψ_L is a doublet.

⁵The Pauli matrices are $\sigma_1 = \begin{pmatrix} 0 & 1 \\ 1 & 0 \end{pmatrix}$, $\sigma_2 = \begin{pmatrix} 0 & -i \\ i & 0 \end{pmatrix}$, and $\sigma_3 = \begin{pmatrix} 1 & 0 \\ 0 & -1 \end{pmatrix}$

where $\mathbf{W}_{\mu\nu}^a$ and $\mathbf{B}_{\mu\nu}$ are the field strength tensors

$$\mathbf{W}_{\mu\nu}^a = \partial_\mu \mathbf{W}_\nu^a - \partial_\nu \mathbf{W}_\mu^a - g_W \epsilon^{abc} \mathbf{W}_\mu^b \mathbf{W}_\nu^c \quad (2.20)$$

$$\mathbf{B}_{\mu\nu} = \partial_\mu \mathbf{B}_\nu - \partial_\nu \mathbf{B}_\mu \quad (2.21)$$

and $\bar{\psi} \equiv \psi^\dagger \gamma^0$ is the adjoint spinor of ψ ⁶. Therefore, the mass eigenstates are the mixture of the gauge fields

$$\mathbf{W}_\mu^\pm = \frac{1}{\sqrt{2}} (\mathbf{W}_\mu^1 \mp i \mathbf{W}_\mu^2) \quad (2.22)$$

$$\begin{pmatrix} \mathbf{A}_\mu \\ \mathbf{Z}_\mu \end{pmatrix} = \begin{pmatrix} \cos \theta_W & \sin \theta_W \\ -\sin \theta_W & \cos \theta_W \end{pmatrix} \begin{pmatrix} \mathbf{B}_\mu \\ \mathbf{W}_\mu^3 \end{pmatrix}. \quad (2.23)$$

Thus, the mass eigenstates \mathbf{A}_μ , \mathbf{W}_μ^\pm , and \mathbf{Z}_μ are identified as the photon, γ , W^\pm and Z^0 bosons experimentally. The *Weinberg weak mixing angle* θ_W is defined as

$$\tan \theta_W = \frac{g_Y}{g_W}. \quad (2.24)$$

The coupling constants g_W and g_Y are related to the electric charge by

$$e = g_W \sin \theta_W = g_Y \cos \theta_Y. \quad (2.25)$$

And the weak eigenstates of quark, q' , are the linear combinations of the mass eigenstates of quark, q , by the *Cabbibo-Kobayashi-Maskawa* (CKM) matrix [33]

$$\begin{pmatrix} d' \\ s' \\ b' \end{pmatrix} = \begin{pmatrix} V_{ud} & V_{us} & V_{ub} \\ V_{cd} & V_{cs} & V_{cb} \\ V_{td} & V_{ts} & V_{tb} \end{pmatrix} \begin{pmatrix} d \\ s \\ b \end{pmatrix}. \quad (2.26)$$

The CKM matrix allows the quarks changing their flavour and generation as observed in the experiment. Similarly, the *Pontecorvo-Maki-Nakagawa-Sakata* (PMNS) matrix [34] is responsible for the flavour changing of the neutrinos.

⁶ ψ^\dagger is the hermitian conjugate of ψ

Spontaneous symmetry breaking and Higgs mechanism

The gauge bosons of the weak interaction, W^\pm and Z^0 , are massive particles⁷. However, the existence of the mass terms violate the gauge invariance of the \mathcal{L}_{EW} . In order to explain the mass of gauge bosons, the Englert-Brout-Higgs mechanism [35, 36, 37, 38, 39] was proposed in 1964. A new scalar complex $SU(2)_L$ doublet field Φ is introduced in the Higgs mechanism

$$\Phi = \begin{pmatrix} \Phi^+ \\ \Phi^0 \end{pmatrix} = \begin{pmatrix} \Phi_1 & i\Phi_2 \\ \Phi_3 & i\Phi_4 \end{pmatrix} \quad (2.27)$$

with hypercharge $Y = 1$ and four degrees of freedom, Φ_i , which are scalar fields and called the *Goldstone modes*. The Lagrangian density for this new field, Higgs field, is

$$\mathcal{L}_\Phi = (D^\mu \Phi)^\dagger (D_\mu \Phi) - V(\Phi) \quad (2.28)$$

where the Higgs potential is defined as

$$V(\Phi) = \mu^2 |\Phi|^2 + \lambda |\Phi|^4 \quad (2.29)$$

where μ and λ are free parameters. The Higgs potential is shown in Fig. 2.1. The Higgs potential is the rotation $U(1)$ symmetry. Choosing any of the points at the bottom of the Higgs potential breaks the symmetry spontaneously. The *spontaneously symmetry breaking* (SSB) means the Lagrangian keeps invariant under certain symmetry but no longer invariant at the ground state.

Because the Higgs potential is invariant under $SU(2)_L \otimes U(1)_Y$, the parameters μ and λ must satisfy $\mu^2 < 0$ and $\lambda > 0$ resulting in a set of degenerate ground states where $\langle 0 | \Phi | 0 \rangle \neq 0$. Among the degenerate ground states, the ground state is often chosen to

⁷ $m_W = 80.385 \pm 0.015$ GeV and $m_Z = 91.1876 \pm 0.0021$ GeV

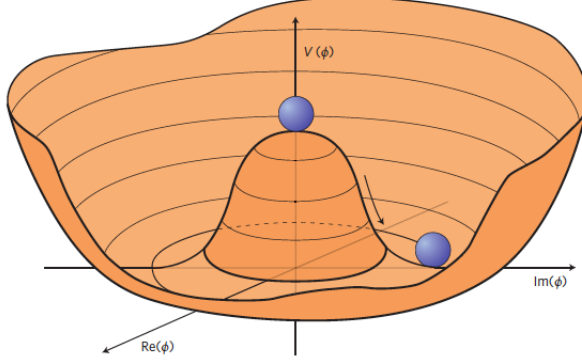


Figure 2.1: An illustration of the Higgs potential which has the form of a Mexican hat. The figure is taken from [40].

have the form

$$\Phi = \frac{1}{\sqrt{2}} \begin{pmatrix} 0 \\ v \end{pmatrix} \quad (2.30)$$

where $v = \sqrt{-\mu^2/\lambda}$ is the *the vacuum expectation value* (VEV). This particular choice of the ground state breaks the $SU(2)_L \otimes U(1)_Y$ symmetries spontaneously and ensures the unbroken electromagnetic interaction under $U(1)_{EM}$ symmetry and photon being massless. By introducing a massive particle, Higgs boson H , the Higgs field can be re-written as

$$\Phi = \frac{1}{\sqrt{2}} \begin{pmatrix} 0 \\ v + H \end{pmatrix} \quad (2.31)$$

and the kinematic term of the Lagrangian density becomes

$$\mathcal{L}_\Phi^{\text{kinematic}} = (D^\mu \Phi)^\dagger (D_\mu \Phi) \quad (2.32)$$

$$= \frac{1}{2} \partial_\mu H \partial^\mu H + (v + H)^2 \left\{ \frac{g_W^2}{4} \mathbf{W}_\mu^\dagger \mathbf{W}^\mu + \frac{g_W^2}{8 \cos^2 \theta_W} \mathbf{Z}_\mu^\dagger \mathbf{Z}^\mu \right\} \quad (2.33)$$

and the Higgs potential is now

$$V(\Phi) = -\frac{v^2 \lambda}{2} (v + H)^2 + \frac{\lambda}{4} (v + H)^4. \quad (2.34)$$

Thus the masses of the W^\pm and Z^0 are obtained by the interaction between the gauge

bosons and Higgs boson. The masses are defined as

$$m_H = v\sqrt{2\lambda}, \quad m_W = \frac{v}{2}g_W, \quad m_Z = \frac{v}{2}\sqrt{g_W^2 + g_Y^2}, \quad m_\gamma = 0. \quad (2.35)$$

However, the masses of fermions are obtained by the *Yukawa interaction*

$$\mathcal{L}_{\text{Yukawa}} = y_f \bar{L}_L \Phi f_R + y_f \bar{Q}_L \Phi f_R + \text{h.c.} \quad (2.36)$$

where the y_f is *Yukawa coupling*, f stands for $\{\ell^i, u^i, d^i\}$ and h.c. represents the hermitian conjugate, respectively. The \bar{L}_L and \bar{Q}_L are the left-handed lepton and quark doublet and f_R is the lepton or quark singlet. The mass of fermion is defined as

$$m_f = \frac{v}{\sqrt{2}}y_f \quad (2.37)$$

where y_f is a free parameter which causes the fermion mass not predictable. Finally, the non-zero VEV, v , can be related to *Fermi constant*, G_F , by

$$v = \frac{1}{\sqrt{\sqrt{2}G_F}} \approx 246 \text{ GeV}. \quad (2.38)$$

2.1.5 The discovery of Higgs boson

A lot of the SM predictions are successfully confirmed by the experimental observations besides the existence of the theoretical Higgs boson. The search of the Higgs boson has become a major goal of the experimental particle physicists. A Higgs-like resonance was discovered and announced on July 4th 2012 by the ATLAS⁸ and CMS⁹ collaborations [1, 2]. By combining the data with integrated luminosities of 4.8 fb^{-1} collected at $\sqrt{s} = 7 \text{ TeV}$ in 2011 and 5.8 fb^{-1} at $\sqrt{s} = 8 \text{ TeV}$ in 2012, the ATLAS experiment measured the mass of the Higgs boson to be $126.0 \pm 0.4 \text{ (stat.)} \pm 0.4 \text{ (syst.)} \text{ GeV}$ with significance of 5.9σ corresponding to a background fluctuation probability of 1.7×10^{-9} [1]. In the meantime,

⁸A Toroidal LHC Apparatus

⁹Compact Muon Solenoid

the CMS experiment announced the mass of the Higgs boson to be 125.3 ± 0.4 (stat) ± 0.5 (syst.) GeV with significance 5.0σ using integrated luminosities of up to 5.1 fb^{-1} at 7 TeV and 5.3 fb^{-1} at 8 TeV [2]. The $H \rightarrow ZZ^{(*)} \rightarrow 4\ell$, $H \rightarrow \gamma\gamma$, and $H \rightarrow WW^{(*)} \rightarrow e\nu\mu\nu$ channels were studied by the ATLAS collaboration and the $H \rightarrow \gamma\gamma$, ZZ , W^+W^- , $\tau^+\tau^-$, and $b\bar{b}$ channels were studied by the CMS collaboration. In the Fig. 2.2 shows the local p -value as a function of the Higgs mass for ATLAS and CMS results, respectively.

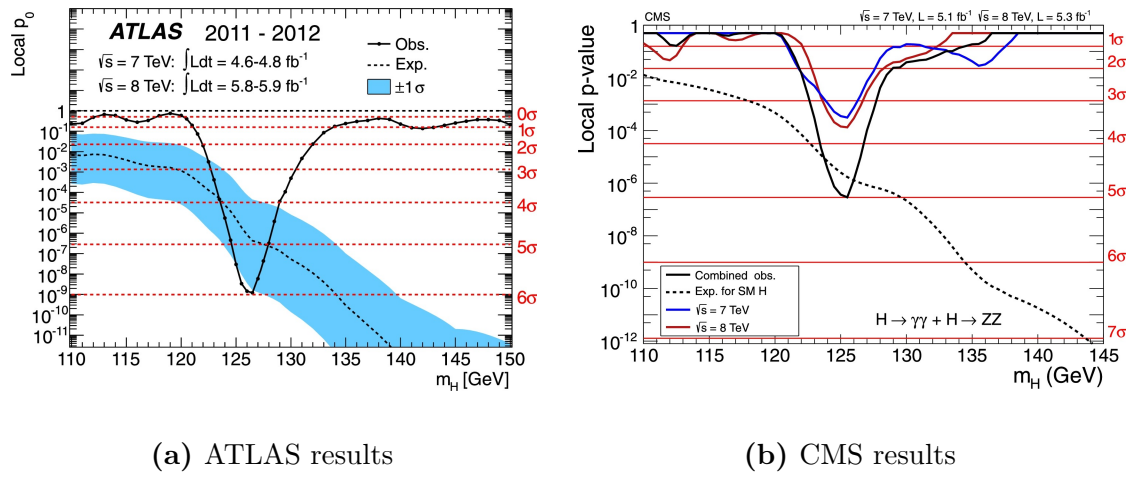


Figure 2.2: The observed local p -value as a function of m_H for the ATLAS [1] and CMS [2] experiment, respectively. The dashed line shows the expected local p_0 for a SM Higgs boson. The horizontal lines denotes the p -values corresponding to significances of 1 to 6σ .

2.2 Beyond the Standard Model

Although the SM is an incredible successful theory for explaining the phenomenon in the particle physics, it leaves some questions which can no be answered. Some of the unanswered questions are introduced in the rest part of this section.

2.2.1 Hierarchy problem

The weakest force in the SM is the weak force but the strength of the weak force is 10^{24} times as strong as gravitational force which doesn't incorporate into the SM. The large discrepancy between the weak force and the gravitational force is called the hierarchy problem [9, 41, 42]. The classical potential of the SM Higgs field Φ is

$$V(\Phi) = \mu^2 |\Phi|^2 + \lambda |\Phi|^4. \quad (2.39)$$

Since the SM requires the VEV for Φ , $\langle\Phi\rangle$, at the minimum of the potential non-vanishing, this is only satisfied if $\mu^2 < 0$ and $\lambda > 0$. However, the parameter μ^2 receives enormous radiative corrections causing it ultraviolet divergent as shown in Eq. (2.40).

$$\mu^2 = \mu_{bare}^2 - \frac{|\lambda_f|^2}{8\pi} \Lambda_{UV}^2 + \mathcal{O}(\Lambda_{UV}^2) \quad (2.40)$$

where μ_{bare} is the Higgs mass, $-\frac{|\lambda_f|^2}{8\pi} \Lambda_{UV}^2$ is the one-loop correction, and Λ_{UV} is an ultraviolet momentum cutoff which is valid up to the Plank scale 10^{19} GeV. The electroweak gauge bosons W^\pm and Z^0 obtain their finite masses from $\langle\Phi\rangle$ so the μ^2 cannot be divergent. There must be some unknown mechanism to protect from divergence.

2.2.2 Dark matter and dark energy

The matters we know today compose of only 5% [43, 44] of the content of the universe and the remaining part is something we don't know. This unknown matter is called *Dark Matter* (DM) [45] which makes up about 27% of the universe and the rest 68% are called *Dark Energy* (DE) [43, 44]. Because DM interacts weakly and doesn't interact with the electromagnetic force, it doesn't absorb, emit, or reflect light causing it hard to detect directly. The name DM comes from it is invisible. Dark energy distributes evenly in both space and time throughout the universe so it doesn't dilute when the universe

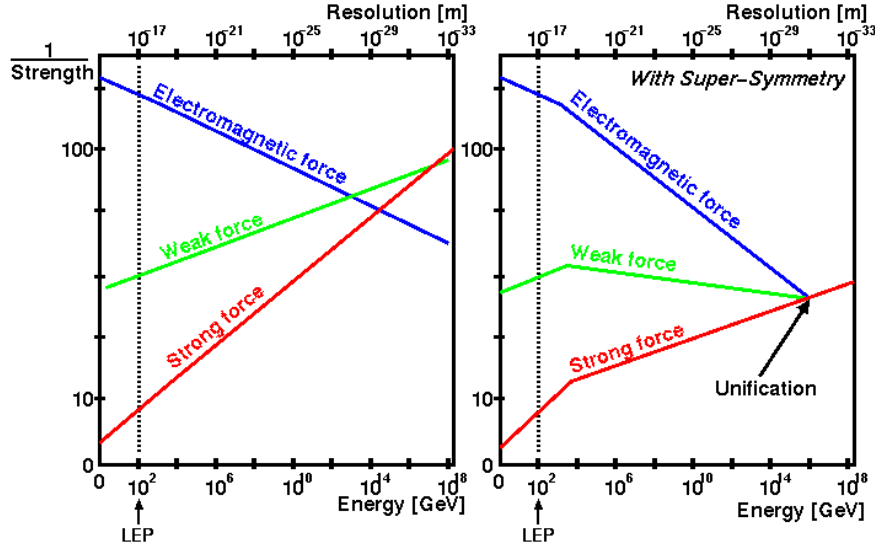


Figure 2.3: The measured running coupling constants in the SM (left) and prediction in the GUT (right). The three lines show the inverse value of the coupling constant for the three fundamental forces. This figure is taken from [46].

expands. The observed scientific data hints the presence of DE is necessary to explain the accelerated expansion of the universe.

2.2.3 Grand Unification

Maxwell unified the electricity and magnetism into electromagnetism in the 1860s. About a century later, physicists successfully developed theory of electroweak which links the electromagnetism and the weak force. Because of the triumph of electroweak theory, theorists raise the question of the possibility to unify all forces. The *Grand Unified Theory* (GUT) [47], which tries to link three of the four known forces together, is developed in the mid-1970s by theorists. The GUT proposes that the electromagnetic force, weak force, and strong force unify to one force at the GUT scale, $\Lambda_{GUT} \approx 10^{16}$ GeV. So the three running coupling constants [48] are expected to be converged at the GUT scale. However, the current experiment results show the coupling constants still different as shown in Fig. 2.3.

2.2.4 More questions

There are some more interesting questions which we don't know the answers. For example, we don't know the reason why there are 61 elementary particles and more than 20 arbitrary parameters in the SM. Also, the SM doesn't explain why there are only three generations. The amount of matter and anti-matter are equal at the beginning of the universe based on the prediction of the SM but the matter dominates in the currently universe which the SM couldn't answer the reason why.

In order to answer these questions, there are many theories being developed on the top of SM but none of them has been observed. One of the most probable candidate for answering these question is supersymmetry which will be introduced in the next chapter.

Chapter 3

Supersymmetry

The SM [23, 24, 25, 26, 27] gets a stupendous success in expecting and explaining the physics phenomena of the elementary particles. However, the SM leaves several open questions unanswered as mentioned in Sect. 2.2. Many different models of new physics were proposed to explain those unanswered questions. Among these new models, the *supersymmetry* (SUSY) [7, 49, 50, 9, 51, 52, 53, 54, 55] wins most physicists' favour. The SUSY proposed by Wess and Zumino [7] at early 1970s is a symmetry relating bosonic and fermionic degrees of freedom. It extends the SM by requiring every SM boson/fermion has a fermionic/bosonic supersymmetric partner and vice versa. The reason why physicists favour SUSY is described in Sect. 3.1 and the introduction of the SUSY as well as the formulaism are given in Sect. 3.2. The *Radiative Natural SUSY* (RNS) and the *Non-Universal Higgs Mass model* with two extra parameters (NUHM2) are given in Sect. 3.3 and 3.4, respectively.

3.1 Why supersymmetry

The SM leaves several unanswered questions, for example, the hierarchy problem (Sect. 2.2.1), what is the candidates of dark matter (Sect. 2.2.2), and why don't the running coupling

constants unify at GUT level (Sect. 2.2.3). The SUSY provides good explanations for these questions.

Hierarchy problem

The SM expects the Higgs squared mass divergent at the Plank scale $\sim 10^{19}$ GeV. However, the W^\pm and Z^0 gauge bosons obtained their finite mass through the Higgs mechanism indicates the Higgs squared mass must be finite. The Fig. 3.1 shows the Feynmann diagram for the one loop correction to the Higgs squared mass due to a fermion f and a scalar S .



Figure 3.1: The Feynmann diagram for the one loop correction to the Higgs squared mass due to (a) a fermion f and (b) a scalar S . The figure is taken from [9].

The corrections are

$$\Delta m_H^2 = -\frac{|\lambda_f^2|}{8\pi^2} \Lambda_{UV}^2 + \dots, \quad \text{fermion} \quad (3.1)$$

$$\Delta m_H^2 = \frac{\lambda_S}{16\pi^2} \Lambda_{UV}^2 + \dots, \quad \text{boson} \quad (3.2)$$

where the Λ_{UV} is an ultraviolet momentum cutoff which is valid up to the Planck scale 10^{19} GeV. The corrections diverge when Λ_{UV} becomes very large. Because the contributions from the fermion and scalar loops have opposite sign, the divergence contributions can be canceled out if there is a scalar loop for each fermionic loop. The SUSY predicts the existence of the bosonic/fermionic sparticles, therefore, if $\lambda_S = 2|\lambda_f^2|$ then the SUSY maintains the finiteness of the Higgs squared mass in a natural way.

Dark matter

The dark matter (DM) makes up about 27% of the universe and it might originate from neutral relic from the early universe. The cosmology observations of the DM indicate that the dark matter should be electrically neutral, cold, massive, and it participates only the weak and gravitational interactions. Therefore, the DM candidate should be a new particle which is *weakly interacting massive particle* (WIMP). The SUSY requires all the sparticles must be produced in pairs and they decay into stable *lightest SUSY particles* (LSP) with odd number. If there are a lot of sparticles produced in the early Universe, they will have to decayed to LSPs and remain until the present day because the LSP is stable. The LSP is a weakly interacting massive particle. It doesn't interact electromagnetically so they cannot be scattered by photon and thus dark. There are 3 kinds of LSP could be the possible DM candidate, the lightest *neutralino*, the lightest *sneutrino* and the *gravitino*.

Grand Unification

The Grand Unified Theory (GUT) tries to unify the strong and electroweak interactions. There will be only one interaction and one coupling constant at the GUT scale ($\approx 10^{16}$ GeV). However, the current coupling constants for electromagnetic, weak, and strong interactions don't unified at the GUT scale as shown in the left hand side of Fig. 2.3. This problem can be solved by introducing the SUSY which modifies the renormalization group equations and make the running gauge couplings converged at the GUT scale. The right hand side of Fig. 2.3 shows the running gauge couplings in SUSY.

3.2 Introduction of the supersymmetry

An brief overview of the SUSY are introduced in this section. Firstly, the mathematical foundation of the SUSY, superalgebra, is described in Sect. 3.2.1 followed by the superspace and superfields in Sect. 3.2.2.

3.2.1 Superalgebra

Poincaré algebra

The SUSY is based on the superalgebra which is an extension of space-time Poincaré algebra. The Poincaré group is a product of the Lorentz group and the group of translations in space-time. A Lorentz group must satisfies the commutation relations

$$[J_i^+, J_j^+] = i\epsilon_{ijk}J_k^+, \quad [J_i^-, J_j^-] = i\epsilon_{ijk}J_k^-, \quad [J_i^+, J_j^-] = 0 \quad (3.3)$$

where $i, j, k = 1, 2, 3$. If the six Lorentz group generators are combined into an antisymmetric second rank tensor generator $M_{\mu\nu}$ where $M_{ij} = \epsilon_{ijk}J_k$ and $M_{0i} = -M_{i0} = -K_i$ ¹ and the generator of the translation groups is P_μ , the energy-momentum operator, then the commutation relations of the Poincaré group are

$$[P_\mu, P_\nu] = 0, \quad (3.4)$$

$$[M_{\mu\nu}, P_\lambda] = i(g_{\nu\lambda}P_\mu - g_{\mu\lambda}P_\nu), \quad (3.5)$$

$$[M_{\mu\nu}, M_{\rho\sigma}] = -i(g_{\mu\rho}M_{\nu\sigma} - g_{\mu\sigma}M_{\nu\rho} - g_{\nu\rho}M_{\mu\sigma} + g_{\nu\sigma}M_{\mu\rho}). \quad (3.6)$$

¹The J_i and K_i with $i = 1, 2, 3$ are rotation and boost generators in 3-dimension respectively. And the ladder operators are defined as $J_i^\pm = \frac{1}{2}(J_i \pm iK_i)$.

where the metric is

$$g_{\mu\nu} = \begin{pmatrix} 1 & 0 & 0 & 0 \\ 0 & -1 & 0 & 0 \\ 0 & 0 & -1 & 0 \\ 0 & 0 & 0 & -1 \end{pmatrix} \quad (3.7)$$

Spinor

A general spin $\frac{1}{2}$ particle state, χ , can be expressed as a *spinor* in the SUSY using two-component spin up χ_+ and spin down χ_- column matrices

$$\chi = c_+ \chi_+ + c_- \chi_- = c_+ \begin{pmatrix} 1 \\ 0 \end{pmatrix} + c_- \begin{pmatrix} 0 \\ 1 \end{pmatrix} = \begin{pmatrix} c_+ \\ c_- \end{pmatrix} \quad (3.8)$$

The solution of the Dirac equation², ψ_D ³, can be expressed using the left-handed and right-handed *Weyl spinors* ψ_L and ψ_R

$$\psi_D = \begin{pmatrix} \psi_1 \\ \psi_2 \\ \psi_3 \\ \psi_4 \end{pmatrix} = \begin{pmatrix} \psi_1 \\ \psi_2 \\ \psi_3 \\ \psi_4 \end{pmatrix} = \begin{pmatrix} \psi_L \\ \psi_R \end{pmatrix} \quad (3.9)$$

It is convenient to use the Weyl spinors to represent the building blocks for any fermion field. The Majorana spinor $\tilde{\psi}_M$ is a real solution of Dirac equation. It is its own charge conjugate and satisfies the Majorana condition

$$\tilde{\psi}_M = \tilde{\psi}_M^* \quad (3.10)$$

The Majorana spinor can be expressed in terms of the Weyl spinors

$$\psi_M = \begin{pmatrix} \xi_\alpha \\ \bar{\xi}^{\dot{\alpha}} \end{pmatrix} \quad (3.11)$$

²The Dirac equation is $(i\gamma^\mu \partial_\mu - m)\psi = 0$.

³The Dirac spinor ψ_D is a four-component field which can be expressed using a four-component matrix.

where the left-handed Weyl spinor ξ_α and the right-handed Weyl spinor $\bar{\xi}^{\dot{\alpha}}$ are the Hermitian conjugate of each other.

Helicity

A particle with momentum \vec{p} and angular momentum \vec{J} , then the *helicity* is defined as

$$h = \vec{J} \cdot \hat{p} = (\vec{L} + \vec{S}) \cdot \hat{p} = \vec{S} \cdot \hat{p}, \quad \hat{p} = \frac{\vec{p}}{|\vec{p}|} \quad (3.12)$$

The eigenvalues of h are +1 and -1 corresponding to right-handed and left-handed eigenstates. Although the helicity is rotation invariant but not boost invariant, the helicity of a massless particle moving at the speed of light is Lorentz invariant.

3.2.2 Superspace and superfields

The superspace is composed of the ordinary space-time coordinate and four anticommuting fermionic coordinates θ_α and $\bar{\theta}_{\dot{\alpha}}$ where the spinor indices α and $\dot{\alpha}$ can be 1 or 2. A superfield $S(x^\mu, \theta_\alpha, \bar{\theta}_{\dot{\alpha}})$ is a function in superspace. The general form of a superfield can be expressed in terms of θ and $\bar{\theta}$

$$S(x, \theta, \bar{\theta}) = a + \theta\xi + \bar{\theta}\bar{\chi} + \theta\theta b + \bar{\theta}\bar{\theta}c + \bar{\theta}\bar{\sigma}^\mu\theta v_\nu + \theta\theta\bar{\theta}\bar{\zeta} + \bar{\theta}\bar{\theta}\theta\eta + \theta\theta\bar{\theta}\bar{\theta}d \quad (3.13)$$

where all spinor indices are suppressed. The a, b, c, d , and v_μ are bosonic fields and $\xi, \bar{\chi}, \bar{\zeta}, \eta$ are fermionic fields which are complex functions of x^μ . The SUSY generators Q_α and $\bar{Q}_{\dot{\alpha}}$ can be expressed as

$$Q_\alpha = -i \frac{\partial}{\partial \theta^\alpha} - \sigma_{\alpha\dot{\beta}}^\mu \bar{\theta}^{\dot{\beta}} \partial_\mu, \quad \bar{Q}_{\dot{\alpha}} = i \frac{\partial}{\partial \bar{\theta}^{\dot{\alpha}}} + \theta^\beta \sigma_{\beta\dot{\alpha}}^\mu \partial_\mu \quad (3.14)$$

and the commutation relations are

$$\{Q_\alpha, \bar{Q}_{\dot{\beta}}\} = -2i\sigma_{\alpha\dot{\beta}}^\mu \partial_\mu, \quad \{Q_\alpha, Q_\beta\} = \{\bar{Q}_{\dot{\alpha}}, \bar{Q}_{\dot{\beta}}\} = 0 \quad (3.15)$$

The SUSY covariant derivatives are defined as

$$D_\alpha = \frac{\partial}{\partial \theta^\alpha} + i\sigma_{\alpha\dot{\beta}}^\mu \bar{\theta}^{\dot{\beta}} \partial_\mu, \quad \bar{D}_{\dot{\alpha}} = (D_\alpha)^\dagger = \frac{\partial}{\partial \bar{\theta}^{\dot{\alpha}}} + i\theta^{\beta} \sigma_\beta^\mu \dot{\alpha} \partial_\mu \quad (3.16)$$

and the commutation relations are

$$\{D_\alpha, \bar{D}_{\dot{\beta}}\} = 2i\sigma_{\alpha\dot{\beta}}^\mu \partial_\mu, \quad \{D_\alpha, D_\beta\} = \{\bar{D}_{\dot{\alpha}}, \bar{D}_{\dot{\beta}}\} = 0 \quad (3.17)$$

The SUSY covariant derivatives anticommute with the SUSY generators⁴.

Chiral superfields and vector superfields

The spin 0 bosons and spin 1/2 fermions are described using the *chiral superfield* and the spin 1 gauge bosons are described using the *vector superfields*. $V(x, \theta, \bar{\theta})$. The chiral superfield, $\Phi(x, \theta, \bar{\theta})$, satisfies the condition⁵

$$\bar{D}_{\dot{\alpha}} \Phi = 0 \quad (3.18)$$

If we redefine the new coordinates (y^μ, θ) and $(\bar{y}^\mu, \bar{\theta})$ in the superface⁶,

$$y^\mu = x^\mu + i\theta\sigma^\mu\bar{\theta}, \quad \bar{y}^\mu = x^\mu - i\theta\sigma^\mu\bar{\theta} \quad (3.19)$$

then the covariant derivatives become

$$D_\alpha = \frac{\partial}{\partial \theta^\alpha} + 2i\sigma_{\alpha\dot{\beta}}^\mu \bar{\theta}^{\dot{\beta}} \frac{\partial}{\partial y^\mu}, \quad \bar{D}_{\dot{\alpha}} = \frac{\partial}{\partial \bar{\theta}^{\dot{\alpha}}} \quad (3.20)$$

And the general form of a chiral superfield can be expressed in terms of the chiral coordinate (y^μ, θ) only

$$\Phi(y, \theta) = \phi(y) + \sqrt{2}\theta\psi(y) + \theta\theta F(y) \quad (3.21)$$

⁴ $\{D_\alpha, Q_\beta\} = \{D_\alpha, \bar{Q}_{\dot{\beta}}\} = \{\bar{D}_{\dot{\alpha}}, Q_\beta\} = \{\bar{D}_{\dot{\alpha}}, \bar{Q}_{\dot{\beta}}\} = 0$

⁵The antichiral superfield satisfies $D_\alpha \Phi^* = 0$ where Φ^* is the complex conjugate of Φ .

⁶The chiral coordinate is (y^μ, θ) and the antichiral coordinate is $(\bar{y}^\mu, \bar{\theta})$

The vector superfield, V , is a real field⁷ and the general form is

$$V(x, \theta, \bar{\theta}) = C + i\theta\chi - i\bar{\theta}\bar{\chi} + \theta\sigma^\mu\bar{\theta}v_\mu + \frac{i}{2}\theta\theta(M + iN) - \frac{i}{2}\bar{\theta}\bar{\theta}(M - iN) \quad (3.22)$$

$$+ i\theta\theta\bar{\theta}(\bar{\lambda} + \frac{i}{2}\bar{\sigma}^\mu\partial_\mu\chi) - i\bar{\theta}\bar{\theta}\theta(\lambda - \frac{i}{2}\sigma^\mu\partial_\mu\bar{\chi}) + \frac{1}{2}\theta\theta\bar{\theta}\bar{\theta}(D - \frac{1}{2}\partial^2C) \quad (3.23)$$

where the C, M, N, D are real scalars, the χ, λ are Weyl spinors, and the v_μ is a vector field. By applying the Wess-Zumino gauge, the general form can be reduced into

$$V_{WZ} = \theta\sigma^\mu\bar{\theta}v_\mu + i\theta\theta\bar{\theta}\bar{\lambda} - i\bar{\theta}\bar{\theta}\theta\lambda + \frac{1}{2}\theta\theta\bar{\theta}\bar{\theta}D \quad (3.24)$$

The non-vanishing power of V_{WZ} is $V_{WZ}^2 = \frac{1}{2}\theta\theta\bar{\theta}\bar{\theta}v_\mu v^\mu$. All the higher power of V_{WZ} are all vanishing $V_{WZ}^n = 0, n \geq 3$.

3.2.3 R -parity

The baryon number B and lepton number L are conserved in the SM but violated in the SUSY. Therefore, a new symmetry called R -parity is introduced to eliminate the B and L violating term. The R -parity is defined as

$$R \equiv (-1)^{3(B-L)+2s} \quad (3.25)$$

where s is the spin of the particle. All of the SM particles have even R -parity ($R = +1$), while all of the sparticles have odd R -parity ($R = 1$). If the R -parity is conserved, SUSY predicts that sparticles are produced in pairs in collider experiments.

3.2.4 Supersymmetry breaking

The supermultiplets are the single particle states in SUSY theory and it corresponds to the irreducible representations of the super-Poincaré algebra. A supermultiplet contains boson

⁷The vector superfield satisfies $V(x, \theta, \bar{\theta}) = V^\dagger(x, \theta, \bar{\theta})$.

and fermion with the same degrees of freedom and all particles in the same supermultiplet have the same mass. However, no any sparticles have been observed from the experiments. Therefore, the SUSY must be spontaneously broken and the sparticles must be heavier than their SM partners. The scalar superpotential V can be represented by the auxiliary fields F_i and D_a

$$V = F^{*i}F_i + \frac{1}{2} \sum_a D^a D_a \quad (3.26)$$

A state $|\Omega\rangle$ is called a vacuum state if $E_\Omega = \langle\Omega|H|\Omega\rangle = 0$. This happens when the potential V has a minimum. There are two kinds of vacuums, the true vacuum and the false vacuum which correspond to the global minimum and the local minimum of the scalar potential V , respectively. For example, when $F_i = D_a = 0$, then $V = 0$ is a global minimum. The $\langle F \rangle = 0$ is called F -term breaking and the $\langle D \rangle = 0$ is called D -term breaking.

3.2.5 The Minimal Supersymmetry Standard Model

The Minimal Supersymmetry Standard Model (MSSM) is the minimal extension of the Standard Model. The MSSM contains only the smallest number of superfields and interactions such that the SM particles can keep their current forms.

Particle content

All the super particles, *sparticles*⁸, have exactly the same quantum number as their SM particles except the spins differ by $\frac{1}{2}$. The super partners of the leptons and quarks are called *sleptons* and *squarks*. The sleptons and squarks are scalar particles with spin $s = 0$ and the left-handed and right-handed states are treated as different particles such that

⁸The super particles of the SM fermions are prefix a "s" and the super particles of the SM bosons are suffix an "*ino*". A tilde is added on the symbol of the SM particle to denote its super partner.

the SM particles and the SUSY sparticles have the same number of degree of freedom.

The super partners of gluons are *gluininos* and there are eight gluinos with spin $s = \frac{1}{2}$.

The super partners of the gauge bosons W^\pm, Z^0 , and γ , are *gauginos*. The gauginos have spin $s = \frac{1}{2}$. The super partners of the Higgs bosons⁹ are *Higgsinos*. The Higgsinos and gauginos mixing states are two *charginos* $\tilde{\chi}_1^\pm, \tilde{\chi}_2^\pm$ and four *neutralinos* $\tilde{\chi}_1^0, \tilde{\chi}_2^0, \tilde{\chi}_3^0, \tilde{\chi}_4^0$ with spin $s = \frac{1}{2}$. Table 3.1 shows the particle contents in the MSSM.

Supermultiplet	Names	Symbol	spin 0	spin 1/2	spin 1	$SU(3)_C \otimes SU(2)_L \otimes U(1)_Y$
Chiral ($\times 3$ families)	squarks, quarks	Q	$(\tilde{u}_L, \tilde{d}_L)$	(u_L, d_L)	-	$\mathbf{3} \otimes \mathbf{2} \otimes \frac{1}{6}$
		\bar{u}	\tilde{u}_R^*	u_R^\dagger	-	$\bar{\mathbf{3}} \otimes \mathbf{1} \otimes -\frac{2}{3}$
		\bar{d}	\tilde{d}_R^*	d_R^\dagger	-	$\bar{\mathbf{3}} \otimes \mathbf{1} \otimes \frac{1}{3}$
Chiral ($\times 3$ families)	sleptons, leptons	L	$(\tilde{\nu}, \tilde{e}_L)$	(ν, e_L)	-	$\mathbf{1} \otimes \mathbf{2} \otimes -\frac{1}{2}$
		\bar{e}	\tilde{e}_R^*	e_R^\dagger	-	$\mathbf{1} \otimes \mathbf{1} \otimes 1$
Chiral	Higgs, higgsinos	H_u	(H_u^+, H_u^0)	$(\tilde{H}_u^+, \tilde{H}_u^0)$	-	$\mathbf{1} \otimes \mathbf{2} \otimes +\frac{1}{2}$
		H_d	(H_d^0, H_d^-)	$(\tilde{H}_d^0, \tilde{H}_d^-)$	-	$\mathbf{1} \otimes \mathbf{2} \otimes -\frac{1}{2}$
Gauge	gluino, gluon	-	-	\tilde{g}	g	$\mathbf{8} \otimes \mathbf{1} \otimes 0$
	winos, W bosons	-	-	$\widetilde{W}^\pm, \widetilde{W}^0$	W^\pm, W^0	$\mathbf{1} \otimes \mathbf{3} \otimes 0$
	bino, B boson	-	-	\tilde{B}^0	B^0	$\mathbf{1} \otimes \mathbf{1} \otimes 0$

Table 3.1: Chiral supermultiplets and gauge supermultiplets in the MSSM. In the chiral supermultiplets, the spin 0 fields are complex scalars and the spin 1/2 fields are left-handed two-component Weyl spinors.

3.3 The radiative natural SUSY

The radiative natural SUSY (RNS) [56, 57, 58, 59] is based on MSSM and it may be valid all the way up to the GUT scale¹⁰. The RNS maintains the Higgs mass $m_H \sim 125$ GeV

⁹The Higgs sector contains two charged states H^\pm and three neutral states h^0, H^0 , and A^0 . The h^0 and H^0 are CP even state and A^0 is CP odd state.

¹⁰The GUT scale is about $m_{\text{GUT}} \approx 2 \times 10^{16}$ GeV.

and Z boson mass $m_Z = 91.2$ GeV and requires no large cancellations at the electroweak scale. It also expects the light higgsino masses to be $100 \sim 300$ GeV, the electroweak gaugino masses $300 \sim 1200$ GeV, the masses of \tilde{g} , \tilde{t} , and \tilde{b} to be $1 \sim 4$ TeV, and the masses of \tilde{u} , \tilde{d} , \tilde{s} , \tilde{c} exist in the $5 \sim 30$ TeV range.

In SUSY models, the Z boson mass can be obtained from the minimization condition on the Higgs sector scalar potential

$$\frac{m_Z^2}{2} = \frac{m_{H_d}^2 + \Sigma_d^d - (m_{H_u}^2 + \Sigma_u^u) \tan^2 \beta}{\tan^2 \beta - 1} - \mu^2 \quad (3.27)$$

where Σ_d^d and Σ_u^u are radiative corrections including the contributions from various particles and sparticles Yukawa and gauge couplings to the Higgs sector. Requiring no large cancellations means each term on the right-hand-side of Eq. (3.27) are individually comparable to the left-hand-side, $m_Z^2/2$. Therefore, no large electroweak fine-tuning (EWFT) is required to obtain $m_Z = 91.2$ GeV and leads to a model with electroweak naturalness. The EWFT parameter is defined as

$$\Delta_{EW} = \max_i \frac{|C_i|}{(m_Z^2/2)} \quad (3.28)$$

which depends only on the weak scale parameters of the theory. Low Δ_{EW} value means less fine-tuning. For example, $\Delta_{EW} = 10 \sim 30$ correspond to $3 \sim 10\%$ fine-tuning. The C_i represents C_{H_d} , C_{H_u} , C_μ , $C_{\Sigma_d^d(k)}$, and $C_{\Sigma_u^u(k)}$

$$C_{H_d} = \frac{m_{H_d}^2}{\tan^2 \beta - 1} \quad (3.29)$$

$$C_{H_u} = \frac{-m_{H_u}^2 \tan^2 \beta}{\tan^2 \beta - 1} \quad (3.30)$$

$$C_\mu = -\mu^2 \quad (3.31)$$

$$C_{\Sigma_d^d(k)} = \frac{\Sigma_d^d}{\tan^2 \beta - 1} \quad (3.32)$$

$$C_{\Sigma_u^u(k)} = \frac{-\Sigma_u^u \tan^2 \beta}{\tan^2 \beta - 1} \quad (3.33)$$

where k denotes the various loop contributions included in Eq. (3.27). In order to get a small EWFT value, $\Delta_{EW} \leq 30$, the RNS has to satisfy

- The light higgsino mass $100 < |\mu| < 300$ GeV.
- $m_{H_u}(m_{\text{GUT}}) \sim (1.3 \sim 2)m_0$. This leads to $m_{H_u}^2 \sim -\frac{m_Z^2}{2}$ at the weak scale.
- $A_0 \sim \pm 1.6m_0$. This results in large radiative corrections of \tilde{t}_i whilst maintain m_H to the ~ 125 GeV.

In the RNS framework, which allows fine-tuning at $5 \sim 10\%$ level, the masses of the higgsino-like gauginos $\tilde{\chi}_1^\pm$, $\tilde{\chi}_1^0$, and $\tilde{\chi}_2^0$ lie in 100 to 300 GeV and the mass gap between $\tilde{\chi}_2^0$ and $\tilde{\chi}_1^0$ is $10 \sim 30$ GeV. The masses of third generation squarks are $m_{\tilde{t}_1} \sim 1$ to 2 TeV and $m_{\tilde{t}_2}$, $m_{\tilde{b}_1} \sim 2$ to 4 TeV. The gluino mass, $m_{\tilde{g}}$, is about 1 to 5 TeV and the masses of first and second generation sfermions, $m_{\tilde{q}}, m_{\tilde{\ell}}$, are about 5 to 10 TeV. And the light Higgs scalar mass is keeping at 125 GeV. The typical mass spectra of RNS is shown in Fig. 3.2. The $m_{\tilde{t}_{1,2}}$ and $m_{\tilde{b}_{1,2}}$ are typically beyond 1 TeV in the RNS, so it is very difficult to detect at LHC. The light higgsino-like charginos $\tilde{\chi}_1^\pm$ and neutralinos $\tilde{\chi}_{1,2}^0$ have substantial production cross-section in the RNS, these particles are produced at large rates at LHC. Because the small mass splittings $\Delta m(\tilde{\chi}_1^\pm, \tilde{\chi}_1^0)$ and $\Delta m(\tilde{\chi}_2^0, \tilde{\chi}_1^0)$, the visible decay products tend to be at very low energies and will be hard to detect above the SM background, making the large E_T^{miss} .

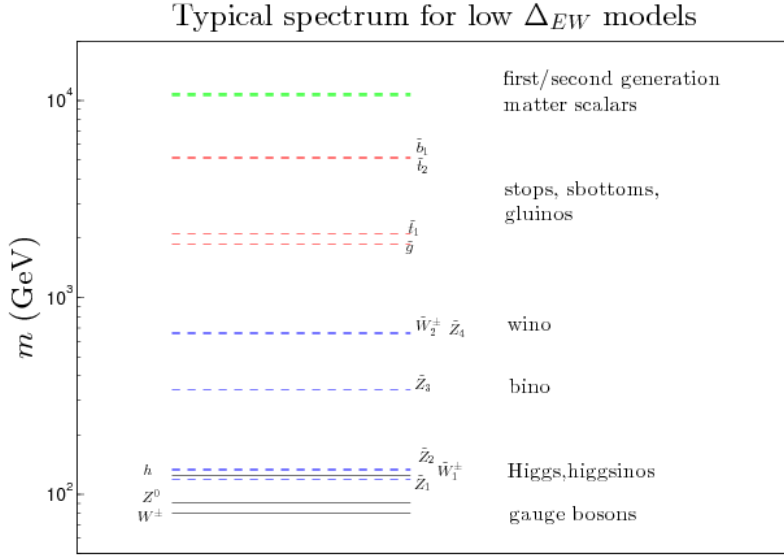


Figure 3.2: Typical sparticle mass spectra of RNS. The figure is taken from [60].

3.4 The non-universal Higgs model with two extra parameters

The RNS can be generated from SUSY GUT type models using non-universal Higgs masses model with two extra parameters (NUHM2) [61, 62, 63, 64] leading to a low fine-tuning Δ_{EW} value at the electroweak scale and keeping electroweak naturalness. The NUHM2 decouples the Higgs mass dobelet parameters $m_{H_u}^2$ and $m_{H_d}^2$ at the GUT scale such that

$$m_{H_u}^2 \neq m_{H_d}^2 \neq m_0^2(m_{\text{GUT}}) \quad (3.34)$$

and it usually uses the weak scale parameters μ and m_A to replace the $m_{H_u}^2$ and $m_{H_d}^2$.

$$\mu^2 = \frac{m_{H_d}^2 - m_{H_u}^2 \tan^2 \beta}{\tan^2 \beta - 1} - \frac{m_Z^2}{2} \quad (3.35)$$

$$m_A^2 = m_{H_d}^2 + m_{H_u}^2 + 2\mu^2 \quad (3.36)$$

If the value of NUHM2 free parameters are chosen as the following ranges

- The matter scalar mass $m_0 \sim 1$ to 7 TeV,
- The soft SUSY breaking gaugino mass $m_{1/2} \sim 0.3$ to 1.5 TeV,
- The trilinear SUSY breaking parameter $A_0 \sim \pm(1$ to 2) m_0 ,
- The ratio of the Higgs field vacuum expectation value $\tan \beta \sim 5$ to 50,
- The superpotential Higgs mass $\mu \sim 100$ to 300 GeV,
- The pseudoscalar Higgs boson mass m_A is varied.

then the low EWFT can be achieved whilst remaining SUSY spectrum and maintaining $123 < m_H < 127$ GeV. Comparing with the well-known mSUGRA/CMSSM models which have the lowest $\Delta_{EW} \sim 200$, the Δ_{EW} in the NUHM2 model is about 10 only. The NUHM2 is expected to form the effective theory for energies lower than m_{GUT} resulting from $SU(5)$ or general $SO(10)$ grand unified theories. Detailed scans for the NUHM2 parameter space with low EWFT had been performed in [56], and the NUHM2 parameter values used in this analysis are set to $m_0 = 5$ TeV, $A_0 = -1.6m_0$, $\tan \beta = 15$, $m_A = 1$ TeV, $\mu = 150$ such that $\text{sign}(\mu) > 0$, and $m_{1/2}$ are varied from 350 to 800 GeV. These parameter choices lead to low EWFT (electroweak naturalness) and predict final state signatures that allow large background rejection while retaining high signal efficiency. Although the kinematics of NUHM2 are very similar to the simplified Higgsino model in compressed scenarios, the primary differences are resulting from the mass spectra, cross-sections, and branching ratios between NUHM2 and simplified Higgsino model.

Figure 3.3 shows the $m_{1/2}$ vs μ plane of NUHM2 model for $m_0 = 5$ GeV, $\tan \beta = 15$, $A_0 = -1.6m_0$, and $m_A = 1$ TeV. The gray and blue regions are excluded by searches

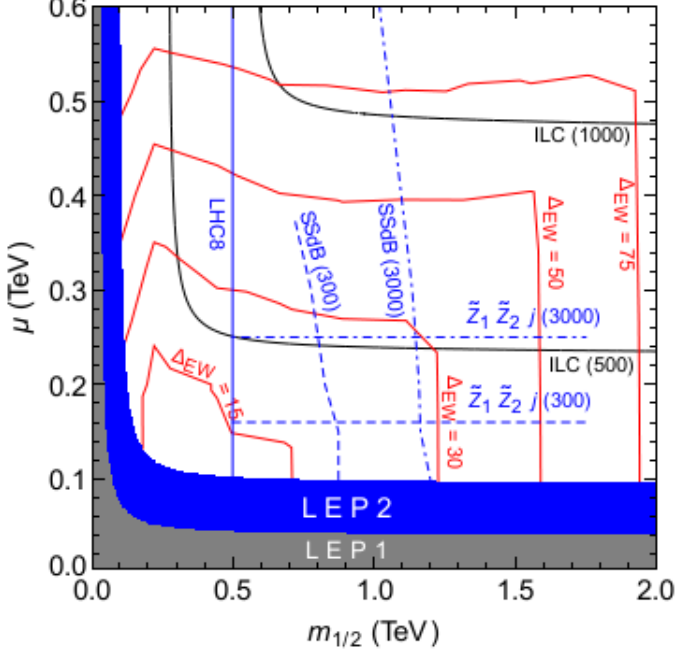


Figure 3.3: The Δ_{EW} contours in the $m_{1/2}$ vs μ plane of NUHM2 model for $m_0 = 5$ GeV, $\tan \beta = 15$, $A_0 = -1.6m_0$, and $m_A = 1$ TeV. The gray and blue shaded regions are excluded by the LEP1 and LEP2 searches for chargino pair production. The region on the left hand side of the blue solid line is excluded by LHC8 gluino pair searches. This figure is taken from [65].

for chargino pair production at LEP1 and LEP2. The area to the left of the blue solid line is excluded by the $\widetilde{g}\widetilde{g}$ production at LHC with $\sqrt{s} = 8$ TeV. The contours for $\Delta_{EW} = 15, 30, 50, 70$ are shown. The $\widetilde{\chi}_2^0\widetilde{\chi}_1^0$ with one ISR jet production where $\widetilde{\chi}_2^0 \rightarrow \ell^+\ell^-\widetilde{\chi}_1^0$ is labeled by two horizontal dashed contours at 300 fb^{-1} and 3000 fb^{-1} , respectively¹¹. The $\widetilde{\chi}_2^0\widetilde{\chi}_1^0$ with one ISR jet is accessible in nearly the entire $\Delta_{EW} < 30$ region. For comparison, the reach of International Linear Collider (ILC) with $\sqrt{s} = 0.5$ and 1 TeV are shown. Thus, the RNS, which accommodates the electroweak naturalness, can be either discovered or ruled out by the LHC plus ILC searches.

¹¹The $\widetilde{\chi}_1^0$ is indicated by \widetilde{Z}_1 and the $\widetilde{\chi}_2^0$ is indicated by \widetilde{Z}_2 in the plot.

Chapter 4

The ATLAS Experiment at LHC

The European Organisation for Nuclear Research (CERN¹) was founded in 1954 and is based in the suburb of Geneva on the Franco–Swiss border. The main function of CERN is to provide particle accelerators and detectors for high-energy physics research. The physicists and engineers at CERN are probing the fundamental structure of the universe using the world’s largest and most complex scientific facility — the *Large Hadron Collider* (LHC) [16]. In the LHC, the particles are boosted to high energies and collide at close to the speed of light. The results of the collisions are recorded by the various detectors. There are seven experiments at the LHC. The biggest of these experiments are *ATLAS* (A Toroidal LHC ApparatuS) [66] and *CMS* (Compact Muon Solenoid) [67] which use general-purpose detectors to investigate a broad physics programme ranging from the search for the Higgs boson to extra dimensions and particles that could make up dark matter. The *ALICE* (A Large Ion Collider Experiment) [68] experiment is designed to study the physics of quark-gluon plasma form and the *LHCb* (Large Hadron Collider beauty) [69] experiment specialises in investigating of CP violation² by studying the

¹The name CERN is derived from the acronym for the French Conseil Européen pour la Recherche Nucléaire.

²The CP violation is violation of the charge conjugate and parity symmetry which says if a particle is interchanged with its anti-particle and its spatial coordinates are inverted, then the physics laws should be the same.

b -quark. These four detectors sit underground in huge caverns of the LHC ring. The rest three experiments, *TOTEM* [70], *LHCf* [71], and *MoEDAL* [72], are smaller. The TOTEM (TOTal Elastic and diffractive cross section Measurement) [70] experiment aims at the measurement of total cross section, elastic scattering, and diffractive dissociation. The LHCf (Large Hadron Collider forward) [71] experiment is intended to measure the neutral particle produced by the collider using the forward particles. The prime motivation of the MoEDAL (Monopole and Exotics Detector at the LHC) [72] experiment is to search directly for the magnetic monopole. An overview of the LHC is described in Sect. 4.1 and the detector apparatus of the ATLAS experiment is outlined in Sect. 4.2.

4.1 The Large Hadron Collide

The LHC [16] is the world's largest and most powerful accelerator which accelerates and collides protons in a 26.7 km circumference crossing the Franco–Swiss border 100 m underground. Built in the tunnel of the former *LEP* (Large Electron–Positron), the LHC is capable of colliding protons as well as heavy ions. Comparing with the LEP which collides electrons and positrons, the advantage of the LHC is the lower energy loss³ in the synchrotron radiation, such that higher energies can be reached by the LHC. The LHC is designed for collisions at a centre-of-mass energy $\sqrt{s} = 14$ TeV and an instantaneous luminosity of $\mathcal{L} = 10^{34}$ cm⁻²s⁻¹. Figure 4.1 shows the infrastructure of the LHC and the pre-accelerator system.

The protons are extracted by ionisation from a hydrogen source and are accelerated to 50 MeV by the linear accelerator *LINAC2*. Then they are injected into the *Proton Synchrotron Booster* (PSB) where the proton energies are increased to 1.4 GeV before they

³The energy loss for protons is about eleven orders of magnitude smaller than the electrons.

CERN's Accelerator Complex

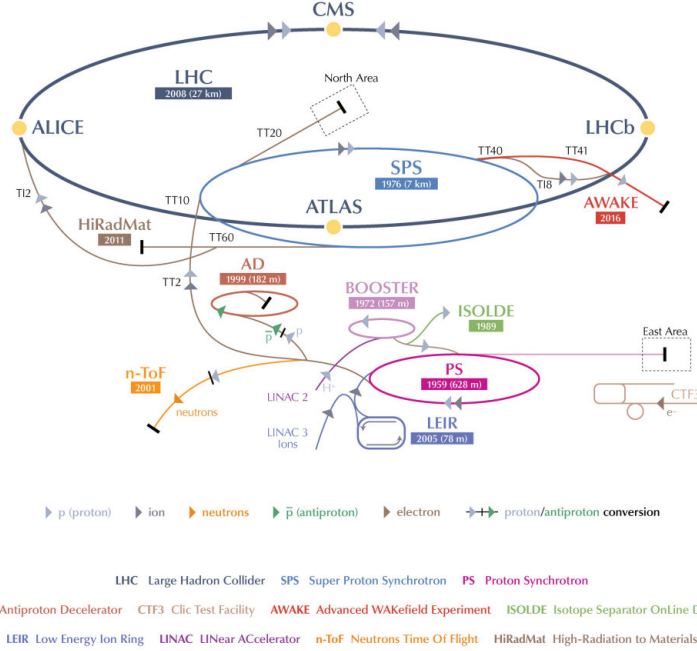


Figure 4.1: The accelerator complex at CERN [73].

enter the *Proton Synchrotron* (PS) which accelerates the protons to 25 GeV. Next, the proton energies are increasing to 450 GeV in the *Super Proton Synchrotron* (SPS). Finally, the protons are split into two beams and enter the LHC where the two beams run in two adjacent beam pipes with opposite directions. In order to keep the protons on the circular trajectory in the LHC, 1232 superconducting dipole magnets [74] generate a magnetic field strength of 8.33 T to bend the proton beams in eight arcs. Additionally, 392 quadrupole magnets [74] are installed to focus the beam. A cryogenic system running with super-fluid helium-4 is used to cool down the superconducting magnets to a temperature of 1.7 K.

For a given physics process, the event rate is proportional to the cross section σ of this process

$$\frac{dN}{dt} = \mathcal{L} \cdot \sigma \quad (4.1)$$

where N is the number of events and \mathcal{L} denotes the luminosity of the beam. The luminosity

of the beam, \mathcal{L} , can be calculated by

$$\mathcal{L} = \frac{N^2 f}{4\pi\sigma_x\sigma_y} \cdot F \quad (4.2)$$

where N is the number of protons, f is the bunches crossing frequency, and the σ_x and σ_y are the x and y components for cross section σ . The geometric luminosity reduction factor, F , is related to the crossing angle at the *interaction point* (IP). Considering a beam consisting of 1.15×10^{11} protons with bunching spacing of 25 ns, the transversal size of the bunch at IP 16×10^{-4} cm, and taking the geometric luminosity reduction factor as 1, the design luminosity of 10^{34} $\text{cm}^{-2}\text{s}^{-1}$ can be reached.

The first beam was circulated through the collider on the morning of 10 September 2008 [75]. However, a magnet quench incident occurred on 19 September 2008 and caused extensive damage to over 50 superconducting magnets, their mountings, and the vacuum pipe. Most of 2009 was spent on repairs the damage caused by the magnet quench incident and the operations resumed on 20 November of that year. The first phase of data-taking (Run 1) started at the end of 2009 and the beam energy was increased to a centre-of-mass $\sqrt{s} = 7$ TeV in 2011 and $\sqrt{s} = 8$ TeV in 2012. The total integrated luminosity of 5.46 fb^{-1} was collected in 2011 and of 22.8 fb^{-1} was collected in 2012. Since 13 February 2013 the LHC was in the Long Shutdown 1 (LS1) phase for maintenance and upgrades. On 5 April 2015, the LHC restarted and was operating at a centre-of-mass energy $\sqrt{s} = 13$ TeV throughout the Run 2 phase⁴.

⁴The Run 2 data-taking started from 2015.

4.2 The ATLAS experiment

The ATLAS⁵ detector [66] is a multi-purpose detector housed in its cavern at point 1 at the LHC [16]. It is the largest experiment at the LHC with a length of 44 m, a diameter of 25 m, and a weight of approximately 7000 tonnes. It consists of three high precision sub-detector systems which are arranged concentrically around the interaction point and in forward and backward symmetrically. Related to this symmetry, the ATLAS detector is sectioned into the central barrel region with one end-cap region perpendicular to the beam pipe on either side. Figure 4.2 shows an overview of the ATLAS detector with its major components.

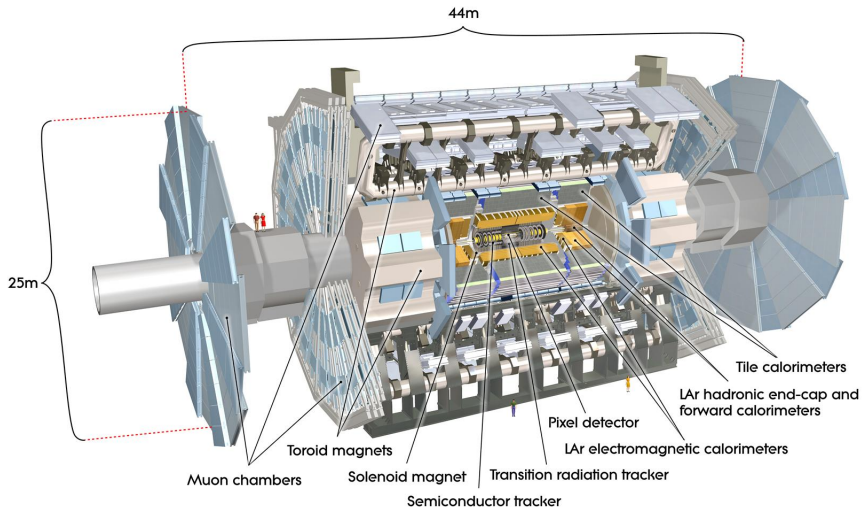


Figure 4.2: Overview of the ATLAS detector [66].

The ATLAS detector is designed to record the proton-proton interactions delivered by the LHC. It can identify particles and measure their tracks and energies with very high precision, therefore, it is sensitive to large areas of particle physics phenomena from the precision measurement of the Standard Model to beyond the Standard Model

⁵A Toroidal LHC Apparatus

(BSM). The detector is constituted by three sub-detector systems and the magnet system. The innermost part of the detector is called the *inner detector* which identifies and reconstructs the charged particles as well as the primary and secondary vertices. Around it, the *calorimeter* system is built as a cylindrical barrel with caps at each end to measure the particle energies. The detector is completed by the *muon spectrometer* which performs identification and measurement of momenta of muons. The magnetic system produces a field of $B = 0.5$ T and $B = 1$ T at barrel and two end-cap, respectively. The detector has to withstand large collision rates with approximately 1000 particles per collision, therefore, a fast readout and a three-level trigger system are implemented to reduce the event rate from 40 MHz to 200 Hz. The ATLAS coordinate system and the detail of each sub-detector systems are described in the following sections.

4.2.1 The ATLAS coordinate system

ATLAS uses a *right-handed coordinate system* with its origin at the nominal proton-proton interaction point (IP) in the centre of the detector and the z -axis along the beam pipe. Along the z -axis the detector is divided into side-A (positive z) and side-C (negative z). The positive x -axis is defined by the direction pointing from the interaction point to the centre of the LHC ring, and the positive y -axis points upward. The azimuthal angle ϕ is measured around the beam pipe and the polar angle θ is the angle from the z -axis. The transverse momentum p_T , the transverse energy E_T and the missing transverse energy E_T^{miss} are defined in the transverse plane⁶, here exemplary for p_T

$$p_T = \sqrt{p_x^2 + p_y^2} \quad (4.3)$$

⁶ $x - y$ plane

An important quantity in hadron collider physics is the *rapidity*, y , because of the invariance y under Lorentz boosts in the longitudinal direction. The rapidity is defined as

$$y = \frac{1}{2} \ln \left[\frac{E + p_z}{E - p_z} \right] \quad (4.4)$$

where E denotes the particle energy and p_z is the component of the momentum along the beam direction. Since mainly leptons can be considered massless in respect to the nominal centre-of-mass energy, the pseudorapidity, η , is used instead of using the y . For a massless particle, the *pseudorapidity*, η , depends on the polar angle θ through

$$\eta = -\ln \tan \frac{\theta}{2} \quad (4.5)$$

For a particle with the energy E much larger than its mass, the approximation $E \approx |\vec{p}|$ is valid. The distance, ΔR , between two objects in the $\eta - \phi$ plane is given by

$$\Delta R = \sqrt{\Delta\eta^2 + \Delta\phi^2} \quad (4.6)$$

where $\Delta\eta$ and $\Delta\phi$ are the difference in pseudorapidity and azimuthal angle, respectively.

4.2.2 The inner detector and tracking system

The *inner detector* (ID) consists of three sub-detectors: the *pixel* detector, the *semiconductor tracker* (SCT), and the *transition radiation tracker* (TRT). The main purpose of the inner detector is to provide high precision measurements of the tracks of particles and to reconstruct the primary and secondary vertices. Each sub-detectors are composed of several layers of material which interacts with the charged particles when the charged particles penetrate the layers. A 2 T magnetic field generated by the central solenoid parallel to the beam axis is applied to bend the charged particles using the Lorentz force. By using the radius r of the curvature of the tracks, the magnetic field strength B , and

the charge of the particle q , we can calculate the magnitude of the transverse momentum p_T

$$p_T = |q|Br \quad (4.7)$$

The layout of the inner detector is illustrated in Fig. 4.3 and the detail of sub-detectors are described in the following paragraphs.

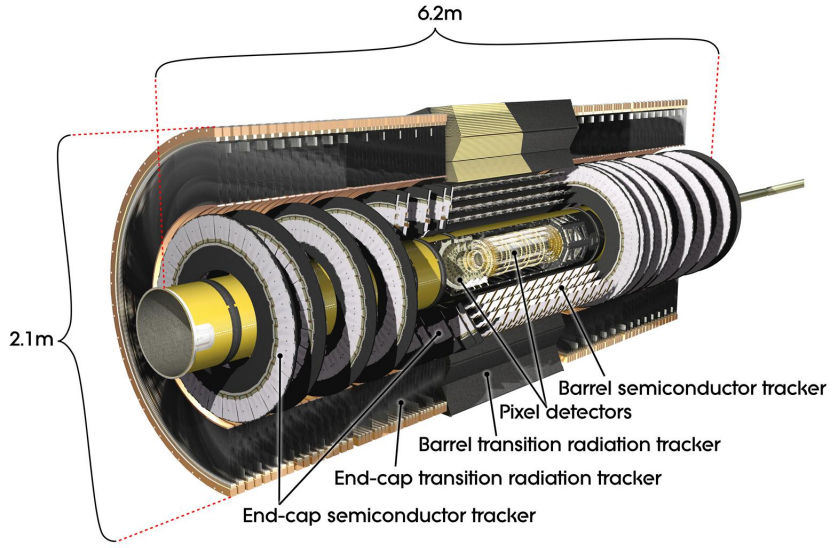


Figure 4.3: Cut-away view of the ATLAS inner detector [66].

Pixel detector

The innermost part of the entire ATLAS detector components is the *pixel* detector which is composed of three barrel layers and three end-cap disks on each side. The three cylindrical barrel layers around the beam axis have radial positions of 50.5 mm, 88.5 mm, and 122.5 mm respectively and they are made of 22, 38, and 52 identical staves respectively. Each stave is inclined with azimuthal angle of 20 degrees and is composed of 13 pixel modules with 46,080 readout channel per module. The size of each pixel is $50 \times 400 \mu m^2$ in $R - \phi \times z$. In the forward region, three disks on each side equip the modules identical

to the barrel modules, except the connecting cables. The total 1,744 modules in the pixel detector lead to nearly 80 million channel readout and provide the intrinsic accuracy of $10 \mu m$ in $R - \phi$ plane and $115 \mu m$ in z direction covering the region $|\eta| < 2.5$.

Semi conductor tracker

On the top of the pixel detector is the *semi conductor tracker* (SCT) which is a silicon strip detector. There are about 6.3 million readout channels which are arranged in 4088 microstrips. The intrinsic accuracies per sensor is $17 \mu m$ in $R - \phi$ and $580 \mu m$ in z direction for the barrel and in R for the disks, respectively. Similar to the pixel detector, the SCT covers the region $|\eta| < 2.5$ and consists of 8 strip layers in barrel and a total of 9 discs in the end-cap region on each side. No track reconstruction is possible beyond the covered pseudorapidity range. Therefore, the electrons cannot be distinguished from photons above $|\eta| > 2.5$ region.

Transition radiation tracker

The outermost component of the inner detector is the *transition radiation tracker* (TRT) which consists of 4 mm diameter straw tubes filled with the xenon-based gas mixture. The gas mixture are ionised by charged particles when they penetrates the straws. The ionised electrons drift to the cathode because a high voltage is applied on the tungsten wire in the center of the straw tube. Therefore, the TRT allows the enhanced electron identification, momentum measurement, vertex measurement. In the barrel region, the straws are surrounded by polypropylene fibres and are divided into two halves at $|\eta| = 0$. In the end-caps, the straws are arranged radially and surrounded by foils as a transition radiation element. They are read out at two sides and at the center of the TRT with the total number of the readout channels of TRT are approximately 350,000. The TRT only

provides information in the $R - \phi$ plane with an intrinsic accuracy of 130 μm per straw and covers a range up to $|\eta| < 2.0$.

Solenoid magnet

A superconducting solenoid magnet encloses the inner detector and produces a 2 T magnetic field to bend the trajectories of the charged particles. A cooling system is used and shared with the *electromagnetic calorimeter* (Sect. 4.2.3) to reduce the deterioration of the energy measurement.

4.2.3 The calorimeters

The calorimeters are used to measure the energy of particles, such as electrons, photons, and jets. Besides muons and neutrinos, all other particles interacting electromagnetically or hadronically are stopped in the calorimeters by absorbing their energy. Not only charged particles but also neutral particles such as photons and neutral hadrons can be detected in the calorimeters. By requiring highly hermiticity of the calorimeters, the missing energy $E_{\text{T}}^{\text{miss}}$ can be reconstructed precisely as negative vectorial sum of all energy deposits. The ATLAS calorimeter system is placed between the inner detector (Sect. 4.2.2) and the muon spectrometer (Sect. 4.2.4). The ATLAS calorimeter system consists of an inner *electromagnetic calorimeter* and an outer *hadronic calorimeter* together with the *forward calorimeter*. The electromagnetic calorimeter and hadronic calorimeter are *sampling calorimeters* which consist of two different materials alternately. An absorber material is used to enhance the particle showers⁷ and a highly ionisable active medium is used to measure the deposited energy. Because only the energies deposited in the

⁷The shower is the cascade of secondary particles produced by the high-energy particle interacting with dense material.

active medium can be observed, the total energy of the shower can be estimated from the deposited energy by clustering algorithms. The electromagnetic calorimeter is focusing on measuring electrons and photons, and the hadronic calorimeter is dedicated for hadronically interacting particles. The whole ATLAS calorimeter system covers a range $|\eta| < 4.9$. An layout view of the ATLAS calorimeter system is shown in Fig. 4.4 and the detail of the three calorimeters are described in the following paragraphs.

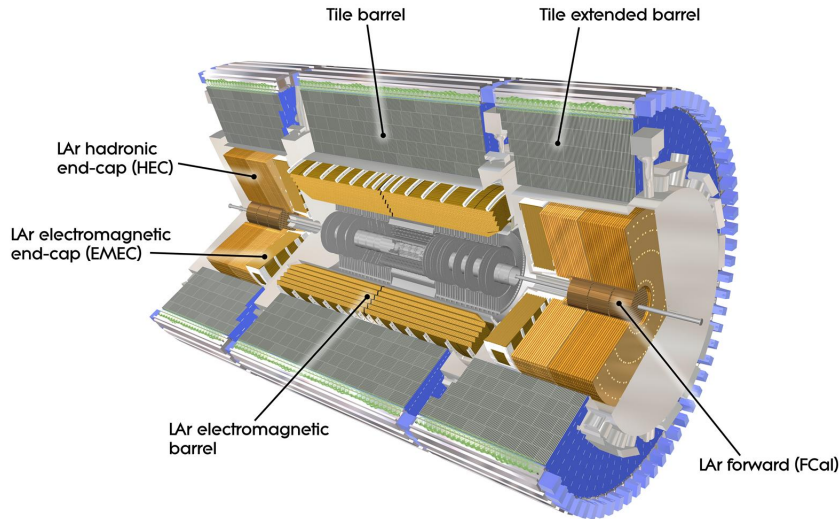


Figure 4.4: Cut-away view of the calorimeter system [66].

Electromagnetic calorimeter

The *electromagnetic calorimeter* (ECAL) measures the energy of electrons and photons as they interact with matter. The ECAL consists of accordion shaped cells of alternating layers of lead as absorber material and liquid argon (LAr) as active medium. The accordion shaped provides the full coverage in the azimuthal angle ϕ . The LAr is chosen as an active medium because it is hard to radiate, it has stable response time and linear behaviour [66]. The electrons or photons lose their energies by alternating bremsstrahlung and pair production when they interact with lead and result in the electromagnetic particle showers

which ionise the LAr and the ionisation currents are collected by the copper electrodes. The ECAL is divided into barrel (EMB) and end-cap (EMEC) components, which cover $|\eta| < 1.475$ and $1.375 < |\eta| < 3.2$ ⁸, respectively. The EMB is made up of three longitudinal layers with different granularity and sensitive in the region $|\eta| < 2.5$. The first strip layer has the highest granularity where the size of cells corresponding to $\Delta\eta \times \Delta\phi = 0.0031 \times 0.1$ for $|\eta| < 1.8$ and coarser for larger $|\eta|$. The smallest granularity allows to separate the showers coming from electrons, photons and neutral pions. The second layer is the largest part of the EMB with the size of cells corresponding to $\Delta\eta \times \Delta\phi = 0.025 \times 0.0245$ so most of the energies are deposited in this layer. The third layer has the granularity $\Delta\eta \times \Delta\phi = 0.05 \times 0.0245$. The total thickness are $22 X_0$ ⁹ and $24 X_0$ for EMB and EMECs, respectively. This special thickness is sufficient to prevent the punch-throughs of high energy showers into the muon spectrometer. Figure 4.5 shows the cut-away view of the the accordion shaped EMB module with the dimensions for three layers.

Hadronic calorimeter

The electromagnetic interacting particles produce narrow showers, however, the hadrons, which are heavier and penetrate medium further, produce more wide-spread hadronic showers. The *hadronic calorimeter* (HCAL) surrounds the ECAL and is made up by a barrel and two end-caps (HEC). The barrel covers $|\eta| < 1.7$ and it uses plastic scintillator tiles as active medium and steel as absorber material. The hadronic showers stimulate the scintillator and emit light which is collected by *photo multiplier tubes* (PMTs) and then read-out via wavelength shifting optical fibers. The HEC covers $1.5 < |\eta| < 3.2$ which overlap with the pseudorapidity coverage region of barrel. The HEC is composed of

⁸There are two EMECs and each of them consists of two wheels. The inner wheel covers $1.375 < |\eta| < 2.5$ and the outer wheel covers $2.5 < |\eta| < 3.2$.

⁹The X_0 stands for radiation lengths which is a characteristic of material. It is related to the energy loss of the particle when it interacts with the material electromagnetically.

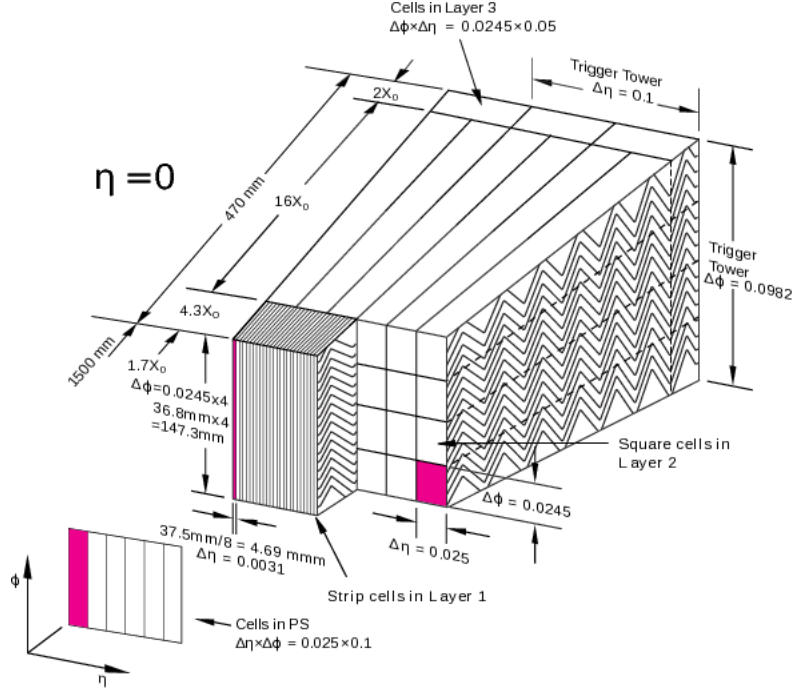


Figure 4.5: Cut-away view of the accordion shaped EM module with the dimensions for three layers [76].

two copper plate wheels as absorber material on each side and the LAr in between. The designed thickness in the barrel region is $9.7 \lambda^{10}$. Therefore, the punch-through to the muon spectrometer is suppressed. The granularity of the HCAL is coarser than the ECAL but it is sufficient for measuring E_T^{miss} and jet reconstruction.

Forward calorimeter

The *forward calorimeter* (FCAL) uses the LAr as active medium and one copper and two tungsten layers as absorber materials. The copper layer (FCAL1) is used to measure the electromagnetic interactions whereas the two tungsten layers (FCAL2 and FCAL3) is used to measure the hadronically interactions. The FCAL provides the very forward region coverage $3.1 < |\eta| < 4.9$ can contribute the E_T^{miss} measurement.

¹⁰The λ represents the hadronic interaction lengths which is the mean free path of a strongly interacting particle between two inelastic scatterings.

Energy resolution

The energy resolution is the ability of the calorimeter to distinguish the two adjacent energies. The number of ionized particles N is proportion to the energy E of the incoming particle. Therefore, the higher energy of the incoming particle the more ionised particles produced in the shower. Based on the Poisson statistics we know

$$\frac{\sigma_E}{E} \propto \frac{\sigma_N}{N} = \frac{\sqrt{N}}{N} = \frac{1}{\sqrt{N}} \propto \frac{1}{\sqrt{E}} \quad (4.8)$$

where σ_E is the energy resolution at FWHM¹¹ in a Gaussian distribution and $\sigma_N = \sqrt{N}$ is the Poisson standard deviation. Taking the effects of calibration and electronics noise into account, the relative energy resolution becomes

$$\frac{\sigma_E}{E} = \frac{a}{E} \oplus \frac{b}{\sqrt{E}} \oplus c \quad (4.9)$$

where a, b, c are noise, sampling, and constant terms, respectively. The relative energy resolutions for ECAL, HCAL, and FCAL are summarised in Table 4.1.

Calorimeter	Required resolution
Electromagnetic calorimeter	$\sigma_E/E = 10\%/\sqrt{E(\text{GeV})} \oplus 0.7\%$
Hadronic calorimeter	$\sigma_E/E = 50\%/\sqrt{E(\text{GeV})} \oplus 3\%$
Forward calorimeter	$\sigma_E/E = 100\%/\sqrt{E(\text{GeV})} \oplus 10\%$

Table 4.1: Resolution requirements for the different calorimeters of the ATLAS detector [66].

4.2.4 The muon spectrometer

The outermost part of the ATLAS detector is the *muon spectrometer* [66, 77, 78]. Muons have the same properties as electrons but 200 times heavier than the electrons. Because

¹¹The FWHM means full width at half maximum.

muons don't interact predominately by bremsstrahlung, most of the muons escape the inner detector and calorimeters without being stopped. Only the muons with an energy less than 5 GeV are stopped before the muon spectrometer. Therefore, a detector concentrates on the measurement of high precision momentum and trajectory of muons is necessary.

The muon spectrometer is designed to measure the transverse momentum (p_T) of muons with $p_T > 3$ GeV with a resolution of 3% for $p_T < 250$ GeV and increasing to 10% at 1 TeV. It consists of large toroid magnets system and high precision tracking chambers allowing a precise measurement of the muon momentum over nearly the full solid angle. The barrel toroid magnet system is composed of eight superconducting coils which are installed radial symmetrically around the beam pipe. It covers the range $|\eta| < 1.4$ and bends the trajectories of muons with the bending power 1.5 to 5.5 Tm. The magnetic field produced by the barrel toroid magnets provides an approximately 1 T field at the center of each coils, but is rather non-uniform, especially in the barrel-endcap transition region. In the endcap toroid magnets system, the magnetic field is provided by eight superconducting coils, closed in an insulation vessel extending to about 10 m in diameter, located between the first and the second station of tracking chambers. The endcap toroid magnets cover $1.6 < |\eta| < 2.4$ and provide a magnetic field in the range of 1 to 2 T with bending power 1 to 7.5 Tm.

The *monitored drift tubes* (MDT) consists of cylindrical drift tubes, filled with a gas mixture of Ar and CO₂. A tungsten-rhenium alloyed aluminium wire in the centre of each tube collects the electrons freed by ionisation of the gas volume by traversing muons. The MDT covers a full range of $|\eta| < 2.7$, while the inner layer only covers $|\eta| < 2.0$. The *cathode strip chambers* (CSC) provides a coverage range $2.0 < |\eta| < 2.7$, where MDTs would have occupancy problems. The CSC is made up by two discs and filled with Ar

and CO₂ gas mixture. Both MDT and CSC are slow for trigger but they provide high precision tracking in the spectrometer bending plane and end-cap inner layer, respectively. The *resistive plate chambers* (RPC) and *thin gap chambers* (TGC) are used for triggering in barrel and end-cap, they have sufficient intrinsic time resolution of 1.5 ns and 4 ns, respectively. A sketch of the muon spectrometer and its four components are depicted in Fig. 4.6 and Table 4.2 gives a summary of the muon spectrometer components.

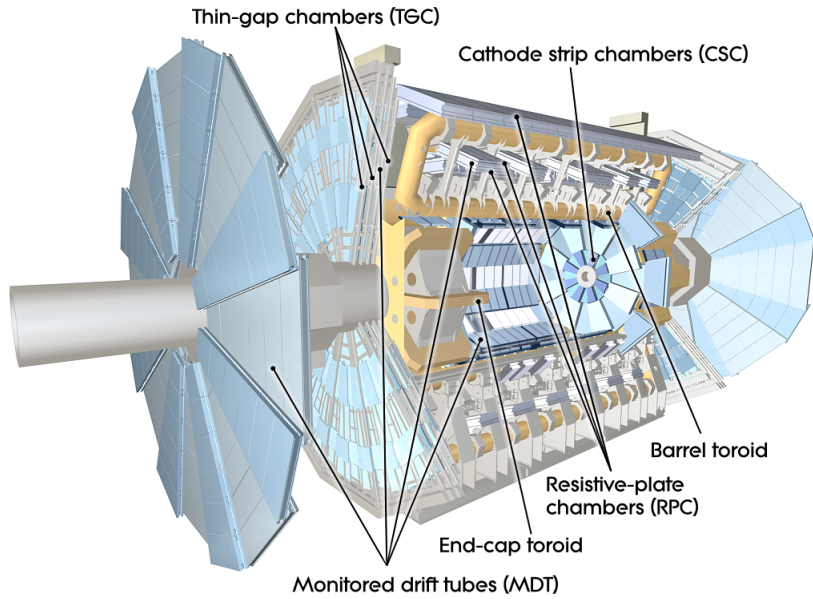


Figure 4.6: Sketch of the muon system of the ATLAS detector [66].

Type	Purpose	Location	η coverage	Channel
MDT	Tracking	barrel + end-cap	$0.0 < \eta < 2.7$	354k
CSC	Tracking	end-cap layer 1	$2.0 < \eta < 2.7$	30.7k
RPC	Trigger	barrel	$0.0 < \eta < 1.0$	373k
TGC	Trigger	end-cap	$1.0 < \eta < 2.4$	318k

Table 4.2: A summary of the muon spectrometer components.

4.2.5 The trigger system and data acquisition

The LHC pp collision rate is 40 MHz corresponding to 50 TB/s data¹² generated by the ATLAS detector [79]. However, the limited rate for writing the events into disk is about 1 kHz¹³. The majority of the products of the pp collision are low p_T QCD processes which are not the interesting events for the analysis. Hence, the three-level ATLAS trigger and data acquisition (DAQ) system is designed to pick the interesting events and reduce the data size. Figure 4.7 shows the functional view of the ATLAS trigger/DAQ system and the brief descriptions are given in the following paragraph.

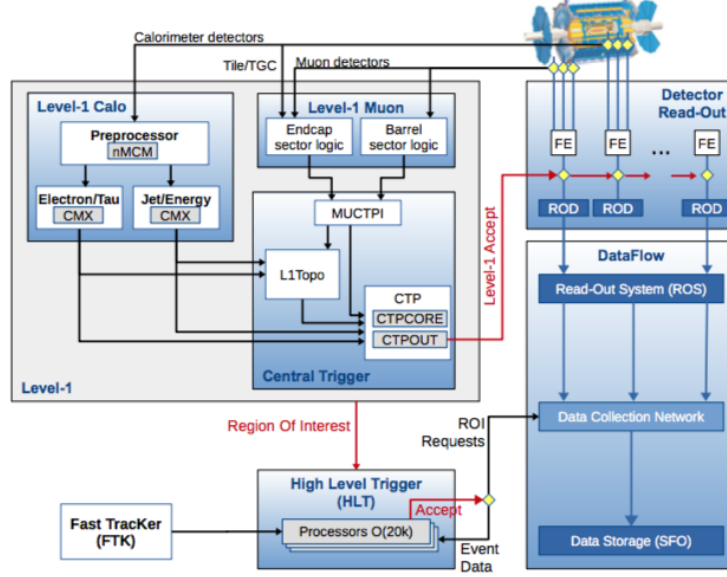


Figure 4.7: The schematic view of the ATLAS trigger/DAQ system in Run-2. The figure is taken from [80].

The level-1 trigger

The initial selection is made by the hardware-based *level-1* (LVL1) trigger based on reduced-granularity information from calorimeters and the muon spectrometer. The

¹²Assuming the typical event size is 1.3 MB.

¹³The data storage rate is 200 Hz in Run-1 but it is increased to about 1 kHz in Run-2.

latency¹⁴ of the level-1 trigger is required to be less than $2.5 \mu s$ ¹⁵. The high p_T muons are identified using only RPC and TGC. The high $p_T e/\gamma$, jets, hadronically decaying τ -leptons, large E_T^{miss} and total E_T objects are selected by calorimeter trigger using a number of sets of p_T thresholds¹⁶ and the energy isolation cuts can be applied. The selected events are read out from the front-end electronics into *readout drivers* (RODs) and written into *readout buffers* (ROBs). The information such as the p_T , η , and ϕ of the candidate objects and E_T^{miss} and total E_T are saved into *region-of-interest* (ROI) and send to the high level trigger. The level-1 trigger reduces the event rate from the high LHC bunch crossing rate to 100 kHz.

The high level trigger

The *level-2* trigger and *event filter* (EF) computer clusters used in Run-1 are merged into a single event professing *high level trigger* (HLT) farm in Run-2. This combination reduces the complexity, allows resource sharing between algorithms, and results in a more flexible HLT. The HLT is completely software based trigger system and it uses the ROI information from the level-1 trigger and the tracking information from the inner detector. The full-event track reconstruction information is performed by the *fast tracker* (FTK) system after each level-1 trigger and provided to the HLT. The trigger reconstruction algorithms for HLT were re-optimised to minimise the differences between the HLT and the offline analysis selections. The output rate of the HLT is approximately 1 kHz within a processing time about $200 \mu s$.

¹⁴The latency is the time interval from the pp collision until trigger decision is available to the front-end electronics.

¹⁵The target latency for the level-1 trigger is $2.0 \mu s$.

¹⁶Typically, there are 6 to 8 sets of thresholds per object type.

Chapter 5

Data set and simulated events

This chapter describes the collision data and simulated event samples used in searching for electroweak production of SUSY states in the compressed scenarios. The collision data are presented in Sect. 5.1 and the Monte Carlo (MC) simulated event samples are detailed in Sect. 5.2. The samples used for searching the strongly-produced SUSY particles in final states with two same-sign or three lepton and jets (SS/3L+jets) can be found in the App. D.1.

5.1 Collision data

The pp collision data used in this analysis were collected by the ATLAS detector at $\sqrt{s} = 13$ TeV during 2015 and 2016 at LHC. The data corresponds to an integrated luminosity of 36.1 fb^{-1} (3.2 fb^{-1} in 2015 and 32.9 fb^{-1} in 2016) with a combined uncertainty of 2.1% after applying beam, detector, and data-quality requirements. The combined uncertainty is derived following the methodology similar to those described in Ref. [81]. The average number of pp interactions per bunch crossing (pile-up) is 13.5 in the 2015 data set and is 25 in the 2016 data set. The data samples are required to satisfy the following good runs list (GRLs) as recommended by the ATLAS collaboration

- `data15_13TeV.periodAllYear_DetStatus-v79-repro20-02_DQDefects-00-02-02_PHYS_StandardGRL_All_Good_25ns.xml`
- `data16_13TeV.periodAllYear_DetStatus-v88-pro20-21_DQDefects-00-02-04_PHYS_StandardGRL_All_Good_25ns.xml`

Events are selected using different inclusive E_T^{miss} triggers depending on the run period as listed in Table 5.1. Two new triggers, `HLT_mu4_j125_xe90_mht` and `HLT_2mu4_j85_xe50_mht`, are developed for compressed scenarios starting from run number 308084. However, these new triggers only contribute a small gain compared to the inclusive E_T^{miss} triggers. This analysis uses inclusive E_T^{miss} triggers only.

Run period	E_T^{miss} trigger
2015	<code>HLT_xe70_mht</code>
A-D3	<code>HLT_xe90_mht.L1XE50</code>
D4-F1	<code>HLT_xe100_mht.L1XE50</code>
F1-	<code>HLT_xe110_mht.L1XE50</code>

Table 5.1: The inclusive E_T^{miss} triggers used in this analysis. The E_T^{miss} threshold varies from 70 to 110 GeV depending on the run period.

5.2 Monte Carlo simulated event samples

MC samples are used to model the SUSY signals and to estimate the SM background. All SM background MC samples were processed through a detailed ATLAS detector simulation based on GEANT4 [82] and the SUSY signal samples were simulated by a fast simulation (AF2) that parameterizes the calorimeter response [83]. To simulate the effects of additional pp collisions (pile-up) in the same and nearby bunch crossings, inelastic interactions were generated using the soft QCD processes of PYTHIA v8.186 [84] with A2 tune [85] and the MSTW2008LO PDF set [86]. These MC events were overlaid onto each

simulated hard-scatter event and reweighted to match the pile-up conditions observed in the data.

5.2.1 The SM background samples

The SHERPA 2.1.1, 2.2.1, and 2.2.2 [87] were used to produce the $Z^{(*)}/\gamma^*$ + jets, diboson, and triboson events. The matrix elements (ME) were calculated for up to two partons at next-to-leading order (NLO) and up to four partons at leading order (LO) depending on the process. The $Z^{(*)}/\gamma^*$ + jets and diboson samples cover the dilepton invariant masses from 0.5 GeV for $Z^{(*)}/\gamma^* \rightarrow e^+e^-/\mu^+\mu^-$ and from 3.8 GeV for $Z^{(*)}/\gamma^* \rightarrow \tau^+\tau^-$. The POWHEG-Box v1 and v2 interfaced to PYTHIA 6.428 were used to simulated $t\bar{t}$ and single-top production at NLO in the ME. The Higgs boson production were generated using POWHEG-Box v2 interfaced to PYTHIA 8.186. A Higgs boson in association with a W or Z boson production was simulated using MG5_AMC@NLO 2.2.2 with PYTHIA 8.186 and the ATLAS A14 tune. The processes containing $t\bar{t}$ and at least one electroweak bosons were produced using MG5_AMC@NLO 2.2.1, 2.2.2, 2.3.2, 2.3.3 with PYTHIA 6.4.28 or 8.186. These processes were generated at NLO in the ME except for $t+Z$ and $t+t\bar{t}$ which were produced at LO. Table 5.2 summarizes the event generator configurations of the ME, parton shower (PS), PDF set, and the cross-section normalization. Except those produced by SHERPA event generator, the EVTGEN v1.2.0 [88] was used to model the decay of bottom and charm hadrons in all MC samples.

5.2.2 The SUSY signal samples

The NUHM2 model allows the masses of the Higgs doublets m_{H_u} and m_{H_d} differ from the universal scalar mass m_0 at the GUT scale. The parameters of the NUHM2 model were

Process	Matrix element	Parton shower	PDF set	Cross-section
$Z^{(*)}/\gamma^* + \text{jets}$	SHERPA 2.2.1		NNPDF 3.0 NNLO	NNLO
Diboson	SHERPA 2.1.1 / 2.2.1 / 2.2.2		NNPDF 3.0 NNLO	Generator NLO
Triboson	SHERPA 2.2.1		NNPDF 3.0 NNLO	Generator LO, NLO
$t\bar{t}$	POWHEG-Box v2	PYTHIA 6.428	NLO CT10	NNLO + NNLL
t (s -channel)	POWHEG-Box v1	PYTHIA 6.428	NLO CT10	NNLO + NNLL
t (t -channel)	POWHEG-Box v1	PYTHIA 6.428	NLO CT10f4	NNLO + NNLL
$t + W$	POWHEG-Box v1	PYTHIA 6.428	NLO CT10	NNLO + NNLL
$h(\rightarrow \ell\ell, WW)$	POWHEG-Box v2	PYTHIA 8.186	NLO CTEQ6L1	NLO
$h + W/Z$	MG5_AMC@NLO 2.2.2	PYTHIA 8.186	NNPDF 2.3 LO	NLO
$t\bar{t} + W/Z/\gamma^*$	MG5_AMC@NLO 2.3.3	PYTHIA 8.186	NNPDF 3.0 LO	NLO
$t\bar{t} + WW/t\bar{t}$	MG5_AMC@NLO 2.2.2	PYTHIA 8.186	NNPDF 2.3 LO	NLO
$t + Z$	MG5_AMC@NLO 2.2.1	PYTHIA 6.428	NNPDF 2.3 LO	LO
$t + WZ$	MG5_AMC@NLO 2.3.2	PYTHIA 8.186	NNPDF 2.3 LO	NLO
$t + t\bar{t}$	MG5_AMC@NLO 2.2.2	PYTHIA 8.186	NNPDF 2.3 LO	LO

Table 5.2: The MC simulated samples of SM background process.

fixed to $m_0 = 5$ TeV, $m_A = 1$ TeV, $A_0 = -1.6m_0$, $\tan\beta = 15$, $\mu = 150$ GeV, and the $m_{1/2}$ is varied from 350 to 800 GeV as suggested in Ref. [56]. These parameter settings lead to RNS with low EWFT which keeps the Higgs boson mass about 125 GeV, the masses of \tilde{g} and \tilde{q} about TeV scale, and the light Higgsino mass about μ . The mass spectra and decay branching ratios were calculated using ISAJET v7.84 [89] and the cross-sections and the theoretical uncertainties were calculated to NLO using PROSPINO v2.1 [90].

The NUHM2 mass spectra

Figure 5.1 shows the mass spectra of the charginos $\tilde{\chi}_{1,2}^\pm$ and neutralinos $\tilde{\chi}_{1,2,3,4}^0$ as a function of $m_{1/2}$ in the NUHM2 model and the mass splitting spectra between electroweakinos as a function of $m_{1/2}$ are shown in Fig. 5.2. The masses of lower mass electroweakinos $\tilde{\chi}_{1,2}^0$ and $\tilde{\chi}_1^\pm$ are roughly flat when $m_{1/2} > 500$ GeV, however, the masses of higher mass electroweakinos $\tilde{\chi}_{3,4}^0$ and $\tilde{\chi}_2^\pm$ increased with $m_{1/2}$. The mass splittings between the lower

mass electroweakinos decrease with $m_{1/2}$ and the mass splittings between $\tilde{\chi}_3^0$ and the lower mass chargino $\tilde{\chi}_1^\pm$ or neutralinos $\tilde{\chi}_{1,2}^0$ increase with $m_{1/2}$. In the NUHM2 model, the $m_{\tilde{\chi}_1^\pm}$ doesn't set to exactly in the middle between $m_{\tilde{\chi}_1^0}$ and $m_{\tilde{\chi}_2^0}$ but it varied such that the mass ratio varies from 1.61 to 1.21 as shown in Table 5.3.

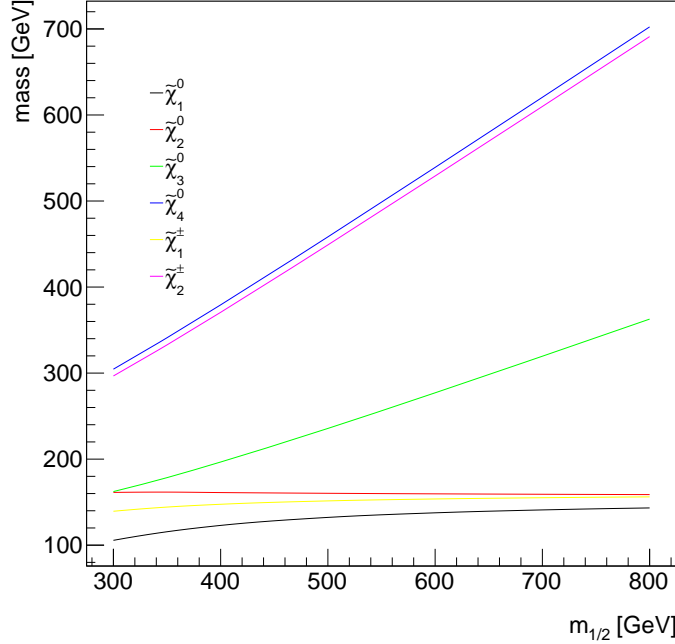


Figure 5.1: The mass spectra of the charginos $\tilde{\chi}_{1,2}^\pm$ and neutralinos $\tilde{\chi}_{1,2,3,4}^0$ as a function of $m_{1/2}$ in the NUHM2 model. The $m_{\tilde{\chi}_1^0}$, $m_{\tilde{\chi}_2^0}$, and $m_{\tilde{\chi}_1^\pm}$ are roughly flat when $m_{1/2} > 500$ GeV. The $m_{\tilde{\chi}_3^0}$, $m_{\tilde{\chi}_4^0}$, and $m_{\tilde{\chi}_2^\pm}$ are heavier and increase with $m_{1/2}$.

The NUHM2 cross-sections

The electroweakinos are divided into two categories, compressed and accessible, in the NUHM2 model. The compressed category contains the lower mass charginos $\tilde{\chi}_1^\pm$ and neutralinos $\tilde{\chi}_{1,2}^0$ and the accessible category contains the higher mass charginos $\tilde{\chi}_2^\pm$ and neutralinos $\tilde{\chi}_{3,4}^0$. Figures 5.3a and 5.3b show the cross-sections for different combinations of electroweakino production and the detail values can be found in App. A. The largest

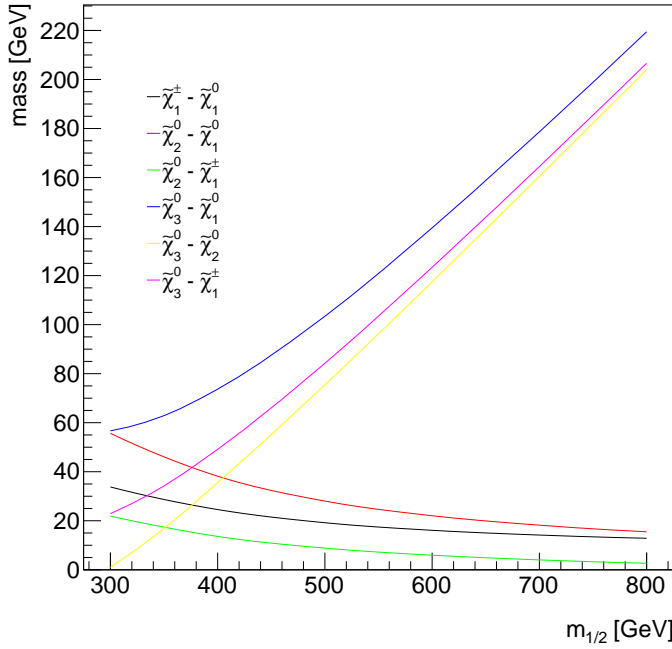


Figure 5.2: The mass splitting spectra between charginos and neutralinos in the NUHM2 model. The mass differences $\Delta m(\tilde{\chi}_3^0, \tilde{\chi}_{1,2}^0)$ and $\Delta m(\tilde{\chi}_3^0, \tilde{\chi}_1^\pm)$ increase with $m_{1/2}$. The mass differences $\Delta m(\tilde{\chi}_1^\pm, \tilde{\chi}_1^0)$, $\Delta m(\tilde{\chi}_2^0, \tilde{\chi}_1^0)$, and $\Delta m(\tilde{\chi}_2^0, \tilde{\chi}_1^\pm)$ decrease with $m_{1/2}$.

$m_{1/2}$ [GeV]	$m_{\tilde{\chi}_2^0}$ [GeV]	$m_{\tilde{\chi}_1^\pm}$ [GeV]	$m_{\tilde{\chi}_1^0}$ [GeV]	$(m_{\tilde{\chi}_2^0} - m_{\tilde{\chi}_1^\pm}) / (m_{\tilde{\chi}_1^\pm} - m_{\tilde{\chi}_1^0})$
350	161.68	144.29	115.62	1.61
400	161.14	147.54	122.97	1.55
500	160.30	151.47	132.28	1.46
600	159.66	153.71	137.61	1.37
700	159.17	155.14	140.98	1.28
800	158.78	156.14	143.29	1.21

Table 5.3: The masses of $\tilde{\chi}_1^0$, $\tilde{\chi}_2^0$, and $\tilde{\chi}_1^\pm$ and the ratios of the mass difference between $(m_{\tilde{\chi}_2^0} - m_{\tilde{\chi}_1^\pm})$ and $(m_{\tilde{\chi}_1^\pm} - m_{\tilde{\chi}_1^0})$. The $m_{\tilde{\chi}_1^\pm}$ doesn't set to the middle between $m_{\tilde{\chi}_1^0}$ and $m_{\tilde{\chi}_2^0}$.

cross-section is the compressed + compressed production and is almost independent of $m_{1/2}$. The cross-section of compressed + accessible and accessible + accessible productions are much smaller than the compressed + compressed production and they decrease quickly when $m_{1/2}$ increases. Therefore, only the different combinations of compressed production are considered in this analysis. The compressed + compressed production has cross-section about pb scale at 13 TeV, hence the Higgsino analysis is expected to have good sensitivity for NUHM2 model.

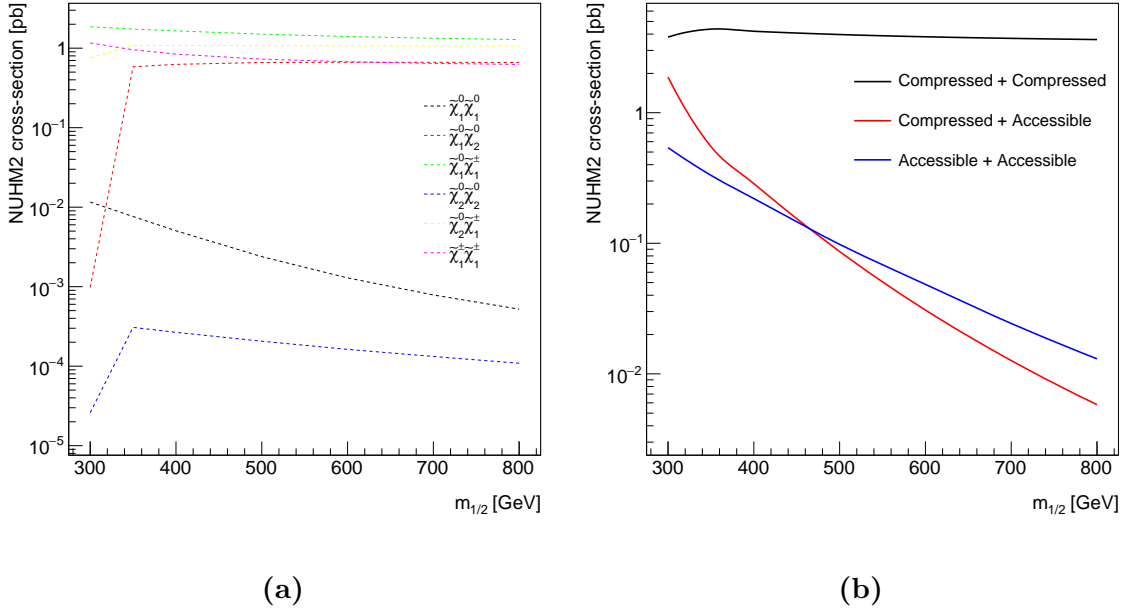


Figure 5.3: The NUHM2 cross-sections for (a) different combinations of compressed + compressed production and (b) all compressed + compressed, compressed + accessible, and accessible + accessible productions.

The NUHM2 production channels and relevant decays

The compressed category contains $\tilde{\chi}_1^\pm$, $\tilde{\chi}_1^0$, and $\tilde{\chi}_2^0$. Therefore, the compressed + compressed productions can be specified by $\tilde{\chi}_1^0 \tilde{\chi}_1^0$, $\tilde{\chi}_1^0 \tilde{\chi}_2^0$, $\tilde{\chi}_1^0 \tilde{\chi}_1^\pm$, $\tilde{\chi}_2^0 \tilde{\chi}_2^0$, $\tilde{\chi}_2^0 \tilde{\chi}_1^\pm$, and $\tilde{\chi}_1^\pm \tilde{\chi}_1^\mp$. Because the

highest sensitivity of this analysis is expected using 2 leptons, only the productions containing 2 leptons are considered. The R -parity conservation requires $\tilde{\chi}_1^0$, which is LSP, to be stable, therefore, the $\tilde{\chi}_1^0\tilde{\chi}_1^0$ production doesn't pass 2 leptons requirement. The cross-section of $\tilde{\chi}_2^0\tilde{\chi}_2^0$ production is very small so it can be neglected. The $\tilde{\chi}_1^\pm$ decays into a W^\pm and a $\tilde{\chi}_1^0$, therefore, the $\tilde{\chi}_1^0\tilde{\chi}_1^\pm$ doesn't produce 2 leptons in the final state. Only the $\tilde{\chi}_2^0\tilde{\chi}_1^0$, $\tilde{\chi}_2^0\tilde{\chi}_1^\pm$, and $\tilde{\chi}_1^\pm\tilde{\chi}_1^\mp$ productions are consider in this analysis.

The neutralino $\tilde{\chi}_2^0$ can decay into $\gamma\tilde{\chi}_1^0$, $W^\pm\tilde{\chi}_1^\mp$, $q\bar{q}\tilde{\chi}_1^0$, $\ell^+\ell^-\tilde{\chi}_1^0$, and $\nu\bar{\nu}\tilde{\chi}_1^0$. Table 5.4 lists the branching ratios for all possible $\tilde{\chi}_2^0$ decays for $m_{1/2} = 600$ GeV. Since the $\tilde{\chi}_2^0 \rightarrow \gamma\tilde{\chi}_1^0$ has very small branching ratio, this decay can be neglected.

Decay	Branching Ratio	type
$\tilde{\chi}_2^0 \rightarrow \gamma\tilde{\chi}_1^0$	$3.91677720 \times 10^{-3}$	-
$\tilde{\chi}_2^0 \rightarrow \tilde{\chi}_1^- u\bar{d}$	$7.45565048 \times 10^{-4}$	
$\tilde{\chi}_2^0 \rightarrow \tilde{\chi}_1^- \nu_e e^+$	$2.48521683 \times 10^{-4}$	
$\tilde{\chi}_2^0 \rightarrow \tilde{\chi}_1^- \nu_\mu \mu^+$	$2.48521683 \times 10^{-4}$	
$\tilde{\chi}_2^0 \rightarrow \tilde{\chi}_1^+ d\bar{u}$	$7.45565048 \times 10^{-4}$	
$\tilde{\chi}_2^0 \rightarrow \tilde{\chi}_1^+ e^- \bar{\nu}_e$	$2.48521683 \times 10^{-4}$	
$\tilde{\chi}_2^0 \rightarrow \tilde{\chi}_1^+ \mu^- \bar{\nu}_\mu$	$2.48521683 \times 10^{-4}$	$\tilde{\chi}_2^0 \rightarrow W^\pm\tilde{\chi}_1^\mp$
$\tilde{\chi}_2^0 \rightarrow \tilde{\chi}_1^- c\bar{s}$	$7.45565048 \times 10^{-4}$	
$\tilde{\chi}_2^0 \rightarrow \tilde{\chi}_1^- \nu_\tau \tau^+$	$2.48521683 \times 10^{-4}$	
$\tilde{\chi}_2^0 \rightarrow \tilde{\chi}_1^+ s\bar{c}$	$7.45565048 \times 10^{-4}$	
$\tilde{\chi}_2^0 \rightarrow \tilde{\chi}_1^+ \tau^- \bar{\nu}_\tau$	$2.48521683 \times 10^{-4}$	
$\tilde{\chi}_2^0 \rightarrow \tilde{\chi}_1^0 u\bar{u}$	$1.25538409 \times 10^{-1}$	
$\tilde{\chi}_2^0 \rightarrow \tilde{\chi}_1^0 d\bar{d}$	$1.61880091 \times 10^{-1}$	
$\tilde{\chi}_2^0 \rightarrow \tilde{\chi}_1^0 s\bar{s}$	$1.61880091 \times 10^{-1}$	$\tilde{\chi}_2^0 \rightarrow q\bar{q}\tilde{\chi}_1^0$
$\tilde{\chi}_2^0 \rightarrow \tilde{\chi}_1^0 c\bar{c}$	$1.25538409 \times 10^{-1}$	
$\tilde{\chi}_2^0 \rightarrow \tilde{\chi}_1^0 b\bar{b}$	$9.05863643 \times 10^{-2}$	
$\tilde{\chi}_2^0 \rightarrow \tilde{\chi}_1^0 e^- e^+$	$3.67224030 \times 10^{-2}$	
$\tilde{\chi}_2^0 \rightarrow \tilde{\chi}_1^0 \mu^- \mu^+$	$3.67224030 \times 10^{-2}$	$\tilde{\chi}_2^0 \rightarrow \ell^+ \ell^- \tilde{\chi}_1^0$
$\tilde{\chi}_2^0 \rightarrow \tilde{\chi}_1^0 \tau^- \tau^+$	$3.35381366 \times 10^{-2}$	
$\tilde{\chi}_2^0 \rightarrow \tilde{\chi}_1^0 \nu_e \bar{\nu}_e$	$7.30678439 \times 10^{-2}$	
$\tilde{\chi}_2^0 \rightarrow \tilde{\chi}_1^0 \nu_\mu \bar{\nu}_\mu$	$7.30678439 \times 10^{-2}$	$\tilde{\chi}_2^0 \rightarrow \nu\bar{\nu}\tilde{\chi}_1^0$
$\tilde{\chi}_2^0 \rightarrow \tilde{\chi}_1^0 \nu_\tau \bar{\nu}_\tau$	$7.30678812 \times 10^{-2}$	

Table 5.4: The possible $\tilde{\chi}_2^0$ decays in NUHM2 model with $m_{1/2} = 600$ GeV. The $\tilde{\chi}_2^0 \rightarrow \gamma\tilde{\chi}_1^0$ has the lowest branching ratio hence it is not considered in our study. The rest of the decays are catogorized into 4 types as shown in the third column.

The MC samples for the $\tilde{\chi}_2^0 \tilde{\chi}_1^\pm$ generated by pp collision are produced where four kinds of $\tilde{\chi}_2^0$ decay are specified to determine the dominant one and the $\tilde{\chi}_1^\pm$ decay is assumed to be $\tilde{\chi}_1^\pm \rightarrow W^\pm \tilde{\chi}_1^0 \rightarrow f\bar{f}\tilde{\chi}_1^0$. Since $\tilde{\chi}_2^0 \rightarrow q\bar{q}\tilde{\chi}_1^0$ and $\tilde{\chi}_2^0 \rightarrow \nu\bar{\nu}\tilde{\chi}_1^0$ do not satisfy the 2 leptons requirement, the $\tilde{\chi}_2^0$ decay should be dominated by $\tilde{\chi}_2^0 \rightarrow W^\pm \tilde{\chi}_1^\mp$ and $\tilde{\chi}_2^0 \rightarrow \ell^+\ell^-\tilde{\chi}_1^0$. Table 5.5 shows the 2 leptons filter efficiency for the $\tilde{\chi}_2^0$ decays considered, the number of events in each decay type, and the contributions to the whole $\tilde{\chi}_2^0$ decay. Because the $\tilde{\chi}_2^0 \rightarrow \ell^+\ell^-\tilde{\chi}_1^0$ contributes more than 99%, the other 3 decays can be neglected. Although $\tilde{\chi}_2^0 \rightarrow q\bar{q}\tilde{\chi}_1^0$ and $\tilde{\chi}_2^0 \rightarrow \nu\bar{\nu}\tilde{\chi}_1^0$ are expected to contribute nothing, due to the presence of the fake leptons, there are some contributions. This is expected, as no requirement on the truth matching was used in the selection.

Decay type	\mathcal{BR}	Filter efficiency			
		$pp \rightarrow \tilde{\chi}_2^0 \tilde{\chi}_1^+$	$pp \rightarrow \tilde{\chi}_2^0 \tilde{\chi}_1^-$	N_{event}	$N_{\text{event}}/N_{\text{total}}$
		$\tilde{\chi}_1^+ \rightarrow f\bar{f}\tilde{\chi}_1^0$	$\tilde{\chi}_1^- \rightarrow f\bar{f}\tilde{\chi}_1^0$		
$\tilde{\chi}_2^0 \rightarrow W^\pm \tilde{\chi}_1^\mp$	0.004473	0.117129	0.123213	1.032	0.377%
$\tilde{\chi}_2^0 \rightarrow q\bar{q}\tilde{\chi}_1^0$	0.665423	0.029174	0.028922	0.386	0.141%
$\tilde{\chi}_2^0 \rightarrow \ell^+\ell^-\tilde{\chi}_1^0$	0.106983	0.605510	0.619579	272.463	99.482%
$\tilde{\chi}_2^0 \rightarrow \nu\bar{\nu}\tilde{\chi}_1^0$	0.219204	0.009555	0.010037	0	0.0%
All $\tilde{\chi}_2^0$ decays	1	-	-	273.881	100%

Table 5.5: The 2 leptons filter efficiency for 4 kinds of $\tilde{\chi}_2^0$ decay, the number of events for each decay in $0 < m_{\ell\ell} < 50$ GeV, and the contributions to the whole $\tilde{\chi}_2^0$ decay. The transverse momentum of 2 leptons are required to be greater than 2 GeV and no E_T^{miss} requirement is applied in the filter.

The NUHM2 generation

The ISAJET 7.84 SUSY mass spectrum generator are used to calculate the NUHM2 mass spectrum. The NUHM2 signal events were generated using MG5_AMC@NLO v2.2.3 with

NNPDF23LO PDF set up to two extra partons in the ME. The MADSPIN [91] were used to decay the electroweakinos which were required to produce at least two leptons in the final state. Then the results were interfaced with PYTHIA v8.186 using the A14 tune to model the parton shower and hadronization. The PROSPINO v2.1 [92] is used to calculate the cross-section and theoretical uncertainties to the NLL level. A filter required 2 leptons of at least 3 GeV and $E_T^{\text{miss}} \geq 50$ GeV was added at the generator level. Table 5.6 lists the NUHM2 MC production samples used in this analysis. The $\tilde{\chi}_2^0 \tilde{\chi}_1^\pm$, $\tilde{\chi}_2^0 \tilde{\chi}_1^0$, and $\tilde{\chi}_1^\pm \tilde{\chi}_1^\pm$ productions are considered in each $m_{1/2}$ mass point. The relative branching ratios were calculated using SUSY-HIT v1.5b [93] and were used in the event weighting. Table 5.7 compares the branching ratios for $\tilde{\chi}_2^0 \rightarrow \ell^+ \ell^- \tilde{\chi}_1^0$ and $\tilde{\chi}_1^\pm \rightarrow \ell \bar{\nu} \tilde{\chi}_1^0$ calculating by ISAJET and SUSY-HIT. In the $\tilde{\chi}_2^0 \tilde{\chi}_1^\pm$, $\tilde{\chi}_2^0 \tilde{\chi}_1^0$ productions, the $\tilde{\chi}_2^0$ decays via $\tilde{\chi}_2^0 \rightarrow \ell^+ \ell^- \tilde{\chi}_1^0$ and the $\tilde{\chi}_1^\pm$ decays via $\tilde{\chi}_1^\pm \rightarrow f \bar{f} \tilde{\chi}_1^0$. But in the $\tilde{\chi}_1^\pm \tilde{\chi}_1^\pm$ production, the $\tilde{\chi}_1^\pm$ decays via $\tilde{\chi}_1^\pm \rightarrow \ell \bar{\nu} \tilde{\chi}_1^0$.

$m_{1/2}$ [GeV]	DSID	Production	Cross-section [pb]	Process	BF	Filter Efficiency	Relative uncertainty
350	394305	$\tilde{\chi}_1^+ \tilde{\chi}_1^-$	0.9548695995	$\tilde{\chi}_1^\pm \rightarrow l\nu \tilde{\chi}_1^0$	0.333257248	0.129920	0.07280905
350	394306	$\tilde{\chi}_2^0 \tilde{\chi}_1^-$	0.3983657446	$\tilde{\chi}_2^0 \rightarrow ll \tilde{\chi}_1^0$	0.101384714	0.252870	0.08599203
350	394307	$\tilde{\chi}_2^0 \tilde{\chi}_1^+$	0.6833463531	$\tilde{\chi}_2^0 \rightarrow ll \tilde{\chi}_1^0$	0.101384714	0.255780	0.06443308
350	394308	$\tilde{\chi}_2^0 \tilde{\chi}_1^0$	0.5835187445	$\tilde{\chi}_2^0 \rightarrow ll \tilde{\chi}_1^0$	0.101384714	0.227680	0.07193879
400	394309	$\tilde{\chi}_1^+ \tilde{\chi}_1^-$	0.8415837349	$\tilde{\chi}_1^\pm \rightarrow l\nu \tilde{\chi}_1^0$	0.333237877	0.122010	0.07397928
400	394310	$\tilde{\chi}_2^0 \tilde{\chi}_1^-$	0.3976839861	$\tilde{\chi}_2^0 \rightarrow ll \tilde{\chi}_1^0$	0.102934938	0.220640	0.08518583
400	394311	$\tilde{\chi}_2^0 \tilde{\chi}_1^+$	0.6845201512	$\tilde{\chi}_2^0 \rightarrow ll \tilde{\chi}_1^0$	0.102934938	0.223890	0.06476776
400	394312	$\tilde{\chi}_2^0 \tilde{\chi}_1^0$	0.6255603991	$\tilde{\chi}_2^0 \rightarrow ll \tilde{\chi}_1^0$	0.102934938	0.204160	0.07158509
500	394313	$\tilde{\chi}_1^+ \tilde{\chi}_1^-$	0.7280789222	$\tilde{\chi}_1^\pm \rightarrow l\nu \tilde{\chi}_1^0$	0.333195704	0.108220	0.07328355
500	394314	$\tilde{\chi}_2^0 \tilde{\chi}_1^-$	0.3955900373	$\tilde{\chi}_2^0 \rightarrow ll \tilde{\chi}_1^0$	0.105384522	0.189240	0.08416802
500	394315	$\tilde{\chi}_2^0 \tilde{\chi}_1^+$	0.6819165298	$\tilde{\chi}_2^0 \rightarrow ll \tilde{\chi}_1^0$	0.105384522	0.188060	0.06356555
500	394316	$\tilde{\chi}_2^0 \tilde{\chi}_1^0$	0.6603094819	$\tilde{\chi}_2^0 \rightarrow ll \tilde{\chi}_1^0$	0.105384522	0.176020	0.07005129
600	394317	$\tilde{\chi}_1^+ \tilde{\chi}_1^-$	0.6745140438	$\tilde{\chi}_1^\pm \rightarrow l\nu \tilde{\chi}_1^0$	0.333158828	0.100020	0.07398616
600	394318	$\tilde{\chi}_2^0 \tilde{\chi}_1^-$	0.3930396433	$\tilde{\chi}_2^0 \rightarrow ll \tilde{\chi}_1^0$	0.107603552	0.168710	0.08337329
600	394319	$\tilde{\chi}_2^0 \tilde{\chi}_1^+$	0.6791453722	$\tilde{\chi}_2^0 \rightarrow ll \tilde{\chi}_1^0$	0.107603552	0.169260	0.06375124
600	394320	$\tilde{\chi}_2^0 \tilde{\chi}_1^0$	0.6656504736	$\tilde{\chi}_2^0 \rightarrow ll \tilde{\chi}_1^0$	0.107603552	0.153530	0.07047924
700	394321	$\tilde{\chi}_1^+ \tilde{\chi}_1^-$	0.6438838471	$\tilde{\chi}_1^\pm \rightarrow l\nu \tilde{\chi}_1^0$	0.333131205	0.093538	0.07295880
700	394322	$\tilde{\chi}_2^0 \tilde{\chi}_1^-$	0.3913281838	$\tilde{\chi}_2^0 \rightarrow ll \tilde{\chi}_1^0$	0.109700775	0.158010	0.08575382
700	394323	$\tilde{\chi}_2^0 \tilde{\chi}_1^+$	0.6766070496	$\tilde{\chi}_2^0 \rightarrow ll \tilde{\chi}_1^0$	0.109700775	0.158740	0.06427279
700	394324	$\tilde{\chi}_2^0 \tilde{\chi}_1^0$	0.6643270342	$\tilde{\chi}_2^0 \rightarrow ll \tilde{\chi}_1^0$	0.109700775	0.137880	0.07021531
800	394325	$\tilde{\chi}_1^+ \tilde{\chi}_1^-$	0.6240319555	$\tilde{\chi}_1^\pm \rightarrow l\nu \tilde{\chi}_1^0$	0.333112432	0.087180	0.07242344
800	394326	$\tilde{\chi}_2^0 \tilde{\chi}_1^-$	0.3906074836	$\tilde{\chi}_2^0 \rightarrow ll \tilde{\chi}_1^0$	0.111642916	0.139150	0.08243869
800	394327	$\tilde{\chi}_2^0 \tilde{\chi}_1^+$	0.6748686972	$\tilde{\chi}_2^0 \rightarrow ll \tilde{\chi}_1^0$	0.111642916	0.146310	0.06282954
800	394328	$\tilde{\chi}_2^0 \tilde{\chi}_1^0$	0.6598118363	$\tilde{\chi}_2^0 \rightarrow ll \tilde{\chi}_1^0$	0.111642916	0.128250	0.06943069

Table 5.6: The NUHM2 MC sample dataset ID (DSID), productions, cross-sections, and decay processes and its relevant branching ratios, the filter efficiencies, and the uncertainties.

$m_{1/2}$ [GeV]	Process	Branching ratio		Difference (%)
		ISAJET	SUSY-HIT	
350	$\tilde{\chi}_1^\pm \rightarrow \ell\bar{\nu}\tilde{\chi}_1^0$	0.333335355	0.333257248	0.02
	$\tilde{\chi}_2^0 \rightarrow \ell\ell\tilde{\chi}_1^0$	0.101330683	0.101384714	0.05
400	$\tilde{\chi}_1^\pm \rightarrow \ell\bar{\nu}\tilde{\chi}_1^0$	0.333336010	0.333237877	0.03
	$\tilde{\chi}_2^0 \rightarrow \ell\ell\tilde{\chi}_1^0$	0.102880344	0.102934938	0.05
500	$\tilde{\chi}_1^\pm \rightarrow \ell\bar{\nu}\tilde{\chi}_1^0$	0.333335965	0.333195704	0.04
	$\tilde{\chi}_2^0 \rightarrow \ell\ell\tilde{\chi}_1^0$	0.105169062	0.105384522	0.20
600	$\tilde{\chi}_1^\pm \rightarrow \ell\bar{\nu}\tilde{\chi}_1^0$	0.333335682	0.333158828	0.05
	$\tilde{\chi}_2^0 \rightarrow \ell\ell\tilde{\chi}_1^0$	0.108826172	0.107603552	1.13
700	$\tilde{\chi}_1^\pm \rightarrow \ell\bar{\nu}\tilde{\chi}_1^0$	0.333335459	0.333131205	0.06
	$\tilde{\chi}_2^0 \rightarrow \ell\ell\tilde{\chi}_1^0$	0.108425085	0.109700775	1.16
800	$\tilde{\chi}_1^\pm \rightarrow \ell\bar{\nu}\tilde{\chi}_1^0$	0.333335274	0.333112432	0.07
	$\tilde{\chi}_2^0 \rightarrow \ell\ell\tilde{\chi}_1^0$	0.109469250	0.111642916	1.95

Table 5.7: The branching ratios calculated by ISAJET and SUSY-HIT. The difference are calculated with respect to the SUSY-HIT branching ratio results. Good agreement between the results from two branching ratio calculators can be seen. The largest difference between the results calculating by ISAJET and SUSY-HIT is less than 2%.

Chapter 6

Event reconstruction and selection

Candidate events are required to have at least a reconstructed pp interaction vertex with at least two $p_T > 400$ MeV associated tracks. The vertex with the largest $\sum p_T^2$ of the associated tracks is selected as the primary vertex of the event. In this chapter, the various object reconstructions and identifications in the ATLAS experiment are presented. The electron, muon, and tau objects are presented in Sect. 6.1.1, 6.1.2, and 6.1.3, respectively. Followed by the photons in Sect. 6.1.4, jets in Sect. 6.1.5, and E_T^{miss} in Sect. 6.1.6. Finally, the signal region (SR) selection is described in Sect. 6.2.

6.1 Object selections

This section presents the object definition and selection in the analysis. The general object selections for ATLAS are described followed by the specific selections used for this analysis. The definition of objects used in this analysis are based on the recommendations by Combined Performance groups and are summarized in Table 6.1. The objects are divided into two categories: preselected and signal objects where signal objects are a subset of preselected objects. Unless otherwise stated, the recommendations implemented in SUSYTools-00-08-69 [94] and AnalysisBase 2.4.37 [95] are used for all the objects.

Property	Preselected object	Signal object
Electrons		
Kinematic	$p_T > 4.5 \text{ GeV}$	$p_T > 4.5 \text{ GeV}, \eta < 2.47$ (include crack)
Identification	<code>VeryLooseLLH</code>	<code>TightLLH</code>
Isolation	-	<code>GradientLoose</code>
Impact parameter	$ z_0 \sin \theta < 0.5 \text{ mm}$	$ d_0/\sigma(d_0) < 5, z_0 \sin \theta < 0.5 \text{ mm}$
Reco algorithm	Veto <code>author==16</code>	Veto <code>author==16</code>
Muons		
Kinematic	$p_T > 4 \text{ GeV}$	$p_T > 4 \text{ GeV}, \eta < 2.5$
Identification	<code>Medium</code>	<code>Medium</code>
Isolation	-	<code>FixedCutTightTrackOnly</code>
Impact parameter	$ z_0 \sin \theta < 0.5 \text{ mm}$	$ d_0/\sigma(d_0) < 3, z_0 \sin \theta < 0.5 \text{ mm}$
Jets		
Kinematic	$p_T > 20 \text{ GeV}, \eta < 4.5$	$p_T > 30 \text{ GeV}, \eta < 2.8$
Clustering	Anti- $k_t R = 0.4$ EMTopo	Anti- $k_t R = 0.4$ EMTopo
Pileup mitigation	-	JVT <code>Medium</code> for $p_T < 60 \text{ GeV}, \eta < 2.4$
b -tagging	-	$p_T > 20 \text{ GeV}, \eta < 2.5, \text{MV2c10 FixedCutB} \approx 85\%$

Table 6.1: Summary of objec definitions used in this analysis.

6.1.1 Electrons

General electron reconstruction and identification

In the ATLAS experiment, electron¹ objects are reconstructed and identified using the information from the ID tracks matched to energy clusters in the ECAL. Electron candidates with $p_T > 4 \text{ GeV}$ and $|\eta| < 2.47$ are selected using the tag-and-probe method for $Z \rightarrow ee$ and $J/\psi \rightarrow ee$ processes. Three likelihood based electron identification algorithms, `Loose`, `Medium`, and `Tight` are applied to determine the signal-like reconstructed electron candidates. These three identifications use the same variables to define the likelihood discriminant but with different selection criteria. Depending on the electron identification used, the reconstruction efficiency varies from 78 to 90% and increases with E_T^{miss} . The

¹Electrons and positrons are collectively referred to as electrons.

electron isolation varies between 90% and 99% depending on the isolation selection criteria. More detail about the electron reconstruction performance can be found in Ref. [96] and a detail description about the electron isolation, which is my authorship project, can be found in the App. B.

Specific to this analysis

The preselected electrons used in this analysis have to satisfy $p_T > 4.5$ GeV and $|\eta| < 2.47$ and pass the likelihood-based `VeryLooseLLH` identification. The electron tracks are required to satisfy the longitudinal impact parameter $|z_0 \sin \theta| < 0.5$ mm. The electrons coming from the photon conversion are rejected by veto the `author==16`. The signal electrons have a tighter selection criteria. Besides all the requirements for the preselected electrons, the signal electrons are also required to pass `TightLLH` identification, `GradientLoose` isolation, and the transverse impact parameter $|d_0/\sigma(d_0)| < 5$ requirements.

6.1.2 Muons

General muon reconstruction and identification

In the ATLAS experiment, muon objects are reconstructed and identified using the information from ID and muon spectrometer in the $p_T > 4$ GeV and $|\eta| < 2.7$ region. Muon candidates are identified by applying quality requirements to suppress background which mainly come from pion and kion decays. Four categories of muon identification, `Medium`, `Loose`, `Tight`, and `High-p_T` are provided for different physics analyses. The `Medium` minimizes the systematic uncertainties and is provided as the default selection for muons in ATLAS. The `Loose` maximize the reconstruction efficiency and is used

for multilepton final state analyses. The `Tight` maximize the purity of muons and the `High- p_{T}` maximize the momentum resolution for $p_{\mathrm{T}} > 100$ GeV. The muon reconstruction efficiency is about 99% in $5 < p_{\mathrm{T}} < 100$ GeV and $|\eta| < 2.5$ phase space. The muon isolation efficiency varies between 93% and 100% depending on the isolation selection criteria. More detail about the muon reconstruction performance can be found in Ref. [97].

Specific to this analysis

The preselected muons used in this analysis have to satisfy $p_{\mathrm{T}} > 4$ GeV and $|\eta| < 2.5$, pass the `Medium` identification, and require $|z_0 \sin \theta| < 0.5$ mm on the longitudinal impact parameter. A tighter requirement is applied on the signal muons which in addition pass the `FixedCutTightTrackOnly` isolation together with $|d_0/\sigma(d_0)| < 3$ on the transverse impace parameter.

6.1.3 Taus

General τ reconstruction and identification

The mass of τ lepton is 1.77 GeV and the decay length is 80 μm which is too short to make τ reaches the active region of the ATLAS detector. The τ can decay either leptonically ($\tau \rightarrow \ell\nu_{\ell}$, $\ell = e, \mu$) or hadronically ($\tau \rightarrow \text{hadrons} + \nu_{\tau}$). The hadronic tau decays are about 65% of all possible decay modes and the decay products contain one charged pions (22%) or three charged pions (72%) of all cases. Tau candidates are seeded by jets using the method described in Ref. [98] and they are required to have $p_{\mathrm{T}} > 10$ GeV and $|\eta| < 2.5$ but veto the candidates in the crack region $1.37 < |\eta| < 1.52$. A boosted decision tree (BDT) based algorithm is used to identify the τ candidate and to reject backgrounds from quark- and gluon-initiated jets. Three identifications, `Loose`, `Medium`, and `Tight` are

provided with the efficiency 60%, 55%, and 45% for 1-track and 50%, 40%, and 30% for 3-tracks, respectively. More detail about the τ lepton reconstruction and identification performance can be found in Ref. [98].

Specific to this analysis

The di-tau invariant mass $m_{\tau\tau}$ is used in this analysis and addressed in Sect. 6.2.1.

6.1.4 Photons

General photons reconstruction and identification

In the ATLAS experiment, photons are reconstructed using the tracking information in ID and the energy deposits in the CAL. To distinguish prompt photons² from background photons, the photon identification is based on a set of rectangular cuts on several discriminating variables computed from the energy deposited in the ECAL and from the shower leakage to the HCAL. The photon identification is separately applied to the converted and unconverted photons with $25 \leq E_T \leq 1500$ GeV and 4 $|\eta|$ intervals. Two identifications, **Loose** and **Tight**, are provided. The **Loose** provides high efficiency with low jet rejection and the **Tight**, which is recommended for the analyses by the Combined Performance groups, provides high fake photon rejection and good efficiency. The **Tight** identification efficiency starts from 84% at low E_T and reaches around 98% in $1.37 < |\eta| < 1.81$ region for the unconverted photons. Similar to the unconverted photons, the efficiency for the converted photons increases with energy and reaches up to 98%. More detail about the photon reconstruction and identification can be found in Ref. [99].

²Prompt photons are photons not originating from hadron decays

Specific to this analysis

Photons are required to pass **Tight** identification and have $p_T > 25$ GeV.

6.1.5 Jets

General jets reconstruction

In the ATLAS experiment, jets are reconstructed using the anti- k_t algorithm with radius parameter $R = 0.4$. The reconstruction algorithm uses calorimeter topological clusters in $|\eta| < 4.5$ as input. Four jet cleaning selections, **Looser**, **Loose**, **Medium**, and **Tight**, are provided to reject the background. The **Looser** has the highest efficiency, $\sim 99.8\%$, and the **Tight** has the highest background rejection with efficiency 85% at $p_T = 25$ GeV and 98% at $p_T > 50$ GeV. More detail about the jets reconstruction using anti- k_t algorithm can be found in Ref. [100].

b-tagging

In the ATLAS experiment, it is very important to identify jets containing b hadrons from light flavor jets³. Many b -tagging algorithms were developed to maintain high b -tagging efficiency of real b -jets and to retain very low misidentification efficiency of the light flavor jets. The new developed multivariable algorithm, MV2, improving the c -jet rejection $\sim 40\%$ at 77% b -tagging efficiency and the rejection power at high b -jet p_T is also improved. More detail about the b -tagging can be found in Ref. [101, 102].

³The light flavor jets mean jets containing u , d , s , c , or gluons.

Specific to this analysis

The preselected jets are reconstructed with the anti- k_t algorithm with radius parameter $R = 0.4$ and required $p_T > 20$ GeV and $|\eta| < 4.5$. Jets with $p_T < 60$ GeV and $|\eta| < 2.4$ are required to satisfy `Medium` jet vertex tagger requirement which can suppress pileup jets. The MV2c10 b -tagging algorithm with an 85% efficiency is applied on the preselected jets with $|\eta| < 2.5$. The signal jets are required to satisfy $p_T > 30$ GeV and $|\eta| < 2.8$.

6.1.6 Missing transverse energy

The missing transverse energy E_T^{miss} is defined as the negative vector sum of p_T of all reconstructed objects including leptons, jets, and soft term as show in Eq. (6.1). The soft term is constructed from all tracks associated to the primary vertex but not associated with any physics object. There two kinds of soft term, calorimeter based soft term (CST) and track based soft term (TST) are used in E_T^{miss} calculation. The CST E_T^{miss} is constructed form the energy deposits in the CAL not associated with hard objects and the TST E_T^{miss} is built form ID tracks which not match to any reconstructed object. More detail about the E_T^{miss} reconstruction performance can be found in Ref. [103].

$$E_T^{\text{miss}} = -(\sum \mathbf{p}_T^{\text{hard}} + \mathbf{p}_T^{\text{soft}}) \quad (6.1)$$

6.1.7 Overlap removal

After preselected objects are reconstructed, an overlap removal procedure is applied to resolve ambiguities between the reconstructed jets and leptons. The distance ΔR between two objects is used for overlap removal and ΔR is defined as

$$\Delta R = \sqrt{(\Delta y)^2 + (\Delta\phi)^2} \quad (6.2)$$

where y and ϕ are rapidity and azimuthal angle, respectively. The overlap removal procedure has to follow the steps listed below. In order to avoid the bremsstrahlung from muons followed by a photon conversion into electron pairs, electron candidate is removed if it shares the same ID track with a muon object. Jet is removed from the remaining electrons if $\Delta R(\text{jets}, e) < 0.2$ unless it is a b -jet. If there are less than 3 tracks of jets with $p_T > 500$ MeV and the distance between jets and a muon candidate less than 0.4, i.e. $\Delta R(\text{jets}, \mu) < 0.4$, then the jets are removed. This step can suppress muon bremsstrahlung. Finally, the electrons and muons are removed if the e or μ lie in a distance $\Delta R(\text{jets}, e/\mu) < 0.4$ of the surviving jets so that charm and bottom hadron decays are suppressed.

6.2 Signal region selection

6.2.1 Discriminating variables

This section provides the explanations for various variables used to discriminate signals and background.

- **Same flavour opposite sign (SFOS) lepton pair:** This analysis requires exactly two preselected and two signal leptons in the final state. These two leptons have to carry the same flavor and with opposite electric charge such as $e^\pm e^\mp$ and $\mu^\pm \mu^\mp$.
- **$\mathbf{p}_T^{\ell_1}$ and $\mathbf{p}_T^{\ell_2}$:** The momentum of leading lepton $p_T^{\ell_1} > 5$ GeV is required to suppressed fake/nonprompt leptons background and the threshold of the momentum of subleading lepton $p_T^{\ell_2} > 4.5(4)$ GeV for electron (muon) is used to retain signal acceptance.
- **$\Delta\mathbf{R}_{\ell\ell}$:** The dilepton distance is defined as Eq. (6.3). The $\Delta R_{\ell\ell}$ variable, which

is required to greater than 0.05, suppresses the leptons originating from photon conversions or muons.

$$\Delta R_{\ell\ell} = \sqrt{(\eta_{\ell_1} - \eta_{\ell_2})^2 + (\phi_{\ell_1} - \phi_{\ell_2})^2} \quad (6.3)$$

- **$\mathbf{m}_{\ell\ell}$:** The dilepton invariant mass $m_{\ell\ell}$ is bounded by the mass splitting $m(\tilde{\chi}_2^0) - m(\tilde{\chi}_1^0)$ providing the background suppression power. The background originates from on-shell Z decay can be suppressed if the upper bound of $m_{\ell\ell}$ is set to 60 GeV and the contributions from J/ψ are vetoed by required a $3 < m_{\ell\ell} < 3.2$ GeV window.
- **E_T^{miss} :** In order to keep the E_T^{miss} trigger efficiency exceeding 95%, E_T^{miss} is required to be greater than 200 GeV.
- **N_{jet} :** The number of jets is required to greater than or equal to 1 because of the initial state radiation (ISR) jets.
- **$\mathbf{p}_T^{j_1}$:** The momentum of the leading jet is required to greater than 100 GeV.
- **$\Delta\phi(\mathbf{j}_1, \mathbf{p}_T^{\text{miss}})$:** The azimuthal separation between j_1 and $\mathbf{p}_T^{\text{miss}}$ is required to greater than 2 to suppress the QCD and $Z+\text{jets}$ background.
- **$\min(\Delta\phi(\text{any jet}, \mathbf{p}_T^{\text{miss}}))$:** By requiring $\Delta\phi(\text{any jet}, p_T^{\text{miss}}) > 0.4$, the effect of jet-energy mismeasurement on E_T^{miss} can be reduced.
- **$N_{\text{b-jet}}$:** Requiring $N_{\text{b-jet}} = 0$, the $t\bar{t}$ and single-top backgrounds can be reduced significantly.
- **$\mathbf{m}_{\tau\tau}$:** The di-tau invariant $m_{\tau\tau}(p_{\ell_1}, p_{\ell_2}, \mathbf{p}_T^{\text{miss}})$ variable is defined as the signed square root of $m_{\tau\tau}^2$. The $m_{\tau\tau}$ is used to reconstructed the $Z \rightarrow \tau\tau$ process where τ decays leptonically $\tau \rightarrow \ell\nu_\ell\nu_\tau$. Figure 6.1 shows the Z boson leptonic decay process. The

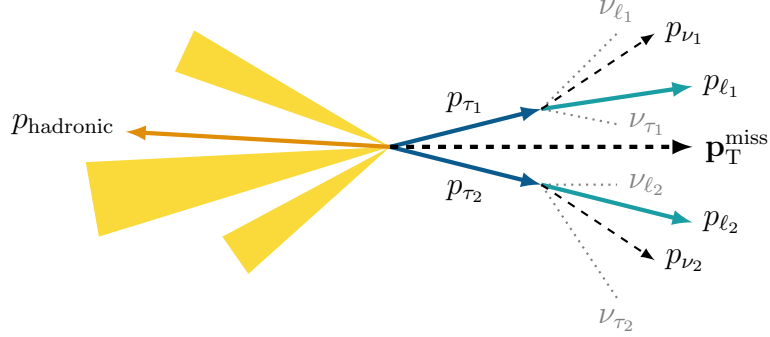


Figure 6.1: The illustration of the $Z \rightarrow \tau\tau + \text{jets}$ decay where τ decays leptonically $\tau \rightarrow \ell\nu_\ell\nu_\tau$.

$m_{\tau\tau}^2$ is defined in Eq. (6.4)

$$m_{\tau\tau}^2 \equiv 2p_{\ell_1} \cdot p_{\ell_2}(1 + \xi_1)(1 + \xi_2) \quad (6.4)$$

where p_{ℓ_1} and p_{ℓ_2} are the momenta of the leptons and the ξ_1 and ξ_2 are the scale factor which can be determined by solving $\mathbf{p}_T^{\text{miss}} = \xi_1 \mathbf{p}_T^{\ell_1} + \xi_2 \mathbf{p}_T^{\ell_2}$. From the Eq. (6.4), the $m_{\tau\tau}^2$ can be negative when either $1 + \xi_1 < 0$ or $1 + \xi_2 < 0$. This situation occurs when only one lepton moves in the same direction as $\mathbf{p}_{\text{hadronic}}$ and $|\mathbf{p}_\ell|$ is small. This rarely happens for highly boosted $Z \rightarrow \tau\tau$ decays but it happens with larger frequency for less boosted heavy particles which decays back-to-back. The $m_{\tau\tau}$ is calculated in Eq. (6.6).

$$m_{\tau\tau} = \text{sign}(m_{\tau\tau}^2) \sqrt{|m_{\tau\tau}^2|} \quad (6.5)$$

$$= \begin{cases} \sqrt{m_{\tau\tau}^2} & m_{\tau\tau}^2 \geq 0, \\ -\sqrt{|m_{\tau\tau}^2|} & m_{\tau\tau}^2 < 0. \end{cases} \quad (6.6)$$

Despite there is a discontinuity at $m_{\tau\tau} = 0$, this variable can be used to discriminate the leptons originating from $Z \rightarrow \tau\tau$.

- $\mathbf{m}_T^{\ell_1}$: The transverse mass of E_T^{miss} and the leading lepton is defined in Eq. (6.7). The

$t\bar{t}$, WW/WZ , and $W+\text{jets}$ background can be reduced by requiring $m_T^{\ell_1} < 70 \text{ GeV}$.

$$m_T^{\ell_1} = \sqrt{2(E_T^{\ell_1} E_T^{\text{miss}} - \mathbf{p}_T^{\ell_1} \cdot \mathbf{p}_T^{\text{miss}})} \quad (6.7)$$

- $E_T^{\text{miss}}/H_T^{\text{lep}}$: The scalar sum of the lepton transverse momentum, H_T^{lep} , is defined in Eq. (6.8). The H_T^{lep} variable has smaller value in the compressed SUSY signal and larger value in the SM background such as WW or WZ .

$$H_T^{\text{lep}} = p_T^{\ell_1} + p_T^{\ell_2} \quad (6.8)$$

The leptons coming from SM background, for example, $t\bar{t}$ and diboson are harder but they are softer in the compressed SUSY signal events. Therefore, for a given value of E_T^{miss} , the $E_T^{\text{miss}}/H_T^{\text{lep}}$ variable is larger in the compressed signals but is smaller for the background. The minimal requirement of this variable is defined in Eq. (6.9) which is adjusted event by event depending on the mass splitting.

$$E_T^{\text{miss}}/H_T^{\text{lep}} > \max[5, 15 - 2m_{\ell\ell}/(1 \text{ GeV})] \quad (6.9)$$

Figure 6.2 shows the $E_T^{\text{miss}}/H_T^{\text{lep}}$ requirement for the electroweakino SR after applying all the SR common requirements and the $\Delta R_{\ell\ell} < 2$.

6.2.2 Signal region

The event selection criteria for the SR are summarized in Table 6.2 and the $m_{\ell\ell}$ binnings are listed in Table 6.3. There are 14 exclusive regions and 7 inclusive regions are defined. The exclusive regions are used to set model-dependent limits while the inclusive regions are used to set the model-independent upper limits. When derive the exclusion limits on the signal model, the SRee- $m_{\ell\ell}$ and SR $\mu\mu$ - $m_{\ell\ell}$ regions are combined and fit simultaneously. The tightest inclusive region allows the mass splitting $1 \sim 3 \text{ GeV}$ is the most compressed scenario while the looser regions allow large mass splittings up to 60 GeV.

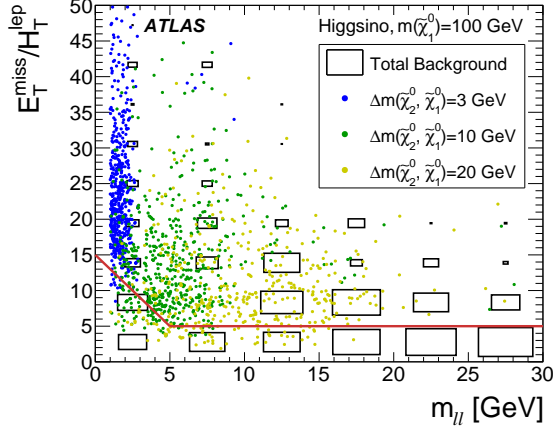


Figure 6.2: The distribution of $E_T^{\text{miss}}/H_T^{\text{lep}}$ as function of m_{ll} for the electroweakino after applying all the SR common requirements and the $\Delta R_{\ell\ell} < 2$. The red line indicates the SR selection. Events in the region below this line are rejected. The signal events are labeled in colored circles for different mass splitting.

Figure 6.3 and Fig. 6.4, show the kinematic variable distributions for the NUHM2 model with $m_{1/2} = 500 \text{ GeV}$ in $1 < \text{SR}\ell\ell - m_{ll} < 60 \text{ GeV}$. The distributions for the other $m_{1/2}$ can be found in the App. C. In order to compare the signal with background distributions, the NUHM2 distributions are multiplied by 10 but the number of events in the legend use its actual values. When making these so called ‘ $N - 1$ ’ plots, all the selections listed in Table 6.2 are applied, except the variable plotted. The bigger arrows in the upper pads presents the selection criteria of the plotting variable as listed in Table 6.2 and the uncertainty bands in the lower pads are the quadratic sum of the statistical uncertainty and a flat 20% systematic uncertainty on the backgrounds.

The cutflows is a sequential cumulative yields after the event selections. Table 6.4 and Table 6.5 shows the signal selection cutflows table for the NUHM2 signal with $m_{1/2}$ ranging from 350 to 800 GeV. The weighted number of events are normalized to 36.1 fb^{-1} and the raw number of events are also shown.

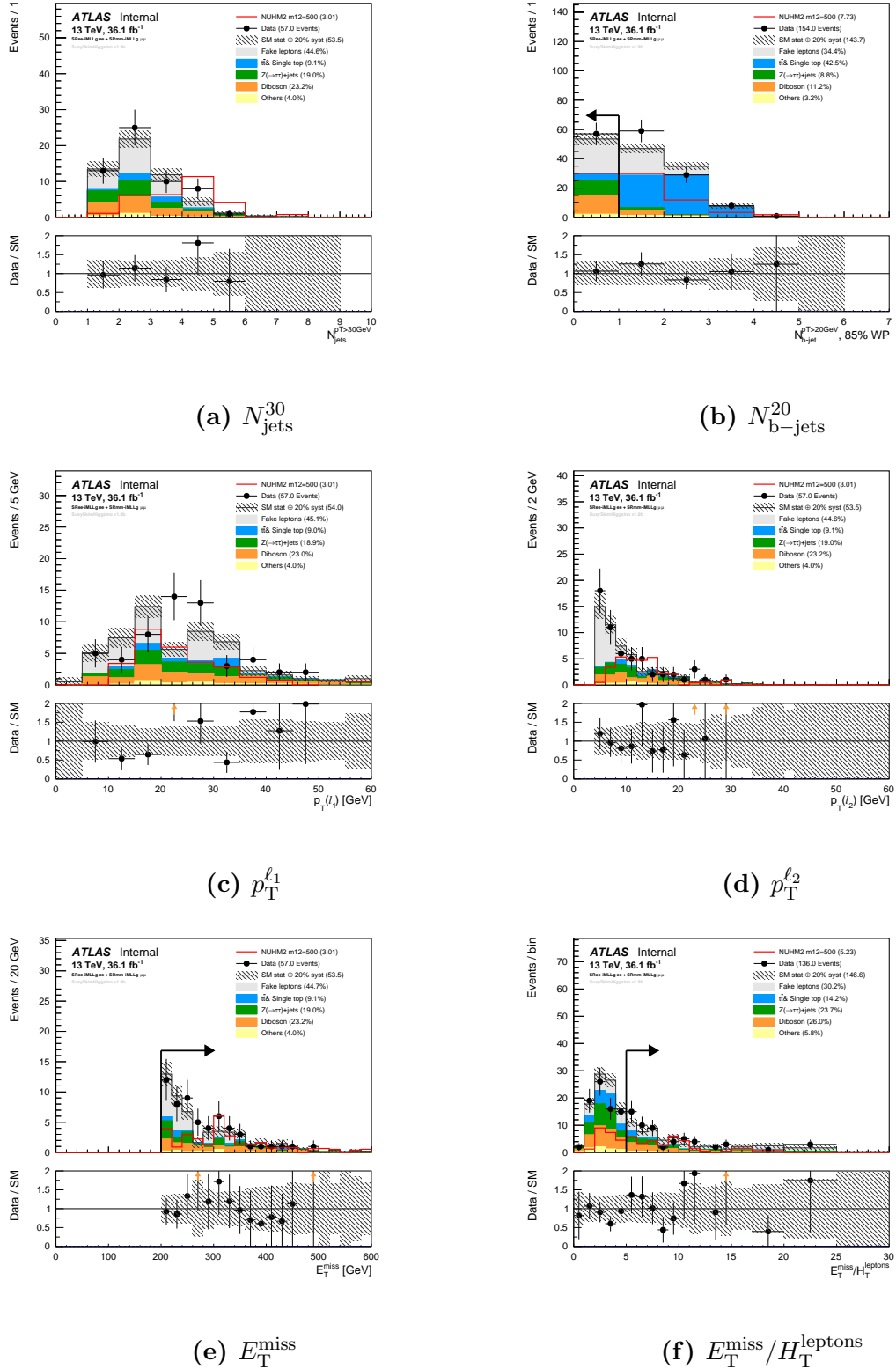


Figure 6.3: The ‘ $N - 1$ ’ distributions for NUHM2 model with $m_{1/2} = 500$ GeV in SR region

$1 < \text{SR}\ell\ell-m_{\ell\ell} < 60$ GeV. The NUHM2 distributions are multiplied by 10 but the number of events in the legend use its actual values.

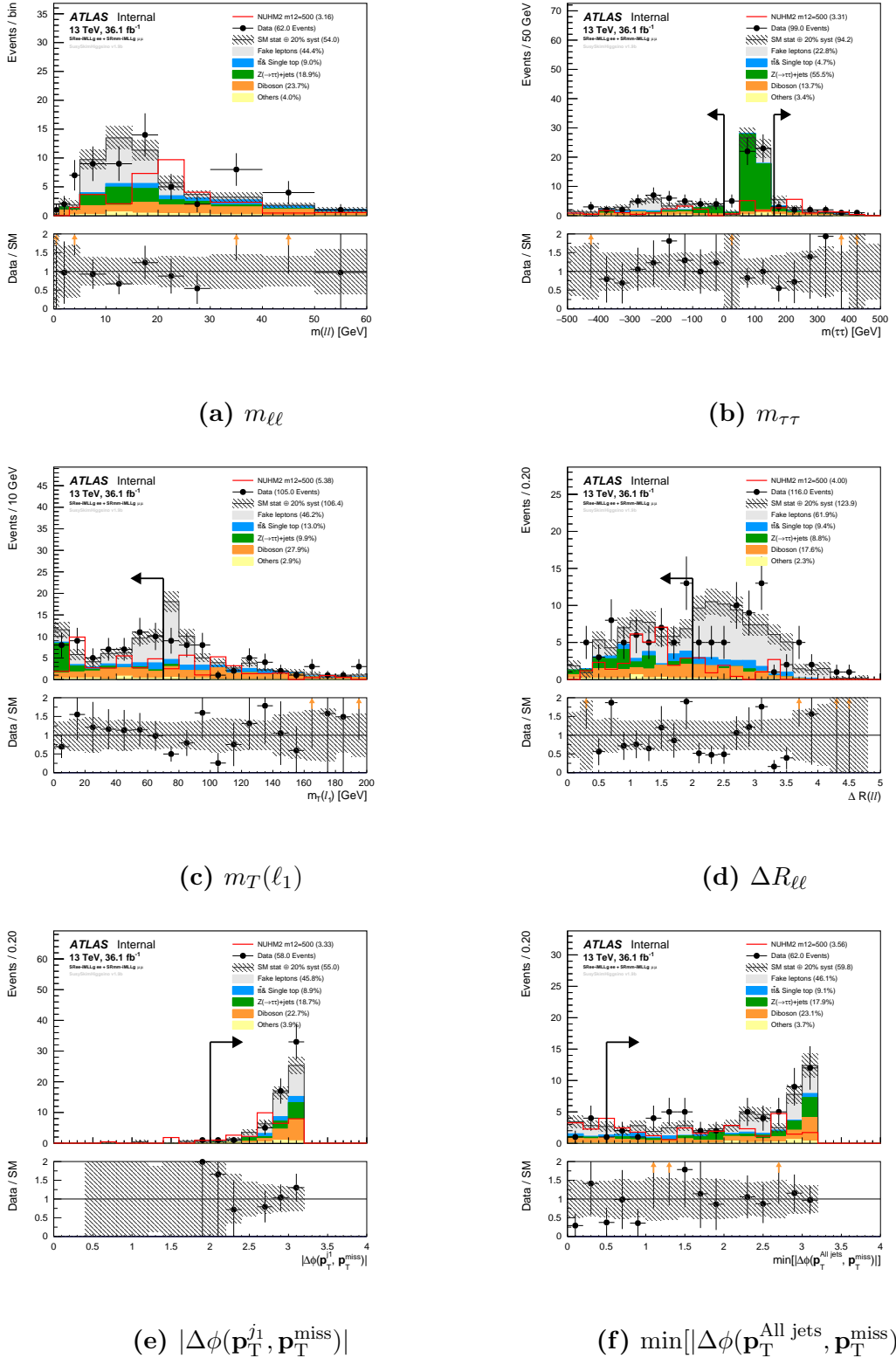


Figure 6.4: The ‘ $N - 1$ ’ distributions for NUHM2 model with $m_{1/2} = 500$ GeV in SR region

$1 < \text{SR}\ell\ell - m_{\ell\ell} < 60$ GeV. The NUHM2 distributions are multiplied by 10 but the number of events in the legend use its actual values.

Variable	Common requirement
Number of leptons	= 2
Lepton charge and flavor	e^+e^- or $\mu^+\mu^-$
Leading lepton $p_T^{\ell_1}$	> 5 GeV for electron and muon
Subleading lepton $p_T^{\ell_2}$	> 4.5 (4) GeV for electron (muon)
$\Delta R_{\ell\ell}$	> 0.05
$m_{\ell\ell}$	$\in [1, 60]$ GeV excluding [3.0, 3.2] GeV
E_T^{miss}	> 200 GeV
Number of jets	≥ 1
Leading jet p_T	> 100 GeV
$\Delta\phi(j_1, \mathbf{p}_T^{\text{miss}})$	> 2.0
$\min(\Delta\phi(\text{any jet}, \mathbf{p}_T^{\text{miss}}))$	> 0.4
Number of b -tagged jets	= 0
$m_{\tau\tau}$	< 0 or > 160 GeV
Electroweakino SRs	
$\Delta R_{\ell\ell}$	< 2
$m_T^{\ell_1}$	< 70 GeV
$E_T^{\text{miss}}/H_T^{\text{lep}}$	> $\max(5, 15 - 2 \frac{m_{\ell\ell}}{1 \text{ GeV}})$
Binned in	$m_{\ell\ell}$

Table 6.2: Summary of event selection criteria. Signal leptons and signal jets are used when applying all requirements. The SR binning is listed in Table 6.3.

Electroweakino SRs								
Exclusive	SRee- $m_{\ell\ell}$, SR $\mu\mu-m_{\ell\ell}$	[1, 3]	[3.2, 5]	[5, 10]	[10, 20]	[20, 30]	[30, 40]	[40, 60]
Inclusive	SR $\ell\ell-m_{\ell\ell}$	[1, 3]	[1, 5]	[1, 10]	[1, 20]	[1, 30]	[1, 40]	[1, 60]

Table 6.3: The SR binnings for the electroweakino SRs. The SR is defined by a $m_{\ell\ell}$ range in GeV. The exclusive bins are used to set the exclusion limits on the model and the inclusive bins are used to set the model-independent limits.

Selection common to all SRs	NUHM2 m12=350		NUHM2 m12=400		NUHM2 m12=500	
	Weighted	Raw	Weighted	Raw	Weighted	Raw
E_T^{miss} triggers, $E_T^{\text{miss}} > 150 \text{ GeV}$, $N_{\text{baseline}}^{\ell} \geq 2$	205	968	196	1262	122.7	1882
Stau veto	205	968	196	1262	122.7	1882
$N_{\text{baseline}}^{\ell} = 2$	158	741	156	975	96.5	1501
$N_{\text{signal}}^{\ell} = 2$	158	741	156	975	96.5	1501
Same flavour	94	445	100	598	64.1	1010
Opposite charge	78	369	79	503	55.1	868
Lepton truth matching	78	366	78	493	54.0	851
Lepton author 16 veto	77	364	77	487	53.8	848
$E_T^{\text{miss}} > 200 \text{ GeV}$	77	364	77	487	53.8	848
$N_{\text{b-jets}} = 0$	38.0	194	31.5	234	22.2	394
$p_T(j_1) > 100 \text{ GeV}$	38.0	194	31.5	234	22.2	394
$\Delta\phi(j_1, \mathbf{p}_T^{\text{miss}}) > 2.0$	37.3	190	30.3	223	21.0	372
$\min(\Delta\phi(\text{any jet}, \mathbf{p}_T^{\text{miss}})) > 0.4$	30.7	153	25.9	188	17.4	316
Veto $m_{\tau\tau} \in [0, 160] \text{ GeV}$	26.2	128	21.6	161	15.8	287
$p_T^{\ell_1} > 5 \text{ GeV}$	26.2	128	21.6	161	15.8	287
$m_{\ell\ell} > 1 \text{ GeV}$	26.2	128	21.6	161	15.8	287
Veto $m_{\ell\ell} \in [3, 3.2] \text{ GeV}$	26.2	128	21.6	161	15.7	286
$m_{\ell\ell} < 60 \text{ GeV}$	26.2	128	21.6	161	15.7	286
$\Delta R_{\ell\ell} > 0.05 \text{ GeV}$	26.2	128	21.5	160	15.7	286
<hr/>						
SR $\ell\ell$ - $m_{\ell\ell}$ selection						
$E_T^{\text{miss}}/H_T^{\text{lep}} > \max(5, 15 - 2 \cdot m_{\ell\ell}/\text{GeV})$	12.4	60	9.9	71	7.9	150
$\Delta R_{\ell\ell} < 2.0 \text{ GeV}$	6.5	34	6.7	51	5.6	105
$m_T^{\ell_1} < 70 \text{ GeV}$	2.7	14	2.5	21	3.0	52

Table 6.4

Selection common to all SRs	NUHM2 m12=600		NUHM2 m12=700		NUHM2 m12=800	
	Weighted	Raw	Weighted	Raw	Weighted	Raw
E_T^{miss} triggers, $E_T^{\text{miss}} > 150 \text{ GeV}$, $N_{\text{baseline}}^{\ell} \geq 2$	76.1	2321	41.2	2471	22.2	2500
Stau veto	76.1	2321	41.2	2471	22.2	2500
$N_{\text{baseline}}^{\ell} = 2$	63.0	1904	33.1	1993	18.1	2029
$N_{\text{signal}}^{\ell} = 2$	63.0	1904	33.1	1993	18.1	2029
Same flavour	42.1	1288	22.7	1383	12.6	1392
Opposite charge	35.9	1101	19.4	1194	10.9	1205
Lepton truth matching	35.2	1079	19.1	1174	10.8	1192
Lepton author 16 veto	35.2	1078	19.0	1168	10.8	1189
$E_T^{\text{miss}} > 200 \text{ GeV}$	35.2	1078	19.0	1168	10.8	1189
$N_{\text{b-jets}} = 0$	13.3	453	6.8	470	3.75	477
$p_T(j_1) > 100 \text{ GeV}$	13.3	453	6.8	470	3.75	477
$\Delta\phi(j_1, \mathbf{p}_T^{\text{miss}}) > 2.0$	12.4	428	6.5	453	3.59	455
$\min(\Delta\phi(\text{any jet}, \mathbf{p}_T^{\text{miss}})) > 0.4$	10.6	360	5.47	379	3.07	383
Veto $m_{\tau\tau} \in [0, 160] \text{ GeV}$	9.3	315	4.77	333	2.73	340
$p_T^{\ell_1} > 5 \text{ GeV}$	9.3	315	4.77	333	2.73	340
$m_{\ell\ell} > 1 \text{ GeV}$	9.3	315	4.76	332	2.72	339
Veto $m_{\ell\ell} \in [3, 3.2] \text{ GeV}$	9.3	315	4.76	332	2.71	337
$m_{\ell\ell} < 60 \text{ GeV}$	9.3	315	4.76	332	2.71	337
$\Delta R_{\ell\ell} > 0.05 \text{ GeV}$	9.3	315	4.76	332	2.71	337
<hr/>						
SR $\ell\ell$ - $m_{\ell\ell}$ selection						
$E_T^{\text{miss}}/H_T^{\text{lep}} > \max(5, 15 - 2 \cdot m_{\ell\ell}/\text{GeV})$	5.5	188	3.05	226	1.85	235
$\Delta R_{\ell\ell} < 2.0 \text{ GeV}$	4.5	153	2.55	192	1.47	194
$m_T^{\ell_1} < 70 \text{ GeV}$	2.06	78	1.21	95	0.64	85

Table 6.5

Chapter 7

Background estimation

The SM background can be categorized into the irreducible and reducible background.

The irreducible background includes events containing two prompt leptons, E_T^{miss} , and jets. The reducible background includes events containing fake or non-prompt leptons.

Since the background estimations rely on the choice of the control regions (CRs) and validation regions (VRs) heavily, the concepts of the CRs and VRs are introduced in Sect. 7.1. The detail discussions of the irreducible background is presented in Sect. 7.2 and of the reducible background is described in Sect. 7.3. Finally, the systematic uncertainty study for this analysis is mentioned in Sect. 7.4.

7.1 Control and validation regions

7.1.1 The concepts

Three different data regions are considered in any physics analysis: signal region (SR), control region (CR), and validation region (VR). The SR is a signal-enriched region, the CR is a background-enriched region, and the VR is a region used to validate the robustness of the signal and background predictions. The SR is a particular region of phase space where a set of selection criteria are applied on kinematic observables. In the

SR, the number of predicted signal events have a significant excess over the number of predicted background events. The CR is enriched in a particular background process with low expected contamination from the signals considered, designed to be similar to SR in the kinematic properties, and kept statistically independent from the SR. The background contamination in the SR can be estimated by extrapolating from the CR. The VR, usually placed in between the SR and CR, is used to validate the predicted number of background events in the SR. Figure 7.1 shows the concepts of multiple SRs, CRs, and VRs.

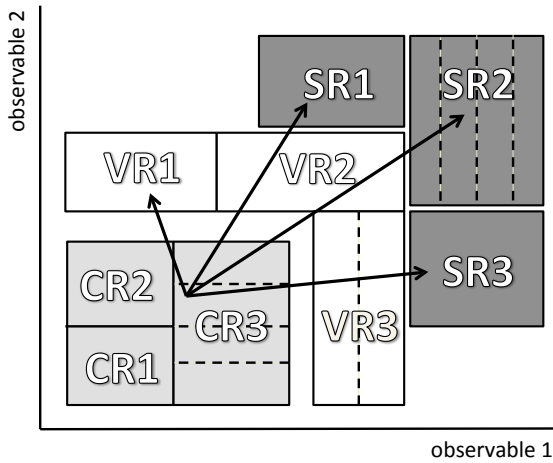


Figure 7.1: An illustration of multiple signal, control, and validation regions. The background contamination in the SRs can be estimated by extrapolating from the CRs and is verified in the VRs which lie in between the SRs and CRs. All regions can be single bin or multiple bins which are indicated by the dashed lines. The figure is taken from [104].

7.1.2 Specific to this analysis

Table 7.1 lists the SM background processes for this analysis, the origins in the SR, and the estimation strategies. Table 7.2 lists the definitions of CRs and VRs where the common

selection criteria listed in Table 6.2 have been applied.

Background process	Origin in SR	Estimation strategy
$t\bar{t}$, tW ($\rightarrow 2\ell$)	irreducible, b -jet fails identification	CR using b -tagging
$Z^{(*)}/\gamma^*(\rightarrow \tau\tau)+\text{jets}$	irreducible fully leptonic τ	CR using $m_{\tau\tau}$
$Z^{(*)}/\gamma^*(\rightarrow ee, \mu\mu)+\text{jets}$	instrumental E_T^{miss}	MC
loss mass Drell-Yen	instrumental E_T^{miss}	MC, data-driven cross check
fakes ($W+\text{jets}$, $VV(1\ell)$, $t\bar{t}$ (1ℓ))	jet fakes 2 nd lepton	fake factor, SS VR
VV	irreducible dileptonic and missed 3 rd lepton	MC, VR using $E_T^{\text{miss}}/H_T^{\text{leptons}}$
other rare processes	irreducible leptonic decays	MC

Table 7.1: The background processes for the 2ℓ analysis and the strategy for estimating the background contamination in the SR.

Region	Leptons	$E_T^{\text{miss}}/H_T^{\text{lep}}$	Additional requirements
CR-top	$e^\pm e^\mp, \mu^\pm \mu^\mp, e^\pm \mu^\mp, \mu^\pm e^\mp$	> 5	$\geq 1 b$ -tagged jet(s)
CR-tau	$e^\pm e^\mp, \mu^\pm \mu^\mp, e^\pm \mu^\mp, \mu^\pm e^\mp$	$\in [4, 8]$	$m_{\tau\tau} \in [60, 120] \text{ GeV}$
VR-VV	$e^\pm e^\mp, \mu^\pm \mu^\mp, e^\pm \mu^\mp, \mu^\pm e^\mp$	< 3	-
VR-SS	$e^\pm e^\pm, \mu^\pm \mu^\pm, e^\pm \mu^\pm, \mu^\pm e^\pm$	> 5	-
VRDF- $m_{\ell\ell}$	$e^\pm \mu^\mp, \mu^\pm e^\mp$	$> \max(5, 15 - 2 m_{\ell\ell}/1 \text{ GeV})$	$\Delta R_{\ell\ell} < 2, m_T^{\ell_1} < 70 \text{ GeV}$

Table 7.2: Definition of control regions and validation regions.

The $t\bar{t}$, tW , $Z^{(*)}/\gamma^*(\rightarrow \tau\tau)+\text{jets}$ decay to same flavor lepton pairs (ee and $\mu\mu$) and different flavor lepton pairs ($e\mu$ and μe) at the same rates. When defining the CR-top and CR-tau, all possible flavor $e^\pm e^\mp, \mu^\pm \mu^\mp, e^\pm \mu^\pm, \mu^\pm e^\mp$ are considered to enhance the statistics. By requiring the events with at least one b -tagged jet, the CR-top defined a top quarks enriched region with $\sim 72\%$ purity. The CR-top is used to estimate the $t\bar{t}$ and tW decaying to 2ℓ final states in the SR. By requiring the events satisfying $60 < m_{\tau\tau} < 120 \text{ GeV}$ and

$E_T^{\text{miss}}/H_T^{\text{lep}}$ between 4 and 8 to reduce the signal contaminations, the CR-tau defined a $Z^{(*)}/\gamma^*(\rightarrow \tau\tau)$ +jets enriched region with $\sim 80\%$ purity. The CR-tau is used to estimate the leptonic τ contaminations in the SR. Because the CAL mismeasuring jets in the $Z^{(*)}/\gamma^*(\rightarrow ee \text{ or } \mu\mu)$ +jets processes cause the high offline E_T^{miss} in the SR with very small effects, the MC samples are used to estimate the contaminations in the SR. The background of non-prompt leptons, or called fake leptons, mainly come from the $W+\text{jets}$, VV , $t\bar{t}$ processes. In these processes, a jet is misidentified as a lepton and form a dilepton final state in the SR. A data-driven method is used to estimate the fake lepton contamination in the SR. For the rare processes such as triboson and $t\bar{t} V$, their contributions in the SR are estimated using MC samples because of negligible contributions to the 2ℓ final states.

Three different VRs are constructed for this analysis. The VR-VV is used for validating diboson background, the VR-SS is used for validating same-sign dilepton background, and VRDF- $m_{\ell\ell}$ is used for validating the background come from different flavor leptons, which include both $e\mu$ and μe . By requiring $E_T^{\text{miss}}/H_T^{\text{lep}} < 3$, the signal contamination in the VR-VV is at most 8%.

7.2 Irreducible background

7.3 Reducible background

7.4 Systematic uncertainties

Chapter 8

Results

Chapter 9

Conclusion

Appendix

Appendix A

Cross-sections of NUHM2

The cross-sections, branching fraction, and filter efficiency for the NUHM2 signal samples are shown in Table [A.1](#), [A.2](#), [A.3](#), [A.4](#), [A.5](#), [A.6](#) and [A.7](#). The various final states are listed in Table [A.8](#)

DSID	Final state	Cross-section [pb]	K-factor/BF	Filter efficiency	Relative uncertainty
370617	111	0.0116116904	1.00000000	1.00000000	0.07950234
370617	112	0.0009775530	1.00000000	1.00000000	0.08535312
370617	113	0.5163867234	1.00000000	1.00000000	0.07315089
370617	114	0.0000593483	1.00000000	1.00000000	0.08483826
370617	115	1.1555478731	1.00000000	1.00000000	0.06803190
370617	116	0.0056717958	1.00000000	1.00000000	0.05803524
370617	117	0.7027932124	1.00000000	1.00000000	0.08979719
370617	118	0.0030806972	1.00000000	1.00000000	0.07709474
370617	122	0.0000260248	1.00000000	1.00000000	0.13101757
370617	123	0.1709342503	1.00000000	1.00000000	0.06993300
370617	124	0.0002175469	1.00000000	1.00000000	0.08148442
370617	125	0.4768609298	1.00000000	1.00000000	0.06541649
370617	126	0.0228714654	1.00000000	1.00000000	0.05697991
370617	127	0.2784795051	1.00000000	1.00000000	0.08434059
370617	128	0.0120807622	1.00000000	1.00000000	0.07942795
370617	133	0.0003583977	1.00000000	1.00000000	0.06910802
370617	134	0.0191236271	1.00000000	1.00000000	0.06575101
370617	135	0.6773400626	1.00000000	1.00000000	0.06477621
370617	136	0.0262277631	1.00000000	1.00000000	0.05716003
370617	137	0.3954923581	1.00000000	1.00000000	0.08483868
370617	138	0.0137758494	1.00000000	1.00000000	0.08211888
370617	144	0.0000568127	1.00000000	1.00000000	0.07453184
370617	145	0.0213534960	1.00000000	1.00000000	0.05398319
370617	146	0.2119219378	1.00000000	1.00000000	0.05665419
370617	147	0.0113003976	1.00000000	1.00000000	0.07780129
370617	148	0.1028839844	1.00000000	1.00000000	0.07544194
370617	157	1.1640104660	1.00000000	1.00000000	0.07733674
370617	158	0.0187939524	1.00000000	1.00000000	0.06417211
370617	167	0.0188413722	1.00000000	1.00000000	0.06767782
370617	168	0.1655520687	1.00000000	1.00000000	0.06249944
394301	157	1.1640104660	0.1110699593	1.4334E-01	0.07733674
394302	127	0.2784795051	0.0365485123	2.5440E-01	0.08434059
394303	125	0.4768609298	0.0365485123	2.5135E-01	0.06541649
394304	112	0.0009775530	0.0365485123	3.0251E-01	0.08535312

Table A.1: The cross-sections, branching fraction, and filter efficiency for the NUHM2 signal samples $m_{1/2} = 300$ GeV.

DSID	Final state	Cross-section [pb]	K-factor/BF	Filter efficiency	Relative uncertainty
370618	111	0.0076283799	1.00000000	1.00000000	0.07739107
370618	112	0.5835187445	1.00000000	1.00000000	0.07193879
370618	113	0.0000894312	1.00000000	1.00000000	0.09912250
370618	114	0.0001023491	1.00000000	1.00000000	0.07825966
370618	115	1.0850849571	1.00000000	1.00000000	0.07591545
370618	116	0.0049251988	1.00000000	1.00000000	0.05689268
370618	117	0.6538672654	1.00000000	1.00000000	0.08886870
370618	118	0.0025928251	1.00000000	1.00000000	0.07604635
370618	122	0.0003076705	1.00000000	1.00000000	0.06756051
370618	123	0.1082826561	1.00000000	1.00000000	0.06926016
370618	124	0.0094622361	1.00000000	1.00000000	0.06300188
370618	125	0.6833463531	1.00000000	1.00000000	0.06443308
370618	126	0.0129259483	1.00000000	1.00000000	0.05402434
370618	127	0.3983657446	1.00000000	1.00000000	0.08599203
370618	128	0.0066391822	1.00000000	1.00000000	0.07534667
370618	133	0.0000649975	1.00000000	1.00000000	0.10705877
370618	134	0.0001247362	1.00000000	1.00000000	0.07583934
370618	135	0.2353276570	1.00000000	1.00000000	0.06552596
370618	136	0.0091529911	1.00000000	1.00000000	0.05672728
370618	137	0.1357101599	1.00000000	1.00000000	0.08410482
370618	138	0.0046580255	1.00000000	1.00000000	0.07466805
370618	144	0.0000282761	1.00000000	1.00000000	0.07380597
370618	145	0.0104731869	1.00000000	1.00000000	0.05738262
370618	146	0.1421425400	1.00000000	1.00000000	0.06087756
370618	147	0.0054325991	1.00000000	1.00000000	0.07452907
370618	148	0.0669626098	1.00000000	1.00000000	0.07470349
370618	157	0.9548695995	1.00000000	1.00000000	0.07280905
370618	158	0.0093028684	1.00000000	1.00000000	0.06338077
370618	167	0.0092973351	1.00000000	1.00000000	0.06299140
370618	168	0.1082938946	1.00000000	1.00000000	0.05684157
394305	157	0.9548695995	0.111060393	1.2990E-01	0.07280905
394306	127	0.3983657446	0.101384714	2.5255E-01	0.08599203
394307	125	0.6833463531	0.101384714	2.5574E-01	0.06443308
394308	112	0.5835187445	0.101384714	2.2766E-01	0.07193879

Table A.2: The cross-sections, branching fraction, and filter efficiency for the NUHM2 signal samples $m_{1/2} = 350$ GeV.

DSID	Final state	Cross-section [pb]	K-factor/BF	Filter efficiency	Relative uncertainty
370619	111	0.0050511346	1.00000000	1.00000000	0.07579917
370619	112	0.6255603991	1.00000000	1.00000000	0.07158509
370619	113	0.0000109243	1.00000000	1.00000000	0.09579487
370619	114	0.0001052946	1.00000000	1.00000000	0.07766307
370619	115	1.0342689914	1.00000000	1.00000000	0.06820123
370619	116	0.0035382215	1.00000000	1.00000000	0.05558890
370619	117	0.6163842668	1.00000000	1.00000000	0.08756721
370619	118	0.0018044868	1.00000000	1.00000000	0.07509790
370619	122	0.0002664650	1.00000000	1.00000000	0.07041738
370619	123	0.0628066056	1.00000000	1.00000000	0.06735393
370619	124	0.0048696810	1.00000000	1.00000000	0.06286865
370619	125	0.6845201512	1.00000000	1.00000000	0.06476776
370619	126	0.0067063042	1.00000000	1.00000000	0.05627793
370619	127	0.3976839861	1.00000000	1.00000000	0.08518583
370619	128	0.0033679821	1.00000000	1.00000000	0.07318125
370619	133	0.0000557211	1.00000000	1.00000000	0.10394707
370619	134	0.0000636446	1.00000000	1.00000000	0.07539568
370619	135	0.1183185424	1.00000000	1.00000000	0.05812791
370619	136	0.0036848994	1.00000000	1.00000000	0.05773533
370619	137	0.0670198462	1.00000000	1.00000000	0.08128406
370619	138	0.0018161476	1.00000000	1.00000000	0.07634830
370619	144	0.0000158930	1.00000000	1.00000000	0.07992644
370619	145	0.0054376416	1.00000000	1.00000000	0.05587952
370619	146	0.0976478188	1.00000000	1.00000000	0.06106615
370619	147	0.0027346724	1.00000000	1.00000000	0.07262348
370619	148	0.0442265190	1.00000000	1.00000000	0.07409153
370619	157	0.8415837349	1.00000000	1.00000000	0.07397928
370619	158	0.0047908009	1.00000000	1.00000000	0.06312184
370619	167	0.0047973169	1.00000000	1.00000000	0.06465433
370619	168	0.0724744359	1.00000000	1.00000000	0.06197995
394309	157	0.8415837349	0.111047482	1.2199E-01	0.07397928
394310	127	0.3976839861	0.102934938	2.2044E-01	0.08518583
394311	125	0.6845201512	0.102934938	2.2387E-01	0.06476776
394312	112	0.6255603991	0.102934938	2.0415E-01	0.07158509

Table A.3: The cross-sections, branching fraction, and filter efficiency for the NUHM2 signal samples $m_{1/2} = 400$ GeV.

DSID	Final state	Cross-section [pb]	K-factor/BF	Filter efficiency	Relative uncertainty
370620	111	0.0023867653	1.00000000	1.00000000	0.07209579
370620	112	0.6603094819	1.00000000	1.00000000	0.07005129
370620	113	0.0001325585	1.00000000	1.00000000	0.07482547
370620	114	0.0000688236	1.00000000	1.00000000	0.07197169
370620	115	0.9426500411	1.00000000	1.00000000	0.06460091
370620	116	0.0015013209	1.00000000	1.00000000	0.06183960
370620	117	0.5588686815	1.00000000	1.00000000	0.08560539
370620	118	0.0007279662	1.00000000	1.00000000	0.07490627
370620	122	0.0002061240	1.00000000	1.00000000	0.07176449
370620	123	0.0211437195	1.00000000	1.00000000	0.06388222
370620	124	0.0014907193	1.00000000	1.00000000	0.06151866
370620	125	0.6819165298	1.00000000	1.00000000	0.06356555
370620	126	0.0021061945	1.00000000	1.00000000	0.05664429
370620	127	0.3955900373	1.00000000	1.00000000	0.08416802
370620	128	0.0010081829	1.00000000	1.00000000	0.07123419
370620	133	0.0000195970	1.00000000	1.00000000	0.10671913
370620	134	0.0000176193	1.00000000	1.00000000	0.07871367
370620	135	0.0340389859	1.00000000	1.00000000	0.05924527
370620	136	0.0006926196	1.00000000	1.00000000	0.05800427
370620	137	0.0187411871	1.00000000	1.00000000	0.08099696
370620	138	0.0003229659	1.00000000	1.00000000	0.07606581
370620	144	0.0000098797	1.00000000	1.00000000	0.07455477
370620	145	0.0016797877	1.00000000	1.00000000	0.05654557
370620	146	0.0453186981	1.00000000	1.00000000	0.06092776
370620	147	0.0008077861	1.00000000	1.00000000	0.07385221
370620	148	0.0192295608	1.00000000	1.00000000	0.07792430
370620	157	0.7280789222	1.00000000	1.00000000	0.07328355
370620	158	0.0014642018	1.00000000	1.00000000	0.06676658
370620	167	0.0014587803	1.00000000	1.00000000	0.06499176
370620	168	0.0324683300	1.00000000	1.00000000	0.06503155
394313	157	0.7280789222	0.111019377	1.0812E-01	0.07328355
394314	127	0.3955900373	0.105384522	1.8923E-01	0.08416802
394315	125	0.6819165298	0.105384522	1.8805E-01	0.06356555
394316	112	0.6603094819	0.105384522	1.7600E-01	0.07005129

Table A.4: The cross-sections, branching fraction, and filter efficiency for the NUHM2 signal samples $m_{1/2} = 500$ GeV.

DSID	Final state	Cross-section [pb]	K-factor/BF	Filter efficiency	Relative uncertainty
370621	111	0.0012897690	1.00000000	1.00000000	0.07308455
370621	112	0.6656504736	1.00000000	1.00000000	0.07047924
370621	113	0.0001361496	1.00000000	1.00000000	0.07047382
370621	114	0.0000378018	1.00000000	1.00000000	0.07036880
370621	115	0.8824882181	1.00000000	1.00000000	0.06538492
370621	116	0.0006132703	1.00000000	1.00000000	0.05826096
370621	117	0.5187808653	1.00000000	1.00000000	0.08546879
370621	118	0.0002849360	1.00000000	1.00000000	0.07563404
370621	122	0.0001627043	1.00000000	1.00000000	0.06980768
370621	123	0.0078958339	1.00000000	1.00000000	0.06365983
370621	124	0.0005370949	1.00000000	1.00000000	0.06338450
370621	125	0.6791453722	1.00000000	1.00000000	0.06375124
370621	126	0.0007771667	1.00000000	1.00000000	0.05779085
370621	127	0.3930396433	1.00000000	1.00000000	0.08337329
370621	128	0.0003583832	1.00000000	1.00000000	0.07532675
370621	133	0.0000068529	1.00000000	1.00000000	0.09776310
370621	134	0.0000060514	1.00000000	1.00000000	0.07178228
370621	135	0.0118585454	1.00000000	1.00000000	0.06459092
370621	136	0.0001672449	1.00000000	1.00000000	0.05977911
370621	137	0.0063210120	1.00000000	1.00000000	0.07773831
370621	138	0.0000738669	1.00000000	1.00000000	0.07600501
370621	144	0.0000050854	1.00000000	1.00000000	0.10988000
370621	145	0.0006099769	1.00000000	1.00000000	0.05679637
370621	146	0.0230198632	1.00000000	1.00000000	0.06402567
370621	147	0.0002805066	1.00000000	1.00000000	0.07646096
370621	148	0.0091676826	1.00000000	1.00000000	0.07848717
370621	157	0.6745140438	1.00000000	1.00000000	0.07398616
370621	158	0.0005268754	1.00000000	1.00000000	0.06482055
370621	167	0.0005263009	1.00000000	1.00000000	0.06458416
370621	168	0.0159949974	1.00000000	1.00000000	0.06360196
394317	157	0.6745140438	0.110994804	9.9998E-02	0.07398616
394318	127	0.3930396433	0.107603552	1.6870E-01	0.08337329
394319	125	0.6791453722	0.107603552	1.6924E-01	0.06375124
394320	112	0.6656504736	0.107603552	1.5353E-01	0.07047924

Table A.5: The cross-sections, branching fraction, and filter efficiency for the NUHM2 signal samples $m_{1/2} = 600$ GeV.

DSID	Final state	Cross-section [pb]	K-factor/BF	Filter efficiency	Relative uncertainty
370622	111	0.0007869897	1.00000000	1.00000000	0.07181679
370622	112	0.6643270342	1.00000000	1.00000000	0.07021531
370622	113	0.0000996207	1.00000000	1.00000000	0.06721434
370622	114	0.0000204490	1.00000000	1.00000000	0.07299332
370622	115	0.8407296201	1.00000000	1.00000000	0.06552209
370622	116	0.0002658841	1.00000000	1.00000000	0.06040295
370622	117	0.4923724748	1.00000000	1.00000000	0.08491961
370622	118	0.0001190742	1.00000000	1.00000000	0.08405305
370622	122	0.0001324452	1.00000000	1.00000000	0.07307817
370622	123	0.0033217150	1.00000000	1.00000000	0.06361965
370622	124	0.0002184464	1.00000000	1.00000000	0.06456221
370622	125	0.6766070496	1.00000000	1.00000000	0.06427279
370622	126	0.0003241413	1.00000000	1.00000000	0.05818056
370622	127	0.3913281838	1.00000000	1.00000000	0.08575382
370622	128	0.0001431279	1.00000000	1.00000000	0.07221632
370622	133	0.0000034045	1.00000000	1.00000000	0.08794933
370622	134	0.0000026928	1.00000000	1.00000000	0.07609993
370622	135	0.0048337927	1.00000000	1.00000000	0.05703733
370622	136	0.0000502367	1.00000000	1.00000000	0.06355969
370622	137	0.0025078220	1.00000000	1.00000000	0.07562175
370622	138	0.0000209783	1.00000000	1.00000000	0.07847390
370622	144	0.0000052666	1.00000000	1.00000000	0.07856700
370622	145	0.0002494848	1.00000000	1.00000000	0.06059516
370622	146	0.0118318988	1.00000000	1.00000000	0.07046938
370622	147	0.0001094560	1.00000000	1.00000000	0.07805891
370622	148	0.0044453542	1.00000000	1.00000000	0.08306247
370622	157	0.6438838471	1.00000000	1.00000000	0.07295880
370622	158	0.0002140543	1.00000000	1.00000000	0.06775447
370622	167	0.0002138494	1.00000000	1.00000000	0.06731630
370622	168	0.0079546496	1.00000000	1.00000000	0.06899943
394321	157	0.6438838471	0.110976399	9.3533E-02	0.07295880
394322	127	0.3913281838	0.109700775	1.5801E-01	0.08575382
394323	125	0.6766070496	0.109700775	1.5871E-01	0.06427279
394324	112	0.6643270342	0.109700775	1.3786E-01	0.07021531

Table A.6: The cross-sections, branching fraction, and filter efficiency for the NUHM2 signal samples $m_{1/2} = 700$ GeV.

DSID	Final state	Cross-section [pb]	K-factor/BF	Filter efficiency	Relative uncertainty
370623	111	0.0005212386	1.00000000	1.00000000	0.07063351
370623	112	0.6598118363	1.00000000	1.00000000	0.06943069
370623	113	0.0000669873	1.00000000	1.00000000	0.06712724
370623	114	0.0000113016	1.00000000	1.00000000	0.07064093
370623	115	0.8098002978	1.00000000	1.00000000	0.06493814
370623	116	0.0001234140	1.00000000	1.00000000	0.06889051
370623	117	0.4737135796	1.00000000	1.00000000	0.08608973
370623	118	0.0000526249	1.00000000	1.00000000	0.07771427
370623	122	0.0001087675	1.00000000	1.00000000	0.07088280
370623	123	0.0015416626	1.00000000	1.00000000	0.06537577
370623	124	0.0000974637	1.00000000	1.00000000	0.06530325
370623	125	0.6748686972	1.00000000	1.00000000	0.06282954
370623	126	0.0001487367	1.00000000	1.00000000	0.06359830
370623	127	0.3906074836	1.00000000	1.00000000	0.08243869
370623	128	0.0000632347	1.00000000	1.00000000	0.07613879
370623	133	0.0000021556	1.00000000	1.00000000	0.08808178
370623	134	0.0000013753	1.00000000	1.00000000	0.08184458
370623	135	0.0022215540	1.00000000	1.00000000	0.05781810
370623	136	0.0000179127	1.00000000	1.00000000	0.06707128
370623	137	0.0011306653	1.00000000	1.00000000	0.07974272
370623	138	0.0000071002	1.00000000	1.00000000	0.07996818
370623	144	0.0000033200	1.00000000	1.00000000	0.08521909
370623	145	0.0001114849	1.00000000	1.00000000	0.06626951
370623	146	0.0064128038	1.00000000	1.00000000	0.07356448
370623	147	0.0000474513	1.00000000	1.00000000	0.07695978
370623	148	0.0023333882	1.00000000	1.00000000	0.08950999
370623	157	0.6240319555	1.00000000	1.00000000	0.07242344
370623	158	0.0000960852	1.00000000	1.00000000	0.06651898
370623	167	0.0000961123	1.00000000	1.00000000	0.06811969
370623	168	0.0042577101	1.00000000	1.00000000	0.07239458
394325	157	0.6240319555	0.1109638923	8.7153E-02	0.07242344
394326	127	0.3906074836	0.1116429166	1.3865E-01	0.08243869
394327	125	0.6748686972	0.1116429166	1.4629E-01	0.06282954
394328	112	0.6598118363	0.1116429166	1.2823E-01	0.06943069

Table A.7: The cross-sections, branching fraction, and filter efficiency for the NUHM2 signal samples $m_{1/2} = 800$ GeV.

ID	Particles										
111	$\chi_1^0 \chi_1^0$	-	-	-	-	-	-	-	-	-	-
112	$\chi_1^0 \chi_2^0$	122	$\chi_2^0 \chi_2^0$	-	-	-	-	-	-	-	-
113	$\chi_1^0 \chi_3^0$	123	$\chi_2^0 \chi_3^0$	133	$\chi_3^0 \chi_3^0$	-	-	-	-	-	-
114	$\chi_1^0 \chi_4^0$	124	$\chi_2^0 \chi_4^0$	134	$\chi_3^0 \chi_4^0$	144	$\chi_4^0 \chi_4^0$	-	-	-	-
115	$\chi_1^0 \chi_1^+$	125	$\chi_2^0 \chi_1^+$	135	$\chi_3^0 \chi_1^+$	145	$\chi_4^0 \chi_1^+$	-	-	-	-
116	$\chi_1^0 \chi_2^+$	126	$\chi_2^0 \chi_2^+$	136	$\chi_3^0 \chi_2^+$	146	$\chi_4^0 \chi_2^+$	-	-	-	-
117	$\chi_1^0 \chi_1^-$	127	$\chi_2^0 \chi_1^-$	137	$\chi_3^0 \chi_1^-$	147	$\chi_4^0 \chi_1^-$	157	$\chi_1^+ \chi_1^-$	167	$\chi_2^+ \chi_1^-$
118	$\chi_1^0 \chi_2^-$	128	$\chi_2^0 \chi_2^-$	138	$\chi_3^0 \chi_2^-$	148	$\chi_4^0 \chi_2^-$	158	$\chi_1^+ \chi_2^-$	168	$\chi_2^+ \chi_2^-$

Table A.8: The list of various final states.

Appendix B

Electron isolation

The electron reconstruction, identification, and isolation play a crucial role for many ATLAS analysis. The electrons¹ leave tracks in the ID and energy deposits in the ECAL. The reconstruction algorithm combines the signals in the calorimeter and the tracks in the ID to defined the electron candidates. The reconstructed candidates are identified as electrons based on a likelihood discrimination which distinguishes the electron candidates from the hadrons, non-prompt electrons originating from photon conversions, and heavy flavour hadron decays. Additionally, the electron candidates are required to be isolated to further distinguish the signal and the background objects. The electron efficiency measurements are performed based on the tag-and-probe method using the $Z \rightarrow ee$ and $J/\psi \rightarrow ee$ samples.

B.1 Electron reconstruction

The electrons are reconstructed in the central region of the ATLAS detector ($|\eta| < 2.47$).

¹The electrons and positron are referred to as electrons.

B.2 Electron identification

B.3 Electron isolation

Appendix C

The distributions

The kinematic variable distributions for the NUHM2 model with $m_{1/2}$ from 350 GeV to 800 GeV in $1 < \text{SR}\ell\ell-m_{\ell\ell} < 60$ GeV are shown in this section.

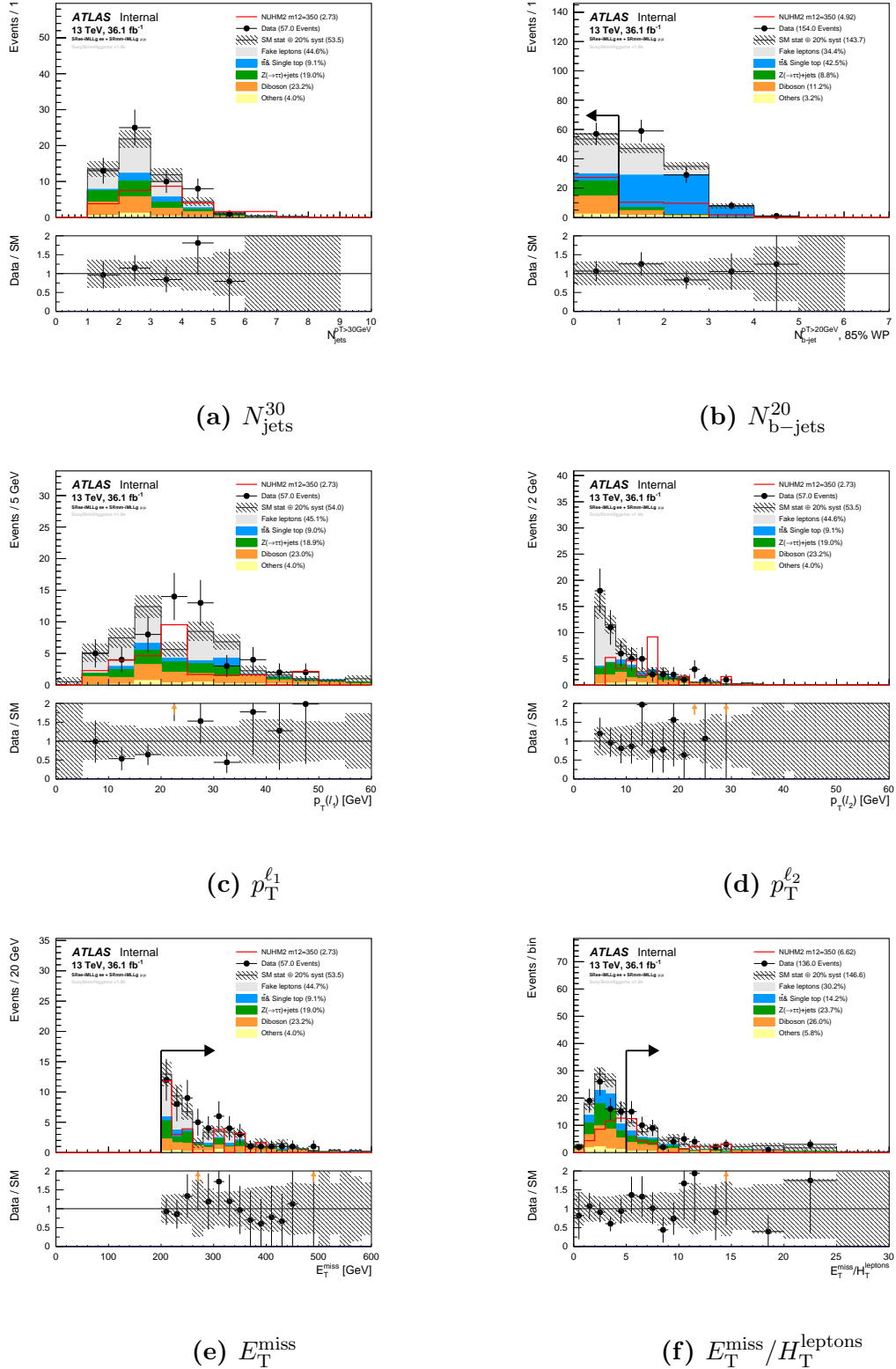


Figure C.1: The ‘ $N - 1$ ’ distributions for NUHM2 model with $m_{1/2} = 350$ GeV in SR region

$1 < \text{SR}\ell\ell-m_{\ell\ell} < 60$ GeV. The NUHM2 distributions are multiplied by 10 but the number of events in the legend use its actual values.

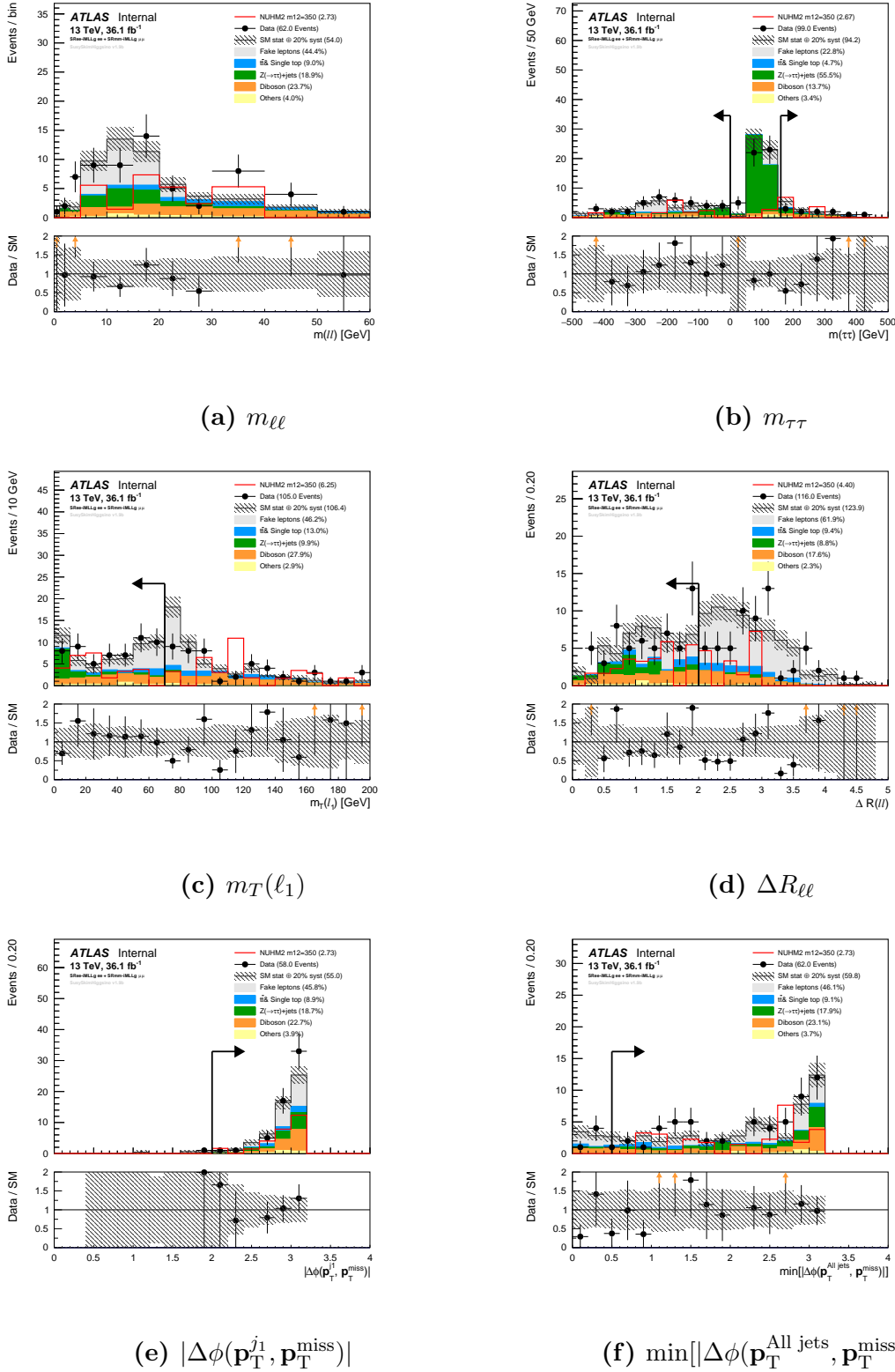


Figure C.2: The ‘ $N - 1$ ’ distributions for NUHM2 model with $m_{1/2} = 350$ GeV in SR region

$1 < \text{SR}\ell\ell - m_{\ell\ell} < 60$ GeV. The NUHM2 distributions are multiplied by 10 but the number of events in the legend use its actual values.

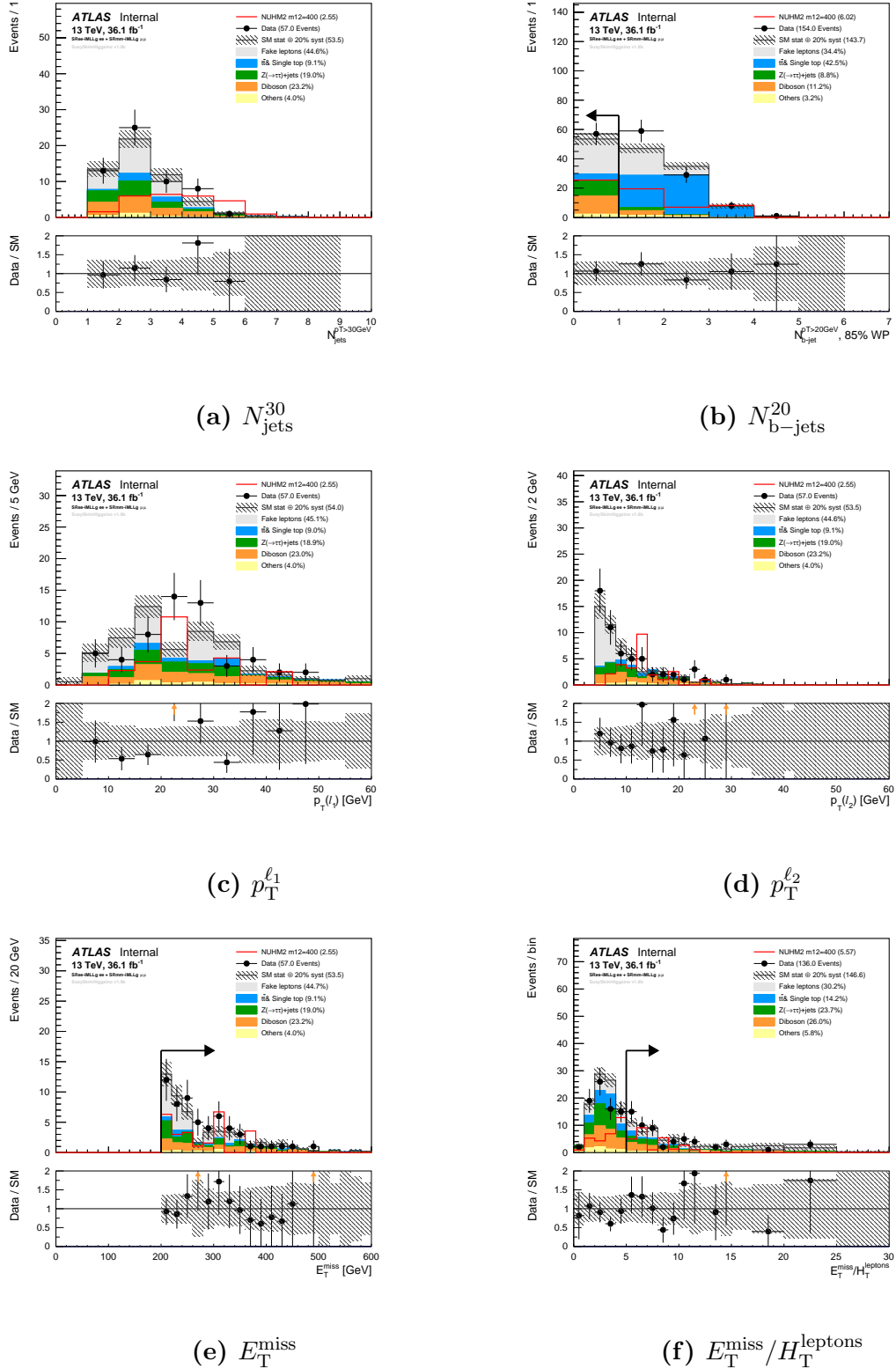


Figure C.3: The ‘ $N - 1$ ’ distributions for NUHM2 model with $m_{1/2} = 400$ GeV in SR region

$1 < \text{SR}\ell\ell-m_{\ell\ell} < 60$ GeV. The NUHM2 distributions are multiplied by 10 but the number of events in the legend use its actual values.

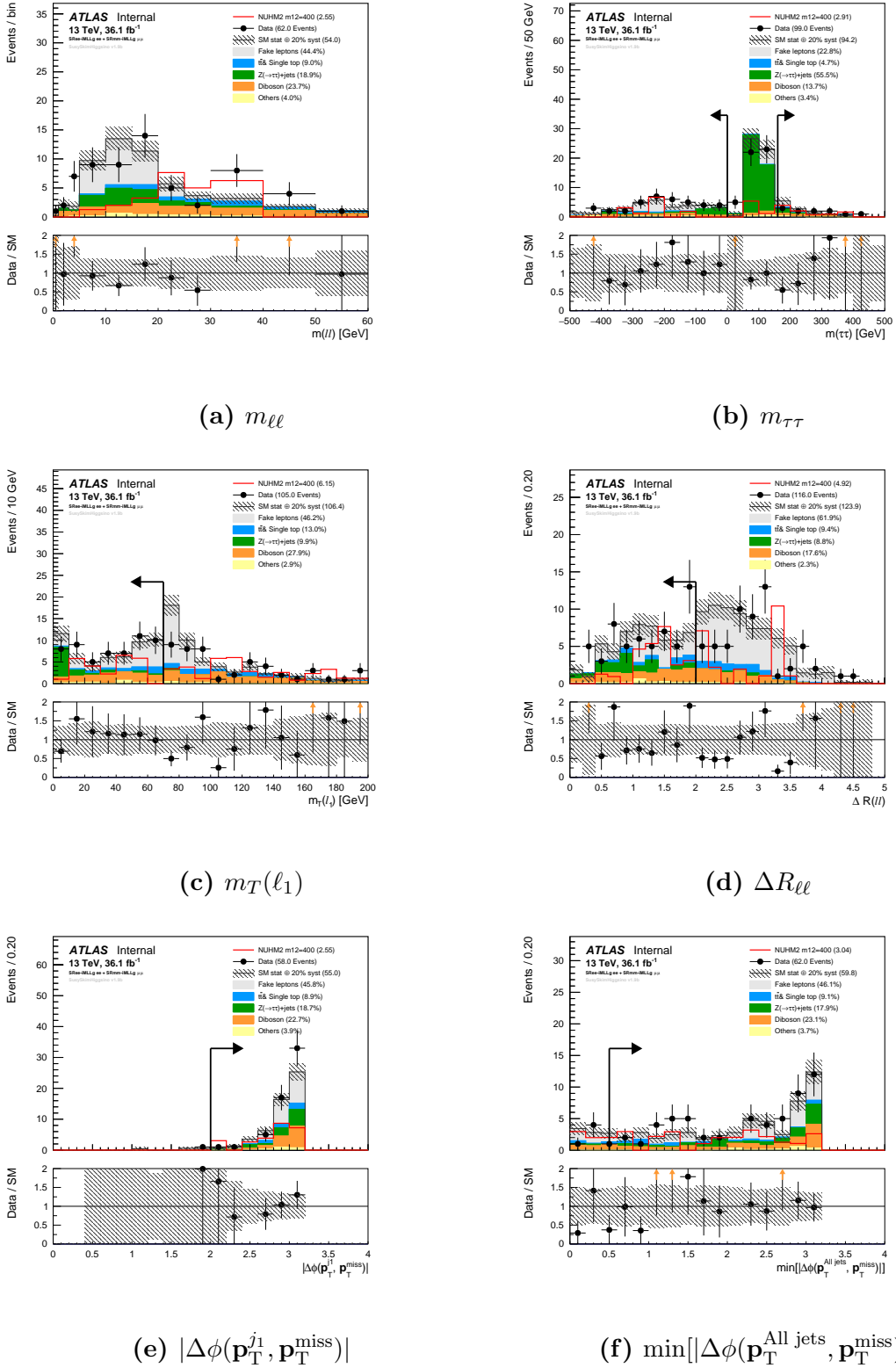


Figure C.4: The ‘ $N - 1$ ’ distributions for NUHM2 model with $m_{1/2} = 400$ GeV in SR region

$1 < \text{SR}\ell\ell - m_{\ell\ell} < 60$ GeV. The NUHM2 distributions are multiplied by 10 but the number of events in the legend use its actual values.

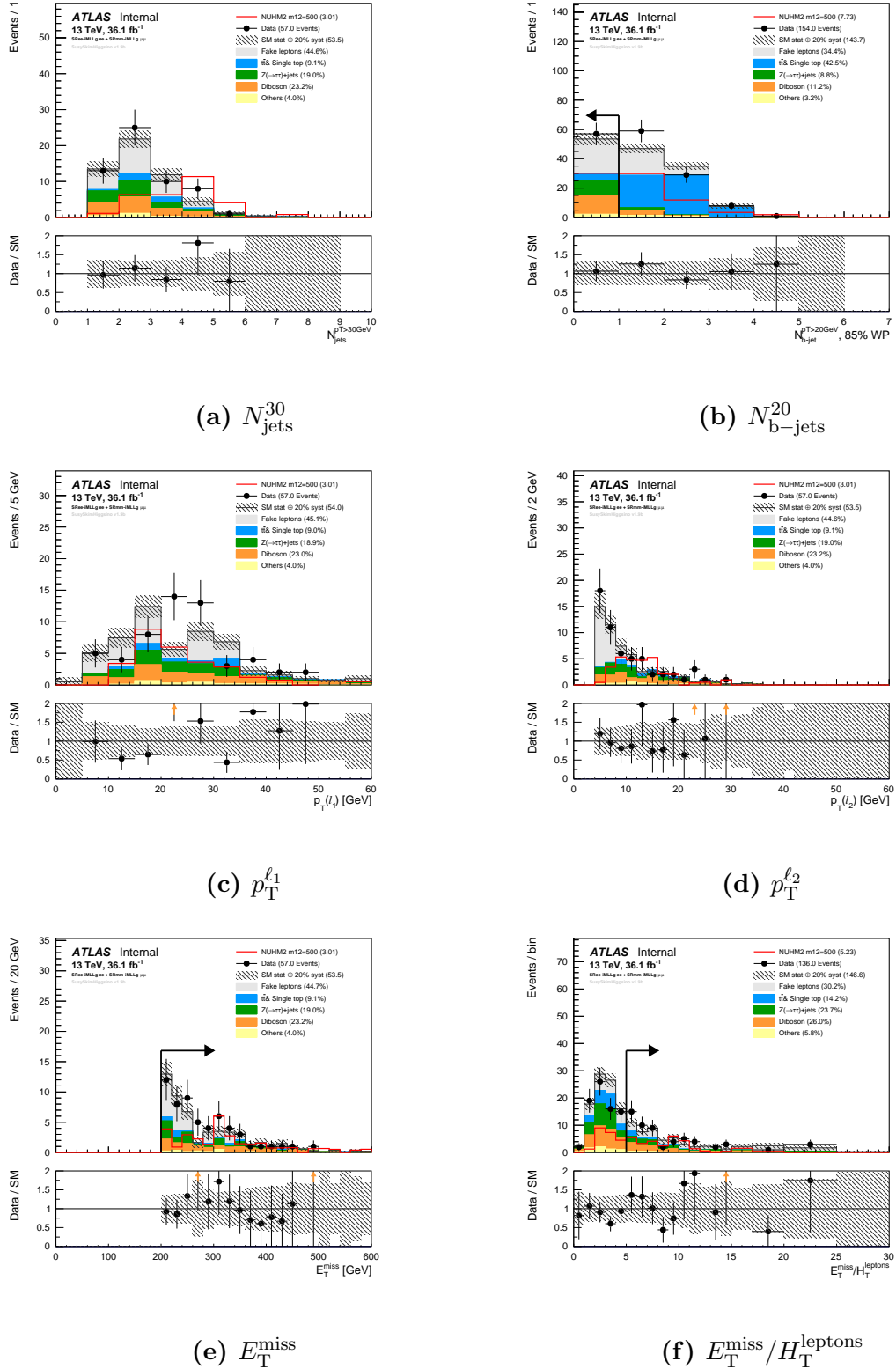


Figure C.5: The ‘ $N - 1$ ’ distributions for NUHM2 model with $m_{1/2} = 500$ GeV in SR region

$1 < \text{SR} \ell\ell - m_{\ell\ell} < 60$ GeV. The NUHM2 distributions are multiplied by 10 but the number of events in the legend use its actual values.

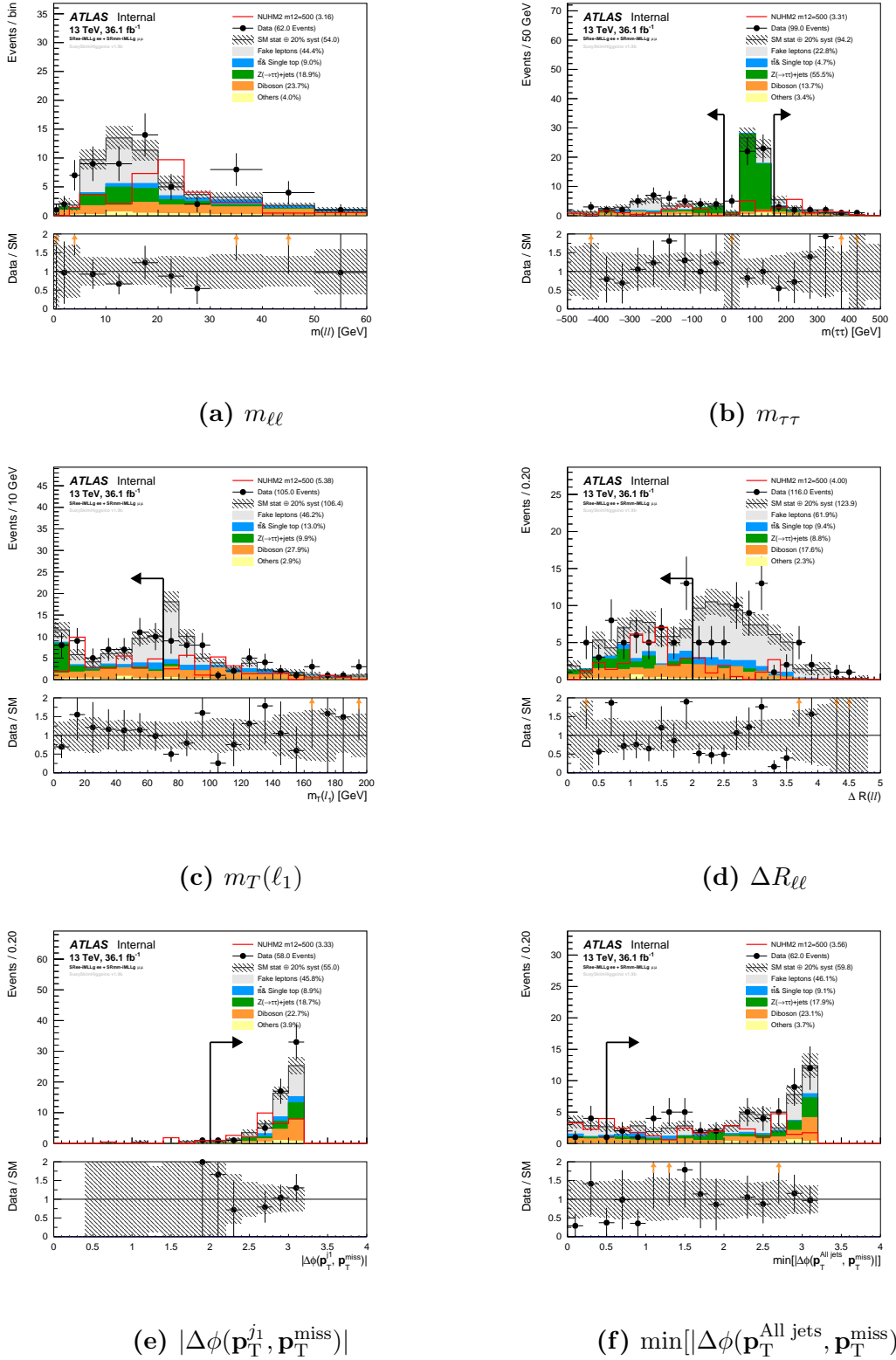


Figure C.6: The ‘ $N - 1$ ’ distributions for NUHM2 model with $m_{1/2} = 500$ GeV in SR region

$1 < \text{SR}\ell\ell - m_{\ell\ell} < 60$ GeV. The NUHM2 distributions are multiplied by 10 but the number of events in the legend use its actual values.

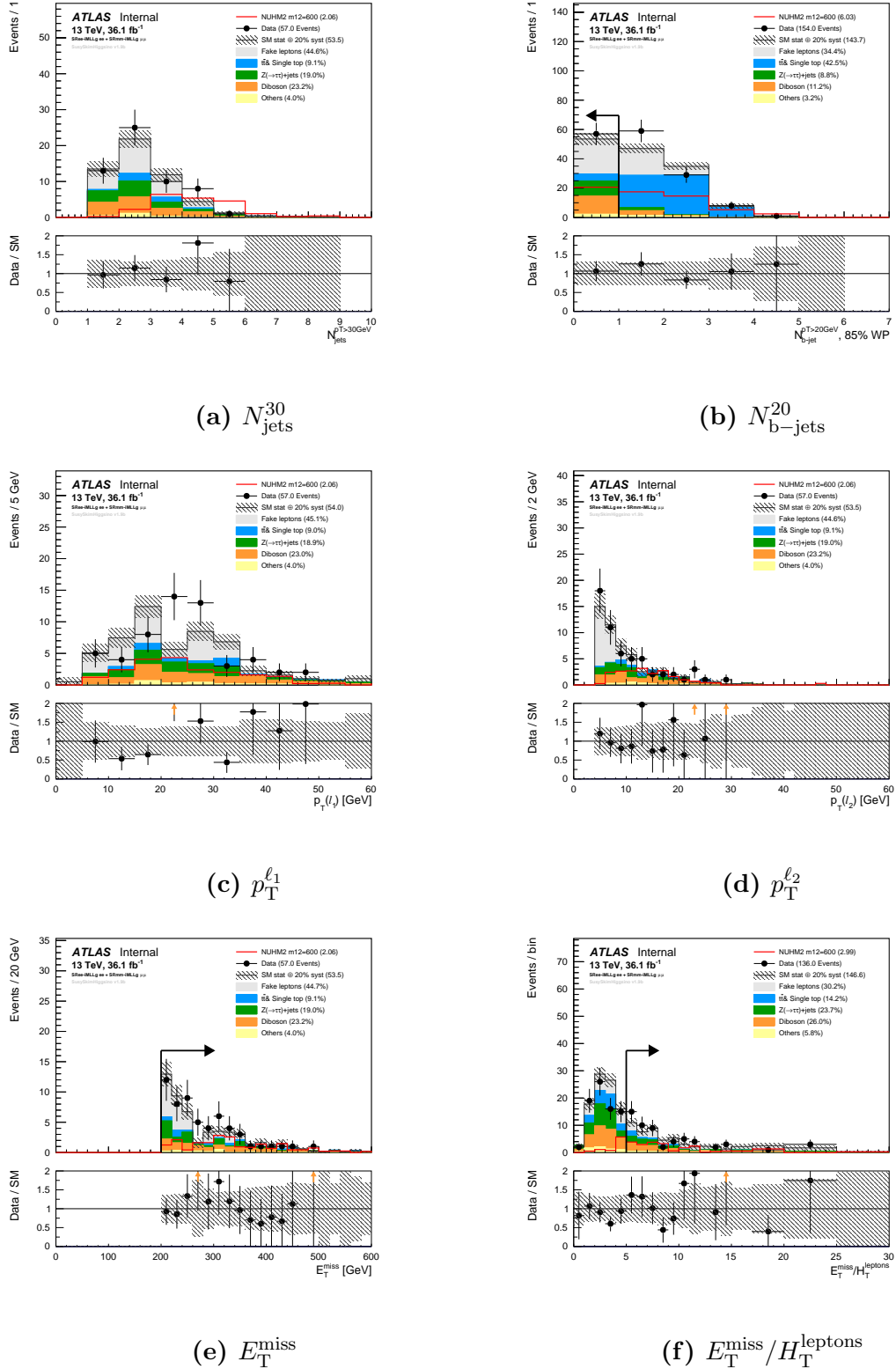


Figure C.7: The ‘ $N - 1$ ’ distributions for NUHM2 model with $m_{1/2} = 600$ GeV in SR region

$1 < \text{SR}\ell\ell-m_{\ell\ell} < 60$ GeV. The NUHM2 distributions are multiplied by 10 but the number of events in the legend use its actual values.

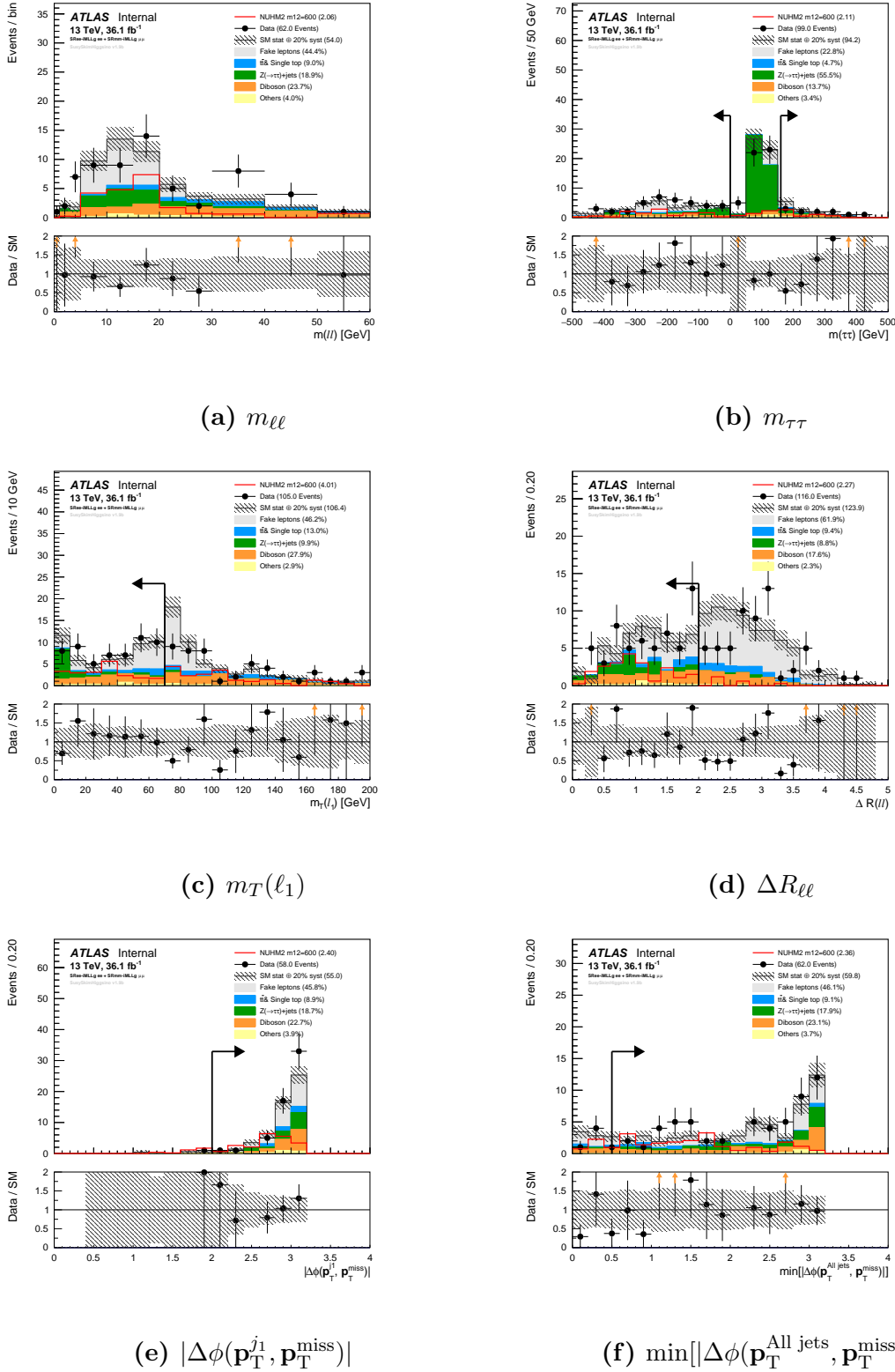


Figure C.8: The ‘ $N - 1$ ’ distributions for NUHM2 model with $m_{1/2} = 600$ GeV in SR region

$1 < \text{SR}\ell\ell - m_{\ell\ell} < 60$ GeV. The NUHM2 distributions are multiplied by 10 but the number of events in the legend use its actual values.

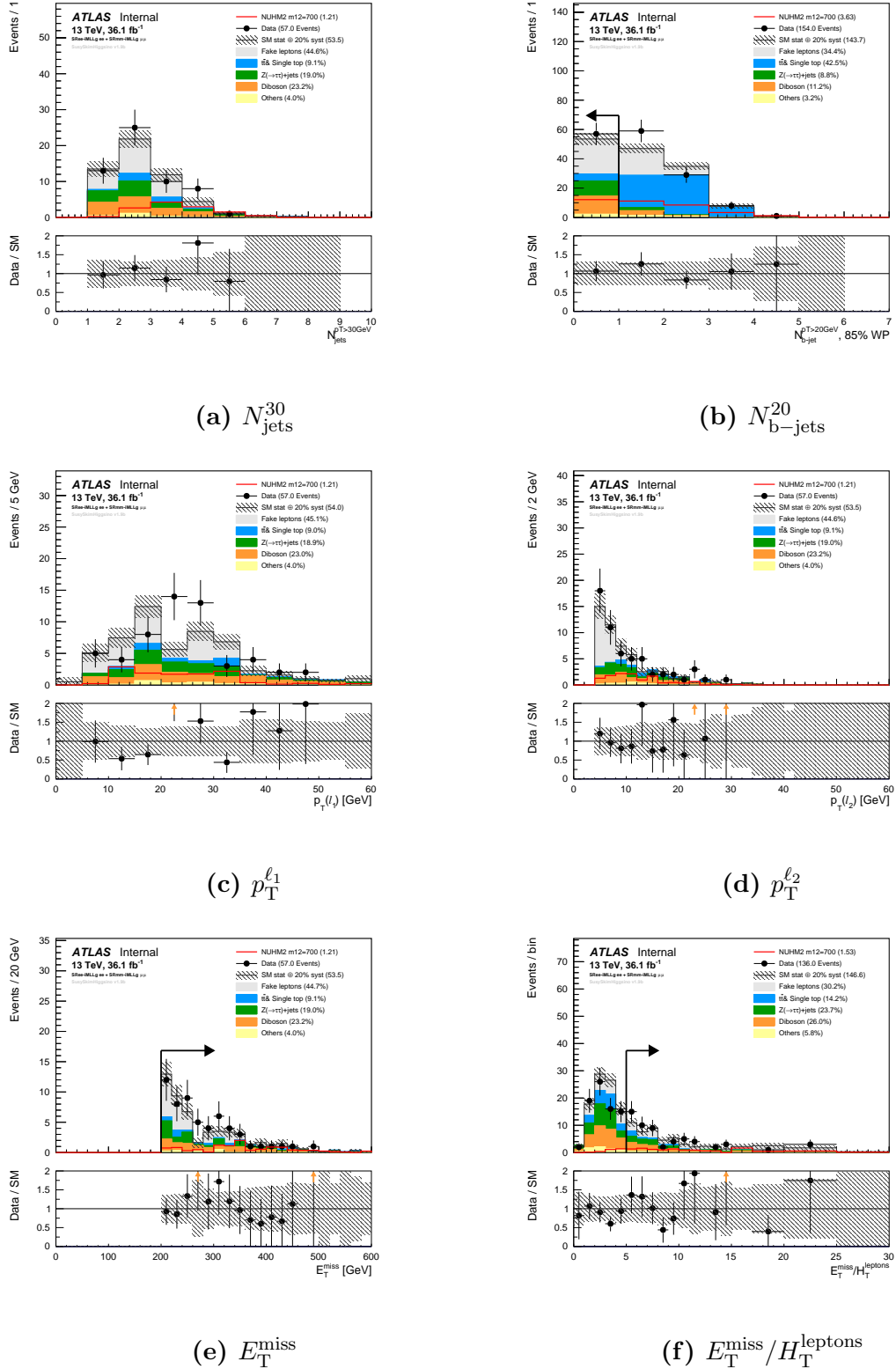


Figure C.9: The ‘ $N - 1$ ’ distributions for NUHM2 model with $m_{1/2} = 700$ GeV in SR region

$1 < \text{SR}\ell\ell-m_{\ell\ell} < 60$ GeV. The NUHM2 distributions are multiplied by 10 but the number of events in the legend use its actual values.

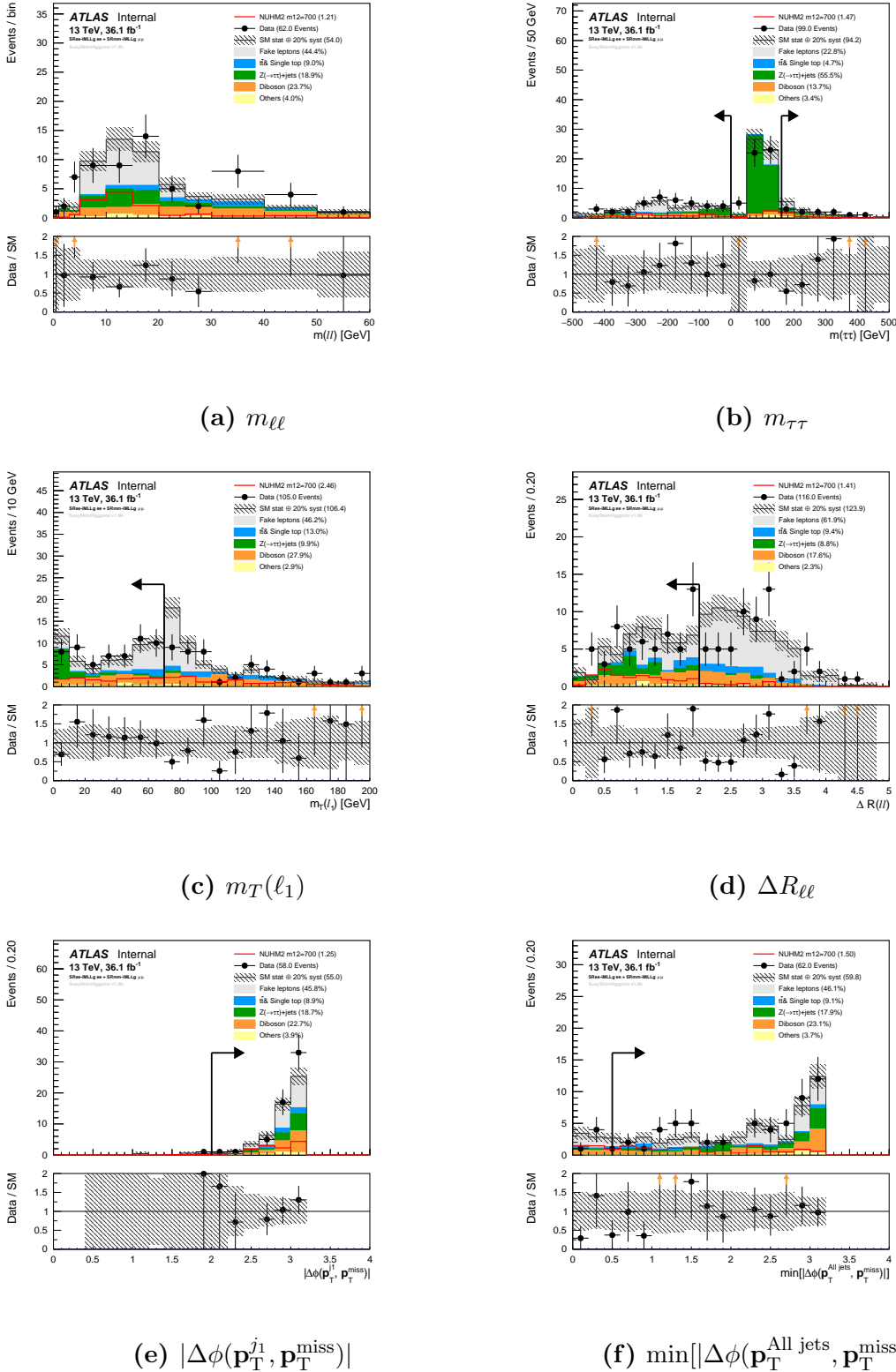


Figure C.10: The ‘ $N - 1$ ’ distributions for NUHM2 model with $m_{1/2} = 700$ GeV in SR region 1 $<\text{SR}\ell\ell-m_{\ell\ell}<60$ GeV. The NUHM2 distributions are multiplied by 10 but the number of events in the legend use its actual values.

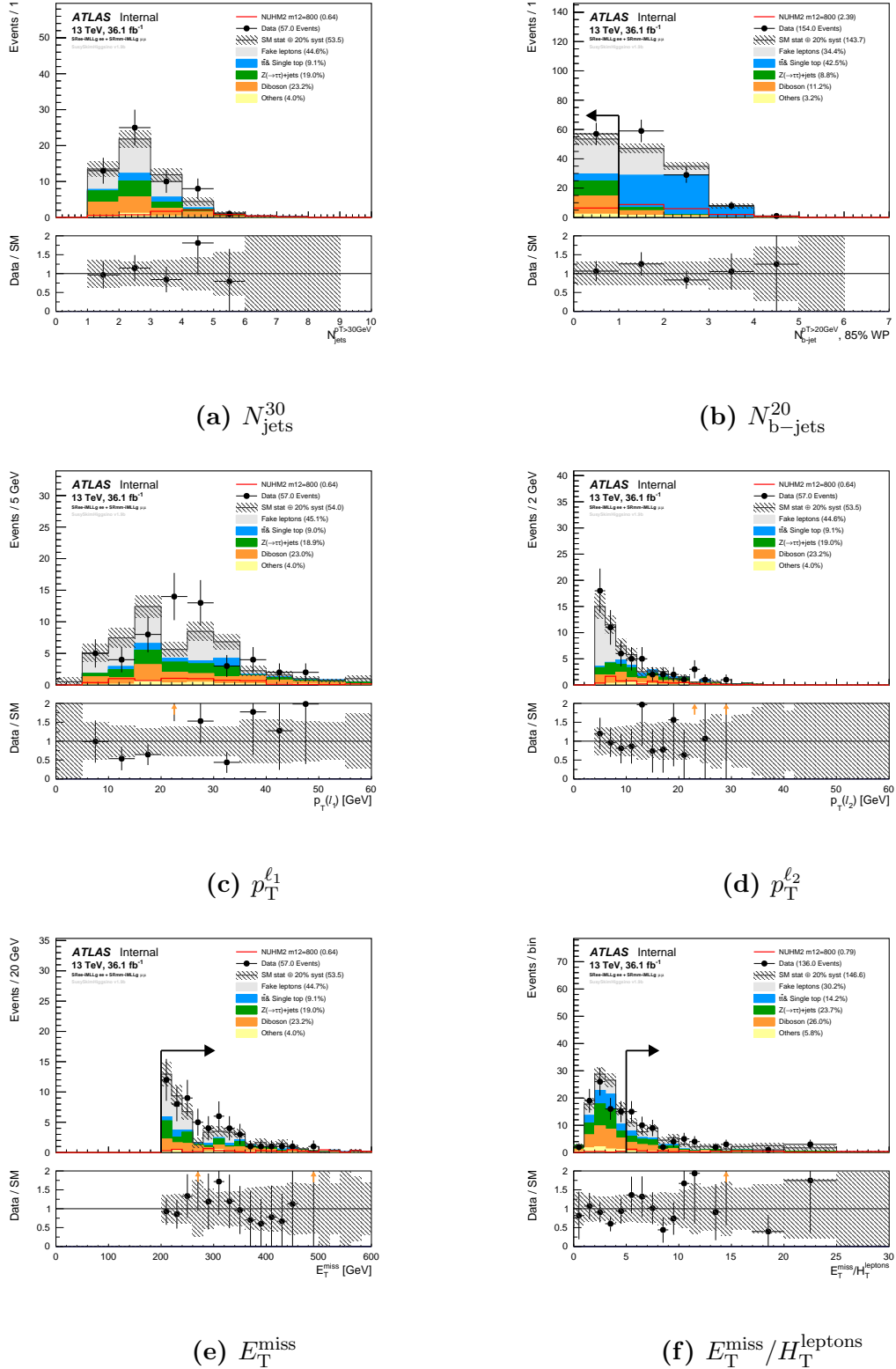


Figure C.11: The ‘ $N - 1$ ’ distributions for NUHM2 model with $m_{1/2} = 800$ GeV in SR region 1 $<\text{SR}\ell\ell-m_{\ell\ell}<60$ GeV. The NUHM2 distributions are multiplied by 10 but the number of events in the legend use its actual values.

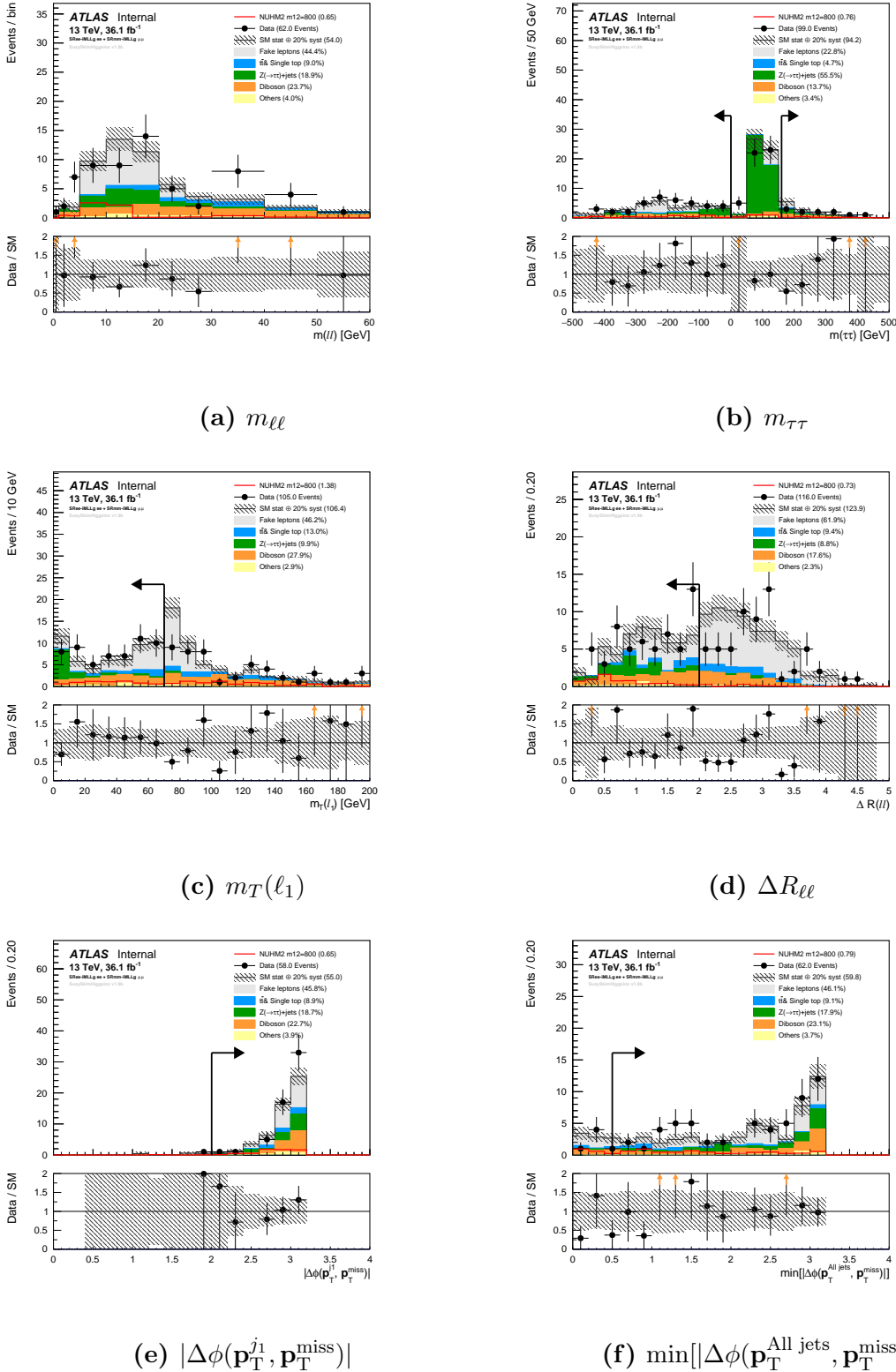


Figure C.12: The ‘ $N - 1$ ’ distributions for NUHM2 model with $m_{1/2} = 800$ GeV in SR region 1 $<\text{SR}\ell\ell-m_{\ell\ell}<60$ GeV. The NUHM2 distributions are multiplied by 10 but the number of events in the legend use its actual values.

Appendix D

Search for strongly-produced SUSY in final states with two same-sign or three leptons and jets using 36.1 fb^{-1} pp collision data at $\sqrt{s} = 13 \text{ TeV}$ with the ATLAS detector

The Monte Carlo (MC) samples are used to model the SUSY signals and to estimate the SM background. The MC samples are processed using a ATLAS detector full simulation (FullSim) or a fast simulation (AFII¹) based on GEANT4 [82] simulation package. The FullSim simulates the detailed properties of the ATLAS detector while the AFII uses a parameterized calorimeter response and simulates ID and MS [83] based on GEANT4. The simulated MC events are reweighted to the observed pile-up conditions in the data.

D.1 Samples used for strong interaction

Table D.1 shows the event generator, parton shower, cross-section normalization, PDF set [86], and the set of tuned parameters for modelling for all samples. Except those

¹AFII stands for ATLAS Fast II.

produced by the SHERPA, the EVTGEN v1.2.0 package [88] is used to model the properties of bottom and charm hadron decays for all MC samples.

Signal/Background	Physics process	Event generator	Parton shower	Cross-section normalization	PDF set	Set of tunned parameters
Signal	RPC	MG5_AMC@NLO 2.2.3	PYTHIA 8.186	NLO+NLL	NNPDF2.3LO	A14
	RPV (except Figure ??)	MG5_AMC@NLO 2.2.3	PYTHIA 8.210	or	NNPDF2.3LO	A14
	RPV (Figure ??)	Herwig++ 2.7.1	Herwig++ 2.7.1	NLO-Prospino2	CTEQ6L1	UEEE5
$t\bar{t} + X$ background	$t\bar{t}W, t\bar{t}Z/\gamma^*$	MG5_AMC@NLO 2.2.2	PYTHIA 8.186	NLO	NNPDF2.3LO	A14
	$t\bar{t}H$	MG5_AMC@NLO 2.3.2	PYTHIA 8.186	NLO	NNPDF2.3LO	A14
	$4t$	MG5_AMC@NLO 2.2.2	PYTHIA 8.186	NLO	NNPDF2.3LO	A14
Diboson background	ZZ, WZ	SHERPA 2.2.1	SHERPA 2.2.1	NLO	NNPDF2.3LO	SHERPA default
	Other (inc. $W^\pm W^\pm$)	SHERPA 2.1.1	SHERPA 2.1.1	NLO	CT10	SHERPA default
Rare background	$t\bar{t}WW, t\bar{t}WZ$	MG5_AMC@NLO 2.2.2	PYTHIA 8.186	NLO	NNPDF2.3LO	A14
	$tZ, tWZ, tt\bar{t}$	MG5_AMC@NLO 2.2.2	PYTHIA 8.186	LO	NNPDF2.3LO	A14
	WH, ZH	MG5_AMC@NLO 2.2.2	PYTHIA 8.186	NLO	NNPDF2.3LO	A14
Triboson	SHERPA 2.1.1	SHERPA 2.1.1	NLO	CT10	SHERPA default	

Table D.1: The simulated signal and background MC samples. The event generator, parton shower, cross-section normalization, PDF set, and the set of tunned parameters for each samples are shown. The $t\bar{t}WW, t\bar{t}WZ, tZ, tWZ, tt\bar{t}, WH, ZH$ and triboson background samples are labeled in the "rare" because they contribute a very small amount to the signal region.

Signal region	$N_{\text{leptons}}^{\text{signal}}$	$N_{b-\text{jets}}$	N_{jets}	$p_T^{\text{jet}} \text{ [GeV]}$	$E_T^{\text{miss}} \text{ [GeV]}$	m_{eff}	$E_T^{\text{miss}}/m_{\text{eff}}$	Other	Targeted signal
Rpc2L2bS	$\geq 2\text{SS}$	≥ 2	≥ 6	> 25	> 200	> 600	> 0.25	-	Fig. ??
Rpc2L2bH	$\geq 2\text{SS}$	≥ 2	≥ 6	> 25	-	> 1800	> 0.15	-	Fig. ??, NUHM2
Rpc2Lsoft1b	$\geq 2\text{SS}$	≥ 1	≥ 6	> 25	> 100	-	> 0.3	$20, 10 < p_T^{\ell_1}, p_T^{\ell_2} < 100 \text{ GeV}$	Fig. ??
Rpc2Lsoft2b	$\geq 2\text{SS}$	≥ 2	≥ 6	> 25	> 200	> 600	> 0.25	$20, 10 < p_T^{\ell_1}, p_T^{\ell_2} < 100 \text{ GeV}$	Fig. ??
Rpc2L0bS	$\geq 2\text{SS}$	$= 0$	≥ 6	> 25	> 150	-	> 0.25	-	Fig. ??
Rpc2L0bH	$\geq 2\text{SS}$	$= 0$	≥ 6	> 40	> 250	> 900	-	-	Fig. ??
Rpc3L0bS	≥ 3	$= 0$	≥ 4	> 40	> 200	> 600	-	-	Fig. ??
Rpc3L0bH	≥ 3	$= 0$	≥ 4	> 40	> 200	> 1600	-	-	Fig. ??
Rpc3L1bS	≥ 3	≥ 1	≥ 4	> 40	> 200	> 600	-	-	Other
Rpc3L1bH	≥ 3	≥ 1	≥ 4	> 40	> 200	> 1600	-	-	Other
Rpc2L1bS	$\geq 2\text{SS}$	≥ 1	≥ 6	> 25	> 150	> 600	> 0.25	-	Fig. ??
Rpc2L1bH	$\geq 2\text{SS}$	≥ 1	≥ 6	> 25	> 250	-	> 0.2	-	Fig. ??
Rpc3LSS1b	$\geq \ell^\pm \ell^\pm \ell^\pm$	≥ 1	-	-	-	-	-	veto $81 < m_{e^\pm e^\pm} < 101 \text{ GeV}$	Fig. ??
Rpv2L1bH	$\geq 2\text{SS}$	≥ 1	≥ 6	> 50	-	> 2200	-	-	Fig. ??, ??
Rpv2L0b	$= 2\text{SS}$	$= 0$	≥ 6	> 40	-	> 1800	-	veto $81 < m_{e^\pm e^\pm} < 101 \text{ GeV}$	Fig. ??
Rpv2L2bH	$\geq 2\text{SS}$	≥ 2	≥ 6	> 40	-	> 2000	-	veto $81 < m_{e^\pm e^\pm} < 101 \text{ GeV}$	Fig. ??
Rpv2L2bS	$\geq \ell^- \ell^-$	≥ 2	≥ 3	> 50	-	> 1200	-	-	Fig. ??
Rpv2L1bS	$\geq \ell^- \ell^-$	≥ 1	≥ 4	> 50	-	> 1200	-	-	Fig. ??
Rpv2L1bM	$\geq \ell^- \ell^-$	≥ 2	≥ 4	> 50	-	> 1800	-	-	Fig. ??

Table D.2

Appendix E

Real lepton efficiency

This appendix presents more details on the measurement of the data-driven real lepton efficiency using the Z tag-and-probe method.

E.1 The Z tag-and-probe method

The Z tag-and-probe method is used to extract the leptons from data and measure the real lepton efficiency. The selected events are required to have at least two baseline leptons. The lepton candidates with $p_T > 25$ GeV and satisfying all the signal lepton requirements are categorized into *tag leptons*. The lepton candidates passing baseline lepton requirements can be classified as *probe leptons*. In order to form a tag-and-probe pair, the two selected leptons have to carry the same flavor and opposite charge. The invariant mass of the tag-and-probe pair system should satisfy the Z boson mass window $80 < m_{\ell\ell} < 100$ GeV. All possible combinations of the tag-and-probe pairs are considered to avoid any bias and to increase the statistics. For the $Z \rightarrow ee$ decay, an additional $|\eta| < 2$ requirement is applied on the tag and probe leptons. However, no additional requirement is applied for the $Z \rightarrow \mu\mu$ decay. The tag lepton is used to select the probe lepton only and the probe lepton is used for the real efficiency measurements. In this study,

the tag and probe leptons are required to match the lepton triggers listed in Table E.1.

Trigger	lepton	2015	2016
Single lepton trigger	electron	<code>e24_lhmedium_iloose_L1EM20VH</code>	<code>e26_lhtight_nod0_ivarloose</code>
	muon	<code>mu20_iloose_L1MU15</code>	<code>mu26_ivarmedium</code>
Dilepton trigger	electron	<code>2e12_lhloose_L12EM10VH</code>	<code>2e17_lhvloose_nod0</code>
	muon	<code>mu18_mu8noL1</code>	<code>mu22_mu8noL1</code>

Table E.1: The list of single lepton and dilepton triggers used for the real lepton efficiency measurements. The dilepton triggers are used for studying the systematic uncertainties causing by the trigger.

Figure E.1 shows the data-to-MC comparison of the tag-and-probe pair invariant mass distributions which indicate the need of subtracting the background especially for the probe electron with $p_T < 20$ GeV. A background template method, which is similar to the one used by the e/γ performance group for their efficiency measurements [105], is used to estimate the background contamination from the low p_T electrons. No background subtraction is performed on the signal leptons because the background contamination is found to be negligible. However, the background contamination in the baseline probe leptons needs to be subtracted. The real lepton efficiency is obtained by the following equation

$$\epsilon = \frac{N_{\text{signal}}}{N_{\text{baseline}} - N_{\text{baseline}}^{\text{bkg}}} \quad (\text{E.1})$$

where N_{signal} is the number of probe leptons passing the signal requirements, N_{baseline} is the number of probe leptons passing the baseline requirements, and $N_{\text{baseline}}^{\text{bkg}}$ is the estimated background contamination in the baseline probe leptons.

E.2 Background subtraction

The background template method is used to evaluate the background contamination on data. By inverting the calorimeter and track isolations, requesting the electron object to fail the medium LH identification, the background sample enriched template can be obtained. Three background templates are considered for the systematic study. The definitions of the background template are summarized in Table E.2.

cut	variation 1 template	baseline template	variation 2 template
Identification	-	fail medium LH	fail medium LH
Calorimeter isolation	$E_T^{topocone20}/p_T > 6\%$	$E_T^{topocone20}/p_T > 15\%$	$E_T^{topocone20}/p_T > 20\%$
Track isolation	$p_T^{varcone20}/p_T > 6\%$	$E_T^{topocone20}/p_T > 8\%$	$E_T^{topocone20}/p_T > 15\%$

Table E.2: The definition of the background templates for estimating the background contamination associated with the Z tag-and-probe method. The baseline template is used to estimate the background contamination. The variation 1 template has looser requirements and the variation 2 template has tighter requirements. They are used to assess the systematic caused by the background contamination.

Figure E.2 shows the m_{ee} distributions of the background template. The invariant mass distribution of the template events (m_{ee}^{template}) is then used to estimate the amount of background in $80 < m_{\ell\ell} < 100$ GeV region. In order to estimate the correct of background events, the $120 < m_{ee} < 150$ GeV region is used to normalize the background template because a smaller prompt electron contribution is expected in this region. Equation E.2 shows the estimation of the number of background events in the tail region using the baseline electrons.

$$N_{bkg}^{\text{tail}} = N_{\text{baseline}}^{\text{tail}} - N_{\text{MC,prompt}}^{\text{tail}} \quad (\text{E.2})$$

where $N_{\text{baseline}}^{\text{tail}}$ can be obtained by integrating the baseline m_{ee} distribution in the tail region and $N_{\text{MC,prompt}}^{\text{tail}}$ is the prompt electron contamination which is estimated by integrating the m_{ee} distribution in the tail region using the $Z \rightarrow ee$ MC simulation. Because the baseline electron selection criteria already provides a relatively high purity of prompt electrons, the background template suffers from low statistics in the tail region. The template is fitted in region $60 < m_{ee}^{\text{template}} < 120$ GeV using an exponential function to avoid any bias in the normalization factor due to statistical fluctuations. However, the $80 < m_{ee}^{\text{template}} < 100$ GeV is excluded to minimize the prompt lepton contamination arising from $Z \rightarrow ee$ decays. The fit is mostly driven by the $60 < m_{ee}^{\text{template}} < 80$ GeV due to the low statistics in the tail. After fitting is performed, the template in the tail region $N_{\text{template}}^{\text{tail}}$ is normalized to the background in the tail N_{bkg}^{tail} to get the correct estimated number of background events. The baseline m_{ee} distributions before and after applying the background subtraction using the background template are shown in Fig. E.3. The data after performing the background subtraction, the MC simulation samples, the background template distributions, and the fitting results are also shown. The simulated m_{ee} distribution of $Z \rightarrow ee$ MC are normalized to the data, which background subtraction has been performed, using a Gaussian fit in Z peak region $85 < m_{ee} < 95$ GeV. After performing the background subtraction, the data and MC have good agreement within the statistical uncertainties.

Then, the background contamination in the Z mass region $80 < m_{ee} < 100$ GeV is calculated using

$$N_{bkg}^{80 < m_{ee} < 100 \text{ GeV}} = \int_{80}^{100} N_{\text{template}} dm_{ee} \cdot \frac{N_{bkg}^{\text{tail}}}{N_{\text{template}}^{\text{tail}}} \quad (\text{E.3})$$

Table E.3 summarize the background estimations in different p_T and $|\eta|$ regions.

The largest improvements are observed in the lowest p_T bin ($10 < p_T < 15$ GeV) where

	$0 < \eta < 0.8$	$0.8 < \eta < 1.37$	$1.52 < \eta < 2.0$
$10 < p_T < 15 \text{ GeV}$	4.04%	2.10%	3.17%
$15 < p_T < 20 \text{ GeV}$	0.44%	0.58%	0.76%

Table E.3: The estimated background contamination in different p_T and $|\eta|$ regions. The p_T and $|\eta|$ binnings correspond to the one used for the final measurements.

a sizeable background contamination is subtracted. The background contamination is relatively small in the second lowest p_T bin ($15 < p_T < 20 \text{ GeV}$) providing the evidence that high purity of prompt leptons can be obtained using Z tag-and-probe method. Table E.4 shows the real electron efficiencies before and after performing the background subtraction.

	background subtraction	$0 < \eta < 0.8$	$0.8 < \eta < 1.37$	$1.52 < \eta < 2.0$
$10 < p_T < 15 \text{ GeV}$	before	57.4 ± 0.9	66.6 ± 0.8	53.2 ± 0.9
	after	59.9 ± 1.9	68.0 ± 1.8	55.0 ± 1.7
$15 < p_T < 20 \text{ GeV}$	before	64.5 ± 0.2	69.4 ± 0.2	62.0 ± 0.3
	after	64.8 ± 0.5	69.8 ± 0.5	62.5 ± 0.6

Table E.4: The real electron efficiencies before and after performing the background subtraction in different p_T and $|\eta|$ regions are shown in percentage.

E.3 Cut efficiencies

Figure E.4 shows the efficiencies associated to each signal cut with respect to baseline definitions. The prompt electron efficiency increases with p_T from $\sim 62\%$ to $\sim 98\%$ and the efficiency losses are dominated by the calorimeter isolation. The calorimeter isolation

cut efficiency increases with p_T from $\sim 69\%$ to $\sim 98\%$. The loose to medium likelihood (LH) cut efficiency increases from $\sim 92\%$ to $\sim 96\%$ in the $10 < p_T < 30$ GeV then reaches a plateau when $30 < p_T < 50$ GeV and increases again to $\sim 98\%$ when $p_T > 60$ GeV. The track isolation cut efficiency increases from $\sim 89\%$ at low p_T to $\sim 100\%$ when $p_T > 60$ GeV. The longitudinal impact parameter cut efficiency increases from $\sim 98\%$ at low p_T to $\sim 100\%$ when $p_T > 15$ GeV. The cut efficiencies for muon are much higher than the electron case because the same muon identification is used for the baseline and the signal muon definitions. The associated efficiencies computed using $Z \rightarrow \mu\mu$ events increase from $\sim 80\%$ for $10 < p_T < 15$ GeV to $\sim 98\%$ when $p_T > 50$ GeV. The dominant contribution is the track isolation cut efficiency which increases from $\sim 82\%$ to 98% when $p_T > 50$ GeV. The transverse and longitudinal impact parameter cut efficiencies are $\sim 99\%$ and 100% , respectively. For the electron case, the transverse impact parameter cut is already applied at the baseline level

E.4 Real lepton efficiencies

The real lepton efficiencies as a function of p_T and $|\eta|$ are shown in Fig E.5 where the background subtraction has been applied on the electron case in $10 < p_T < 15$ GeV and $15 < p_T < 20$ GeV. The uncertainties are the quadratic sum of the statistical uncertainties and the measurement systematic uncertainties. The 3 $|\eta|$ binnings for the electron case are driven by the geometry of ECAL. The crack region, $1.37 < |\eta| < 1.52$, is removed from the real electron efficiency study. It is expected that the electron efficiencies in $1.52 < |\eta| < 2.01$ are lower because the electron identification is better in the central region of the ECAL.

E.4.1 Tag-and-probe method and truth matching comparisons

The truth matched information in the $Z \rightarrow \ell\ell$ MC samples are used to verify the accuracy of Z tag-and-probe method. Figure E.6 shows the real lepton efficiencies as a function of p_T , $|\eta|$, and $\Delta R(\ell, \text{jet})$ using Z tag-and-probe method and truth matching. The associated uncertainties are statistical uncertainties only. For the real electron efficiencies, the largest difference is $\sim 7\%$ in low p_T and no differences can be seen when $p_T > 50$ GeV; the largest difference is $\sim 3\%$ in ; the larger differences in $\Delta R(e, \text{jet})$ exist when $\Delta R(e, \text{jet}) < 0.4$. Because the overlap removal has been applied on the baseline electrons, the $\Delta R(e, \text{jet}) < 0.4$ region lacks statistics. For the real muon efficiencies, the differences are less than 1% for p_T and $|\eta|$. However, the differences are larger for $\Delta R(\mu, \text{jet}) < 0.4$ also because of the overlap removal. The small differences between two methods indicate the robust of Z tag-and-probe method and the differences may be considered as the systematic uncertainties.

E.4.2 Data-to-MC comparisons

The real lepton efficiencies calculating by data and $Z \rightarrow \ell\ell$ MC samples are compared. All 2015 and 2016 data are considered corresponding to an integrated luminosity of 36.5 fb^{-1} . All the lepton scale factors are applied on the MC samples and the simulation is reweighted to the pile-up observed in data. Figure E.7 shows the real efficiencies as a function of p_T , $|\eta|$ and $\Delta R(\ell, \text{jet})$ using data and $Z \rightarrow \ell\ell$ MC samples, respectively. The associated uncertainties are statistical uncertainties only. Good agreement between data and MC can be seen in the p_T and $|\eta|$ plots. Larger differences exist in $\Delta R(\ell, \text{jet})$ plots because of lacking statistics.

E.4.3 Real lepton efficiency versus pileup

The relations between the real lepton efficiencies and the pile-up are also studied. The efficiencies computed by 2015 + 2016 data, Z tag-and-probe method and truth matching MC samples are shown in Fig. E.8. In order to study the efficiencies with different event topologies, the $t\bar{t}$ and $\tilde{g} \rightarrow t\bar{t}\widetilde{\chi}_1^0$ MC samples are considered. The real electron efficiencies are $\sim 92\%$ at low $<\mu>$ and decrease when $<\mu>$ increases. The measured real lepton efficiencies using $\tilde{g} \rightarrow t\bar{t}\widetilde{\chi}_1^0$ MC sample is lower than the data case. The $t\bar{t}$ and data have similar real electron efficiencies. However, the real muon efficiencies for $t\bar{t}$ is lower than the data because the efficiencies in $p_T < 40$ GeV is lower. If a $p_T > 40$ GeV requirement is applied on the $t\bar{t}$ MC sample, then the efficiencies are agreed with data. Figure E.9 shows the measured real electron and muon efficiencies as a function of p_T using data, Z tag-and-probe method, truth matching, $t\bar{t}$, and $\tilde{g} \rightarrow t\bar{t}\widetilde{\chi}_1^0$ MC samples. The real lepton efficiencies of $t\bar{t}$ process is lower than the data one in $p_T < 40$ GeV region. The real lepton efficiencies of $\tilde{g} \rightarrow t\bar{t}\widetilde{\chi}_1^0$ process are lower than data in both electron and muon cases.

E.5 Sources of systematic uncertainties

E.5.1 Measurement systematics

The measurement systematic uncertainties of the real lepton efficiency calculated by the Z tag-and-probe method have been studied by varying the background template definitions, the template fitting ranges, and the $m_{\ell\ell}$ windows. The definition of 3 background templates are listed in Table E.2. The additional template fitting ranges are $[60 - 70] \cup [100 - 120]$ GeV and $[65 - 75] \cup [100 - 120]$ GeV. The two other $m_{\ell\ell}$ windows considered are $75 < m_{ee} < 105$ GeV and $85 < m_{ee} < 95$ GeV. Therefore, there are 27 variations

are considered in $p_T < 20$ GeV and 3 variations in $p_T > 20$ GeV for the electron case.

Because the background subtraction is applied on the electron case only, no background templates and template fitting ranges are considered in the muon case. There are only 3 $m_{\ell\ell}$ window variations considered for the systematic uncertainties of real muon efficiency.

Table E.5 and Table E.6 show the measurement uncertainties for the electron and muon cases, respectively.

Electrons (measurement)			
$ \eta $	[0, 0.8]	[0.8, 1.37]	[1.52, 2.0]
$10 < p_T < 15$ GeV	2.32%(t) / 2.85%(f) / 5.06%(m)	4.84%(t) / 1.99%(f) / 5.66%(m)	5.90%(t) / 0.28%(f) / 10.31%(m)
$15 < p_T < 20$ GeV	1.39%(t) / 0.00%(f) / 3.55%(m)	2.01%(t) / 0.01%(f) / 3.94%(m)	2.05%(t) / 0.15%(f) / 6.19%(m)
$20 < p_T < 25$ GeV	2.46%	3.34%	3.88%
$25 < p_T < 30$ GeV	1.69%	2.17%	2.66%
$30 < p_T < 35$ GeV	1.19%	1.75%	2.07%
$35 < p_T < 40$ GeV	0.70%	1.23%	1.32%
$40 < p_T < 50$ GeV	0.20%	0.30%	0.42%
$50 < p_T < 60$ GeV	0.15%	0.17%	0.20%
$60 < p_T < 70$ GeV	0.13%	0.14%	0.21%
$70 < p_T < 80$ GeV	0.10%	0.17%	0.18%
$80 < p_T < 120$ GeV	0.12%	0.11%	0.19%
$120 < p_T < 150$ GeV	0.10%	0.16%	0.06%
$150 < p_T < 200$ GeV	0.11%	0.03%	0.19%

Table E.5: The systematic uncertainties for real electron efficiencies. For the electron case, the background subtraction is applied on the first two p_T bins ($p_T < 20$ GeV). There are 3 sources of the systematic uncertainties: varying templates (t), varying fitting ranges (f), and varying $m_{\ell\ell}$ windows (m). When $p_T > 20$ GeV, only $m_{\ell\ell}$ window variation is considered.

Since electrons extracted from the $m_{\ell\ell}$ tail region are affected by bremsstrahlung effects, the contribution of the $m_{\ell\ell}$ window variations is larger in the systematic uncertainties. Using larger $m_{\ell\ell}$ window, the lower real electron efficiency we get. In $10 < p_T < 15$ GeV,

$ \eta $	Muon (measurement)			
	[0, 0.6]	[0.6, 1.2]	[1.2, 1.8]	[1.8, 2.5]
$10 < p_T < 15 \text{ GeV}$	1.29%	1.06%	0.96%	0.98%
$15 < p_T < 20 \text{ GeV}$	0.44%	0.38%	0.56%	0.64%
$20 < p_T < 25 \text{ GeV}$	0.19%	0.22%	0.38%	0.56%
$25 < p_T < 30 \text{ GeV}$	0.09%	0.12%	0.22%	0.36%
$30 < p_T < 35 \text{ GeV}$	0.06%	0.11%	0.23%	0.32%
$35 < p_T < 40 \text{ GeV}$	0.05%	0.07%	0.13%	0.26%
$40 < p_T < 50 \text{ GeV}$	0.04%	0.04%	0.05%	0.07%
$50 < p_T < 60 \text{ GeV}$	0.06%	0.06%	0.09%	0.07%
$60 < p_T < 70 \text{ GeV}$	0.06%	0.07%	0.08%	0.08%
$70 < p_T < 80 \text{ GeV}$	0.06%	0.08%	0.11%	0.05%
$80 < p_T < 120 \text{ GeV}$	0.07%	0.07%	0.12%	0.07%
$120 < p_T < 150 \text{ GeV}$	0.06%	0.06%	0.15%	0.05%
$150 < p_T < 200 \text{ GeV}$	0.09%	0.11%	0.15%	0.06%

Table E.6: The systematic uncertainties for real muon efficiencies. Only the $m_{\ell\ell}$ window variation is considered because no background subtraction is applied on the muon case.

the contribution comes from the $m_{\ell\ell}$ window variation is $\sim 10\%$ wherease the background subtraction one is $\sim 6\%$. This result shows the robustness of the background subtraction method.

E.5.2 Trigger bias

The systematic uncertainties originate from different trigger strategies are also studied. The leptons entering in the signal regions are required to fire one of the di-lepton triggers. If the event fires the di-lepton trigger and the considered lepton is the leading lepton or the sub-leading lepton, then a trigger matching should be applied before the real lepton efficiency measurement. However, if the event fires the E_T^{miss} trigger or the considered lepton is the third leading lepton, then no trigger matching should be applied. The

systematics uncertainties of are then assigned as the differences between the nominal values and the values measured with different trigger where the nominal value is obtained using events triggered by the single lepton triggers as listed in Table E.1. In order to provide unbiased probe leptons for the real lepton efficiency measurements, the tag lepton must match single lepton trigger. Moreover, the p_T of the two leading leptons must satisfies $p_T > 20$ GeV, the leptons with $p_T < 20$ GeV will never be trigger matched to the di-lepton trigger. Hence, no systematics are assigned in the region $10 < p_T < 20$ GeV. The real electron efficiencies as a function of p_T in 3 $|\eta|$ regions using different trigger strategies are shown in Fig. E.10. The crack region, $1.37 < |\eta| < 1.52$, is removed from the study.

The real muon efficiencies as a function of p_T in 4 $|\eta|$ regions using different trigger strategies are shown in Fig. E.11. These plots indicate that the trigger strategy does not affect the real muon efficiency measurement.

Table E.7 and Table E.8 show the systematic uncertainties due to the different trigger stratagies.

E.5.3 Extrapolation to signal regions

Because $Z \rightarrow \ell\ell$ events are characterized by well isolated leptons, the leptons presented in the final state are not necessary well isolated using different processes. The processes other than $Z \rightarrow \ell\ell$ might contain many (b -)jets in the SR and with different event topologies. In order to study different event topoloties, a SUSY benchmark model $\tilde{g} \rightarrow t\bar{t}\tilde{\chi}_1^0$ is used and $\Delta m = m_{\tilde{g}} - m_{\tilde{\chi}_1^0} > 1$ TeV requirement is applied on the model to selected boosted event. Since one of the main irreducible background, $t\bar{t}V$, has similar event topology, the $t\bar{t}$ samples are also consdered. The difference in the real lepton efficiencies between

Electrons (trigger)			
$ \eta $	[0, 0.8]	[0.8, 1.37]	[1.52, 2.0]
$10 < p_T < 15 \text{ GeV}$	2.46%	1.32%	3.02%
$15 < p_T < 20 \text{ GeV}$	0.16%	0.78%	1.33%
$20 < p_T < 25 \text{ GeV}$	0.29%	0.84%	1.18%
$25 < p_T < 30 \text{ GeV}$	1.53%	2.07%	2.20%
$30 < p_T < 35 \text{ GeV}$	1.28%	1.63%	1.81%
$35 < p_T < 40 \text{ GeV}$	0.98%	1.19%	1.42%
$40 < p_T < 50 \text{ GeV}$	0.73%	0.90%	1.05%
$50 < p_T < 60 \text{ GeV}$	0.68%	0.81%	1.05%
$60 < p_T < 70 \text{ GeV}$	0.61%	0.70%	1.13%
$70 < p_T < 80 \text{ GeV}$	0.65%	0.77%	1.27%
$80 < p_T < 120 \text{ GeV}$	0.60%	0.66%	1.11%
$120 < p_T < 200 \text{ GeV}$	0.38%	0.40%	0.79%
$150 < p_T < 200 \text{ GeV}$	0.43%	0.22%	0.25%

Table E.7: The systematic uncertainties for real electron efficiencies due to the different trigger strategies. The uncertainties of each trigger strategy are calculated with respect to the one applied single lepton trigger with tag trigger matched. The total uncertainties are the quadratic sum of the uncertainties of each trigger strategy.

the two processes are assigned as system uncertainties. Figure E.12 shows the kinematic distributions of the baseline leptons for $Z \rightarrow \ell\ell$, $\tilde{g} \rightarrow t\bar{t}\tilde{\chi}_1^0$, and $t\bar{t}$ processes.

The SUSY process $\tilde{g} \rightarrow t\bar{t}\tilde{\chi}_1^0$ is more boosted and centralized than the $Z \rightarrow \ell\ell$ and $t\bar{t}$ processes. Figure E.13 shows the $\Delta R(\ell, \text{jet})$ and the N_{jets} distributions of the baseline leptons for $Z \rightarrow \ell\ell$, $\tilde{g} \rightarrow t\bar{t}\tilde{\chi}_1^0$, and $t\bar{t}$ processes.

The leptons from the $Z \rightarrow \ell\ell$ processes are not accompanied with a signal jet and the $\Delta R(\ell, \text{jet})$ distribution peak about $\Delta R(\ell, \text{jet}) = 3$. The leptons from the SUSY process $\tilde{g} \rightarrow t\bar{t}\tilde{\chi}_1^0$ peak at $\Delta R(\ell, \text{jet}) = 0.5$ and most of the statistics are located in $\Delta R(\ell, \text{jet}) < 1$ region. The $Z \rightarrow \ell\ell$ peaks at $N_{\text{jets}} = 4$ and $N_{\text{jets}} = 3$ for the electron and

$ \eta $	Muons (trigger)			
	[0, 0.6]	[0.6, 1.2]	[1.2, 1.8]	[1.8, 2.5]
$10 < p_T < 15 \text{ GeV}$	0.11%	0.15%	0.34%	0.19%
$15 < p_T < 20 \text{ GeV}$	0.14%	0.50%	0.75%	0.77%
$20 < p_T < 25 \text{ GeV}$	0.30%	0.63%	1.01%	0.93%
$25 < p_T < 30 \text{ GeV}$	0.90%	1.38%	2.12%	1.83%
$30 < p_T < 35 \text{ GeV}$	0.58%	0.84%	1.27%	0.99%
$35 < p_T < 40 \text{ GeV}$	0.33%	0.37%	0.57%	0.46%
$40 < p_T < 50 \text{ GeV}$	0.16%	0.13%	0.16%	0.13%
$50 < p_T < 60 \text{ GeV}$	0.06%	0.06%	0.07%	0.07%
$60 < p_T < 70 \text{ GeV}$	0.04%	0.04%	0.04%	0.04%
$70 < p_T < 80 \text{ GeV}$	0.05%	0.06%	0.04%	0.06%
$80 < p_T < 120 \text{ GeV}$	0.03%	0.03%	0.03%	0.11%
$120 < p_T < 120 \text{ GeV}$	0.05%	0.13%	0.10%	0.08%
$150 < p_T < 200 \text{ GeV}$	0.04%	0.03%	0.02%	0.19%

Table E.8: The systematic uncertainties for real muon efficiencies due to the different trigger strategies. The uncertainties of each trigger strategy are calculated with respect to the one applied single lepton trigger with tag trigger matched. The total uncertainties are the quadratic sum of the uncertainties of each trigger strategy.

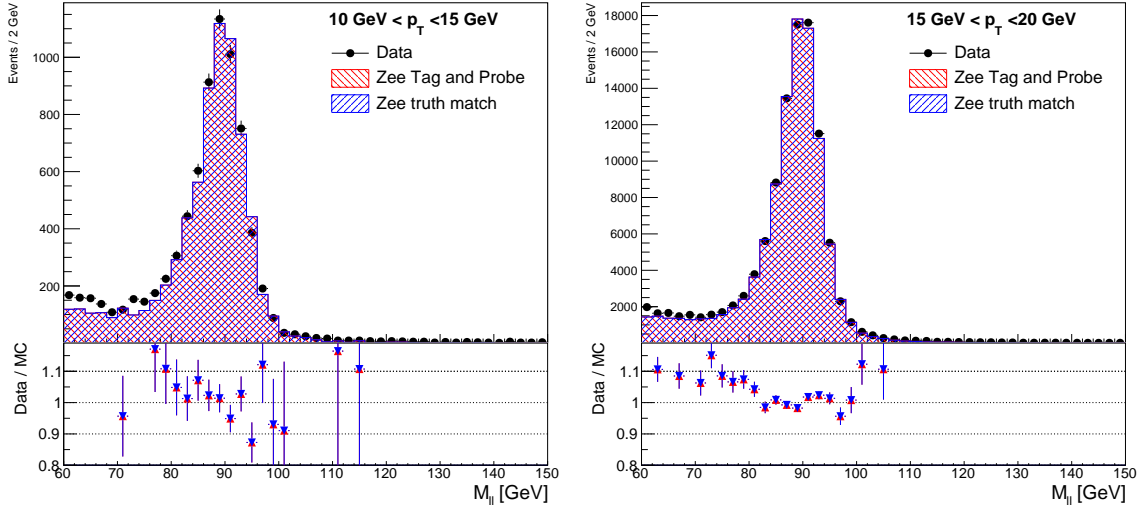
muon case, respectively. The SUSY process $\tilde{g} \rightarrow t\bar{t}\tilde{\chi}_1^0$ peaks at $N_{\text{jets}} = 9$. Hence, the leptons produced in the SUSY process are accompanied with many jets and less isolated than the $Z \rightarrow \ell\ell$ process. If the isolation requirement is looser, then the associated real lepton efficiencies are larger. This extreme topology enables us to assess a conservative SUSY signal extrapolation systematic uncertainty that should cover all SUSY signal processes considered by the analysis.

Figure E.9 shows the real lepton efficiencies as a function of p_T using $Z \rightarrow \ell\ell$, $\tilde{g} \rightarrow t\bar{t}\tilde{\chi}_1^0$, and $t\bar{t}$ processes and the ratio with respect to the data is shown in the lower panel. The real electron efficiencies are p_T dependent when $p_T < 50 \text{ GeV}$ and become stable when

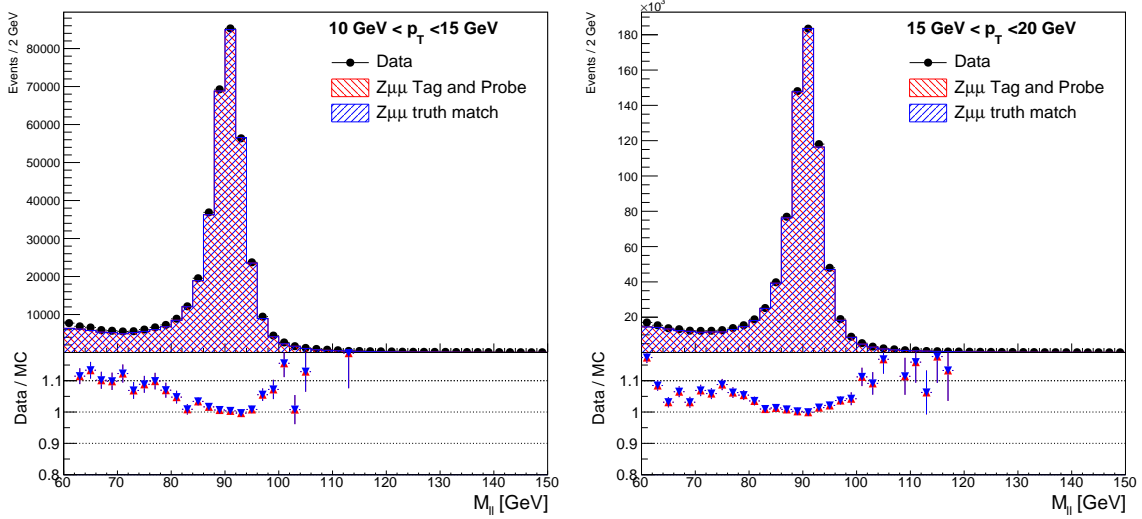
$p_T > 50$ GeV. The real electron efficiencies of $\tilde{g} \rightarrow t\bar{t}\tilde{\chi}_1^0$ are $\sim 8\%$ lower than the efficiencies of $Z \rightarrow ee$. The observed differences in the low p_T region are mostly due to the calorimeter isolation and the track isolation requirements. The differences in the real muon efficiencies mainly come from the track isolation and d_0/σ_{d_0} requirements. The average efficiencies of $Z \rightarrow \ell\ell$ are computed and the relative efficiency differences are calculated with respect to the average efficiencies. Table E.9 shows the relative efficiency differences as a function of $\Delta R(\ell, jet)$ in p_T bins.

E.5.4 Final uncertainties

The final uncertainties are the quadratic sum of the statistical uncertainties and the systematic uncertainties. The sources of systematic uncertainty include the measurement uncertainty, the trigger uncertainty, the uncertainty comes from the differences between Z tag-and-probe method and truth matching, and the uncertainty in the busy environment. Table E.9 shows the uncertainty in the busy environment. The uncertainty in the busy environment is measured as a function of p_T and ΔR so it doesn't combine with the other uncertainties which are function of p_T and $|\eta|$. Table E.10 and Table E.11 show the final uncertainties for electron and muon real efficiencies, respectively.

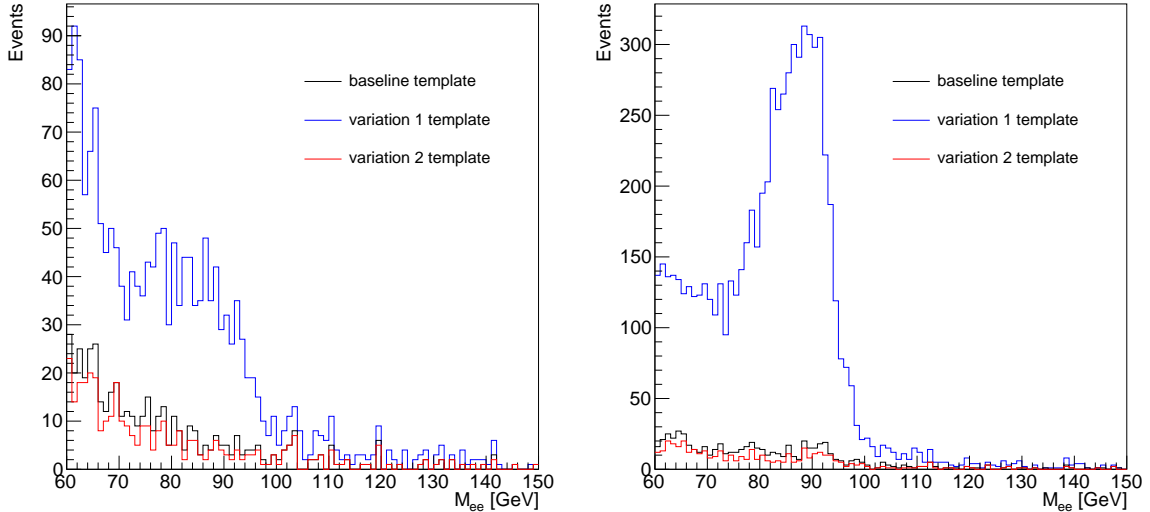


(a) The m_{ee} distribution with $10 < p_T <$
15 GeV. (b) The m_{ee} distribution with $15 < p_T <$
20 GeV.



(c) The $m_{\mu\mu}$ distribution with $10 < p_T <$
15 GeV. (d) The $m_{\mu\mu}$ distribution with $15 < p_T <$
20 GeV.

Figure E.1: The invariant mass distributions of the tag-and-probe pair computed using $Z + jets$ MC and 2015 + 2016 data. The red color stands for the Z tag-and-probe events, the blue color represents the Z truth matched events, and the black dots are data. The MC distributions are scaled to the data using a Gaussian fit of the Z mass peak $85 < m_{\ell\ell} < 95$ GeV.



(a) Probe electrons with $10 < p_T < 15$ GeV. (b) Probe electrons with $15 < p_T < 20$ GeV.

Figure E.2: The m_{ee} distributions for the baseline, variation 1 and variation 2 background templates. The m_{ee} distributions are computed using the probe electrons with different p_T as indicated in the caption of plots. The variation 1 template has looser calorimeter and track isolation requirements and the baseline and the variation 2 templates have tighter selection criteria. So a peak can be seen in the Z mass region in variation 1 template but not in the baseline and variation 2 templates.

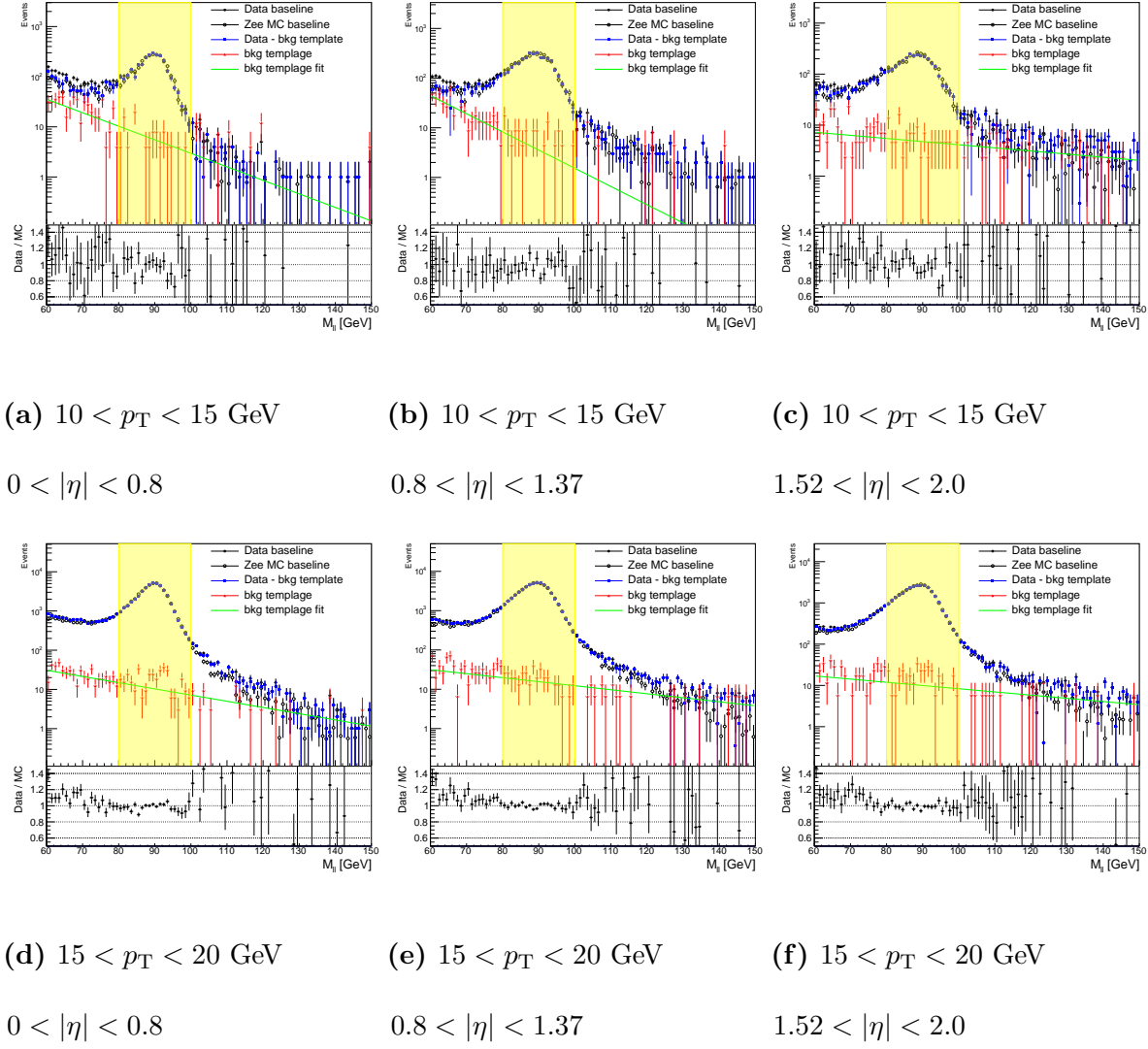


Figure E.3: Illustration of the background subtraction procedure. The full black dots and blue squares are the m_{ee} distributions for data before and after performing the background subtraction, respectively. The m_{ee} distribution for $Z \rightarrow ee$ MC, which is labeled by the open black circles, is normalized to the data after the background subtraction using a Gaussian fit of $85 < m_{ee} < 95$ GeV. The lower panels show the data-to-MC ratio where the background subtraction has been applied on data. The background templates and their respective fitting results are indicated by the red triangles and green lines, respectively.

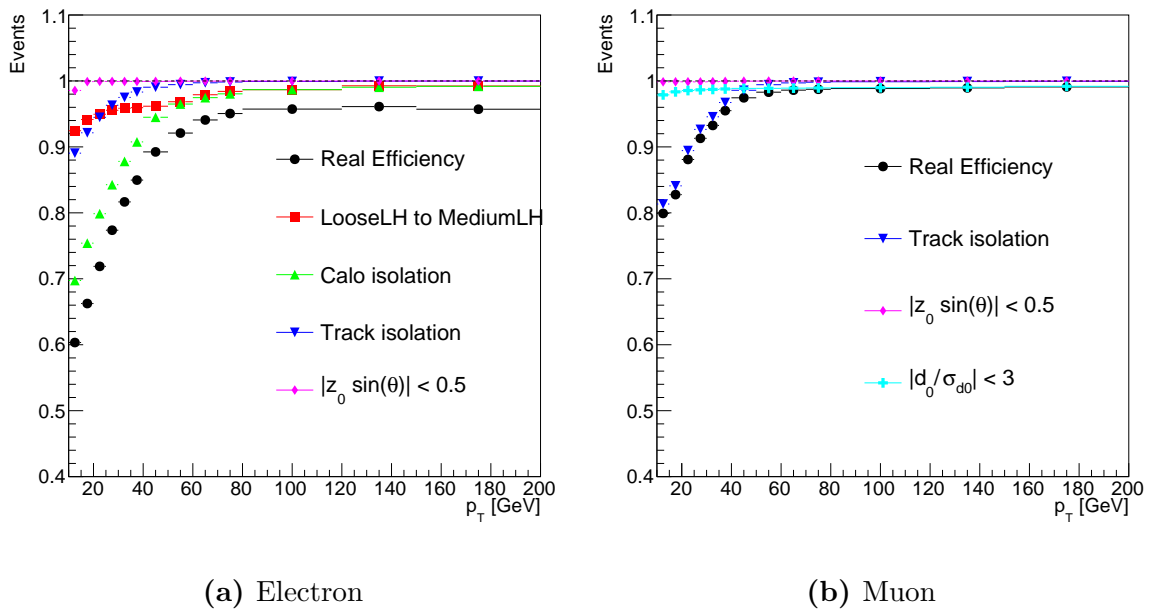


Figure E.4: Cut efficiencies of the signal electron and muon definition as a function of p_T . The total real electron and muon efficiencies are presented by black points. The loose to medium likelihood cut efficiency is presented by red squares. The calorimeter and track isolation cut efficiencies are presented by green triangles and blue triangles, respectively. The longitudinal and transverse impact parameters cut efficiencies are presented by magenta diamonds and cyan crosses, respectively.

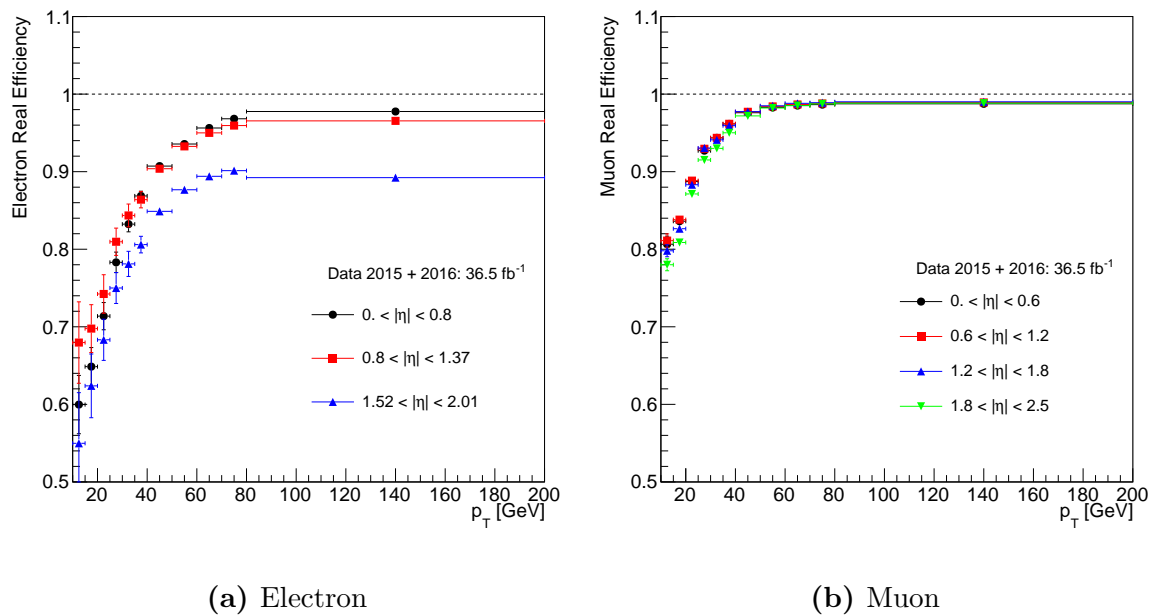


Figure E.5: The real lepton efficiencies as a function of p_T and $|\eta|$ measured using the Z tag-and-probe method. For the real electron efficiencies measurement, the $|\eta|$ binning in the creak region is removed. A homogeneous $|\eta|$ binnings are used for the muon case.

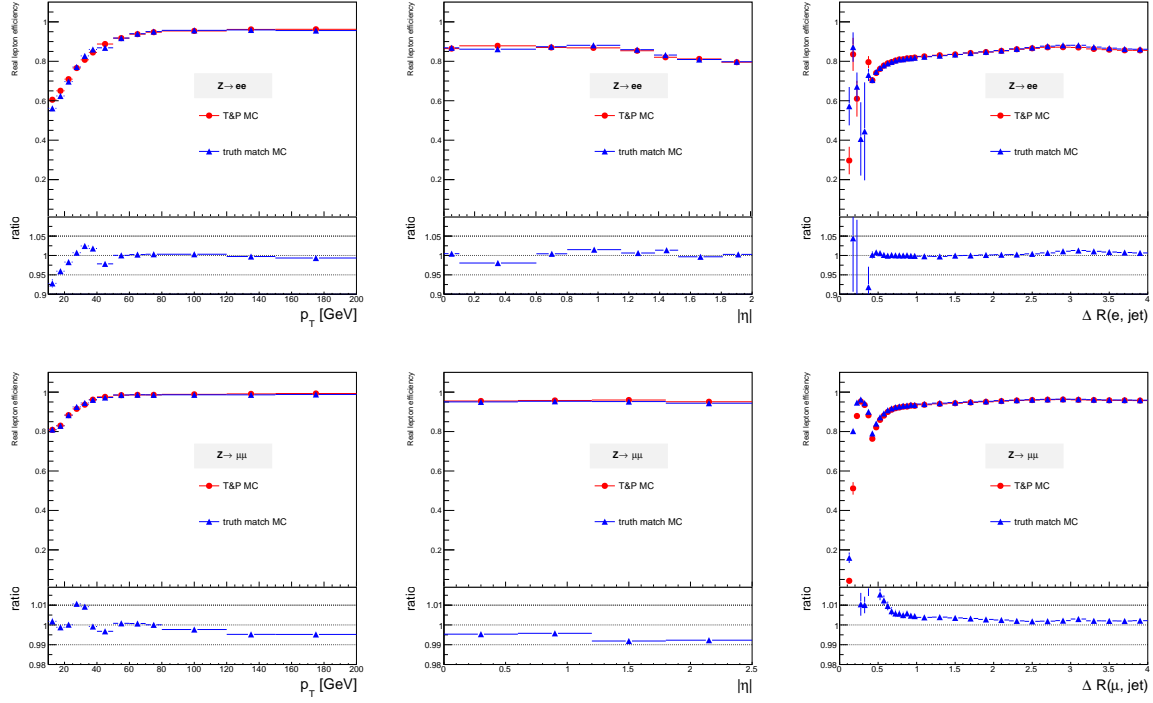


Figure E.6: The real lepton efficiencies computed by Z tag-and-probe method (red dots) and truth matching (blue triangles). The electron cases are on the top row and muon cases are at the bottom row. The three columns from the left to the right are the real lepton efficiencies as a function p_T , $|\eta|$, and $\Delta R(\ell, \text{jet})$, respectively. The lower pads show the ratio with respect to the Z tag-and-probe method.

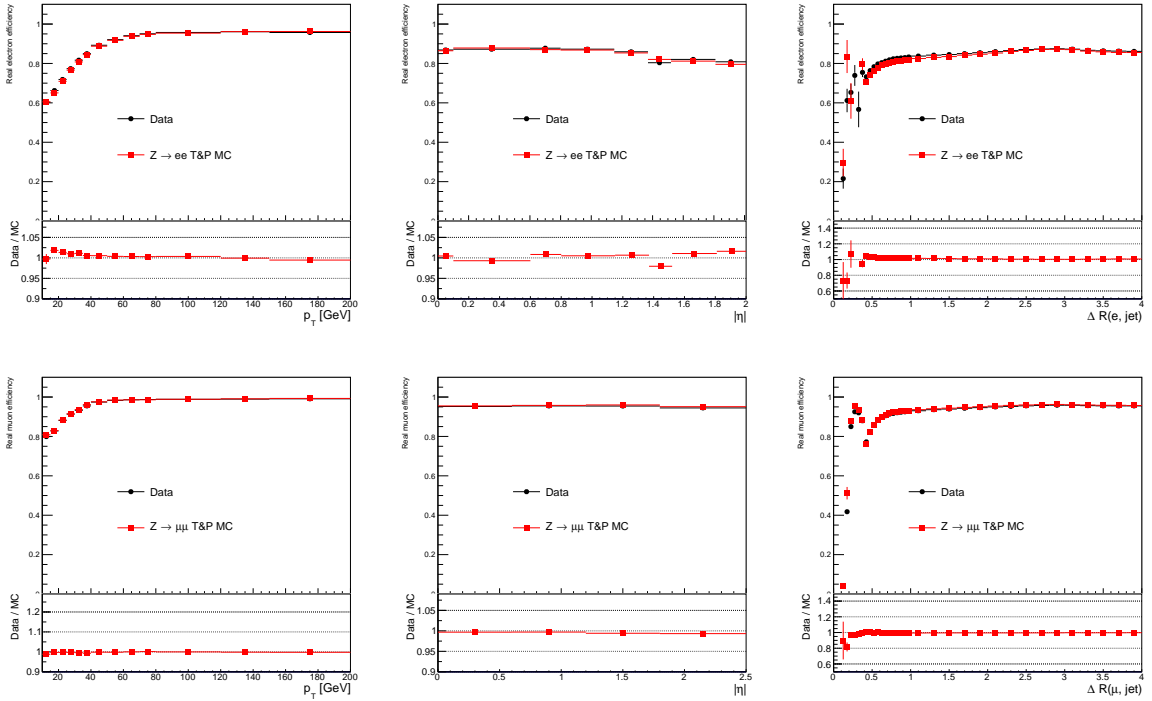


Figure E.7: The real lepton efficiencies measured on 2015 + 2016 data (black dots) and $Z \rightarrow \ell\ell$ MC samples (red squares) using the Z tag-and-probe method. The electron cases are on the top row and muon cases are at the bottom row. The three columns from the left to the right are the real lepton efficiencies as a function p_T , $|\eta|$, and $\Delta R(\ell, \text{jet})$, respectively. The MC samples have been reweighted to the pile-up observed in data.

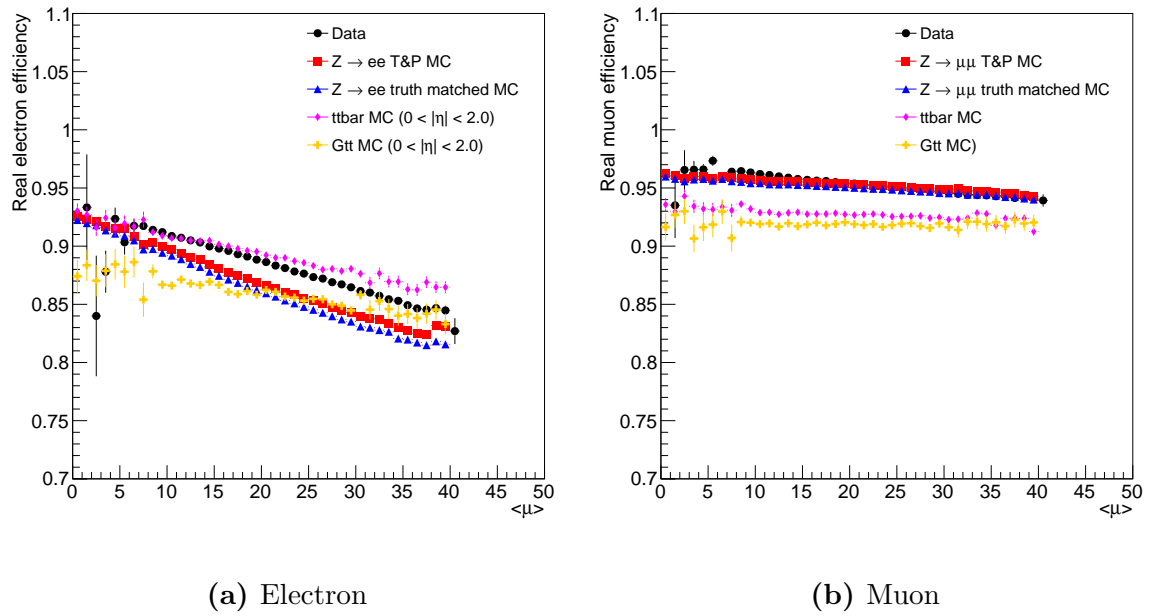


Figure E.8: The real lepton efficiencies as a function of the average interactions per crossing $\langle \mu \rangle$. The data is presented in black dots, $Z \rightarrow \ell\ell$ tag-and-probe is presented in red squares, the truth matching is presented in blue triangles, the $t\bar{t}$ is presented in magenta diamonds, and $\tilde{g} \rightarrow t\bar{t}\widetilde{\chi}_1^0$ is presented in yellow crosses. The $|\eta| < 2$ requirement has been applied on the $t\bar{t}$ and $\tilde{g} \rightarrow t\bar{t}\widetilde{\chi}_1^0$ MC samples for the electron case.

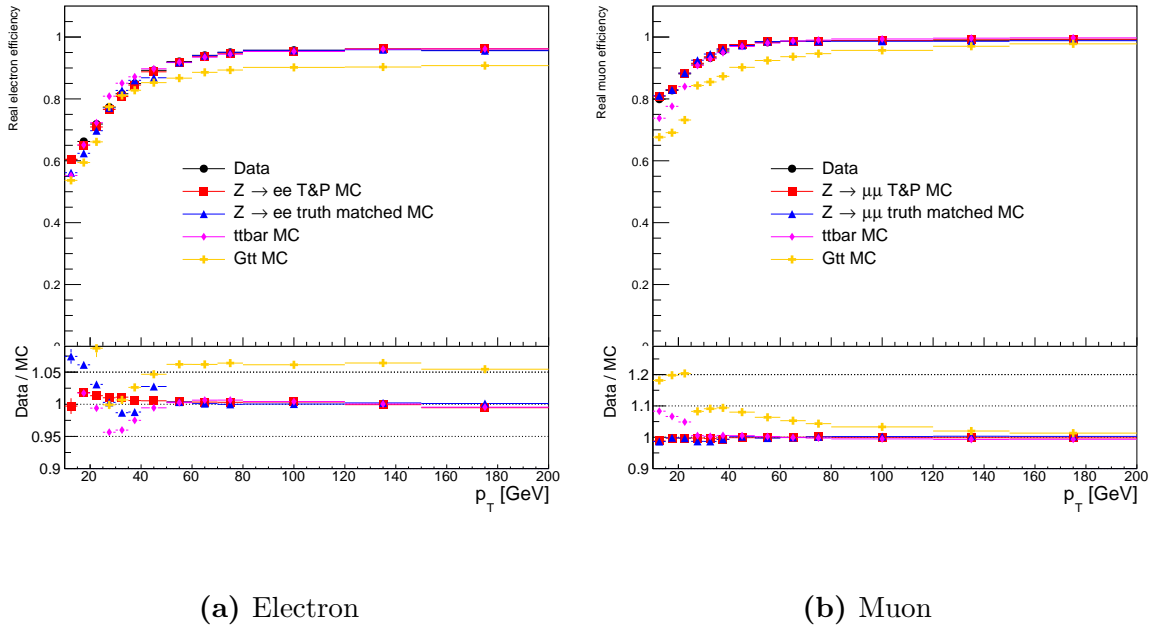


Figure E.9: The real electron and muon efficiencies as a function of p_T . The data is presented in black dots, $Z \rightarrow \ell\ell$ tag-and-probe is presented in red squares, the truth matching is presented in blue triangles, the $t\bar{t}$ is presented in magenta diamonds, and $\tilde{g} \rightarrow t\bar{t}\chi_1^0$ is presented in yellow crosses. The differences in the $p_T < 40$ GeV region come from the different event topologies.

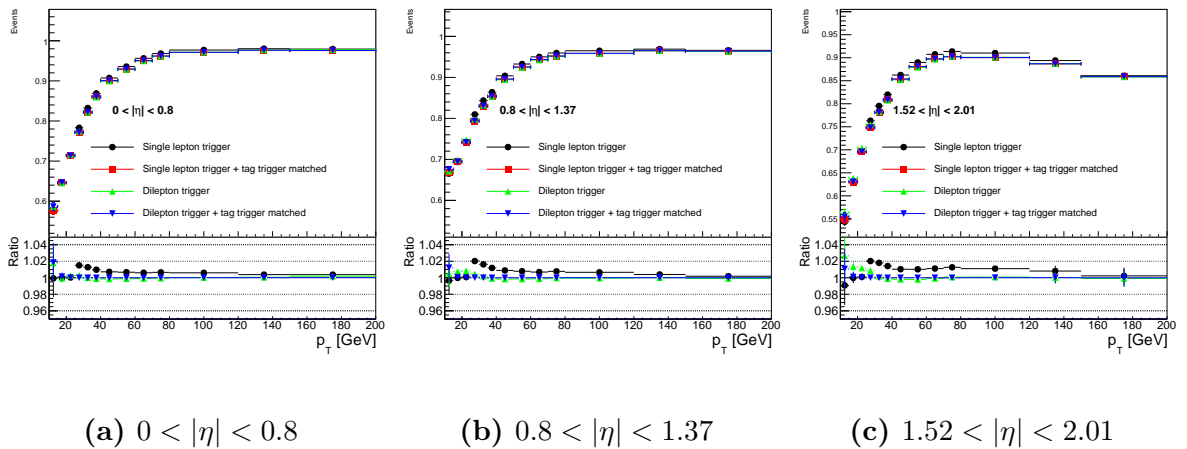


Figure E.10: The real electron efficiencies as a function of p_T in 3 $|\eta|$ regions. Four different trigger strategies are applied. The nominal values are obtained using the single lepton trigger with tag trigger matched. The differences between the nominal values and the values measured using other strategies are assigned as the systematic uncertainties.

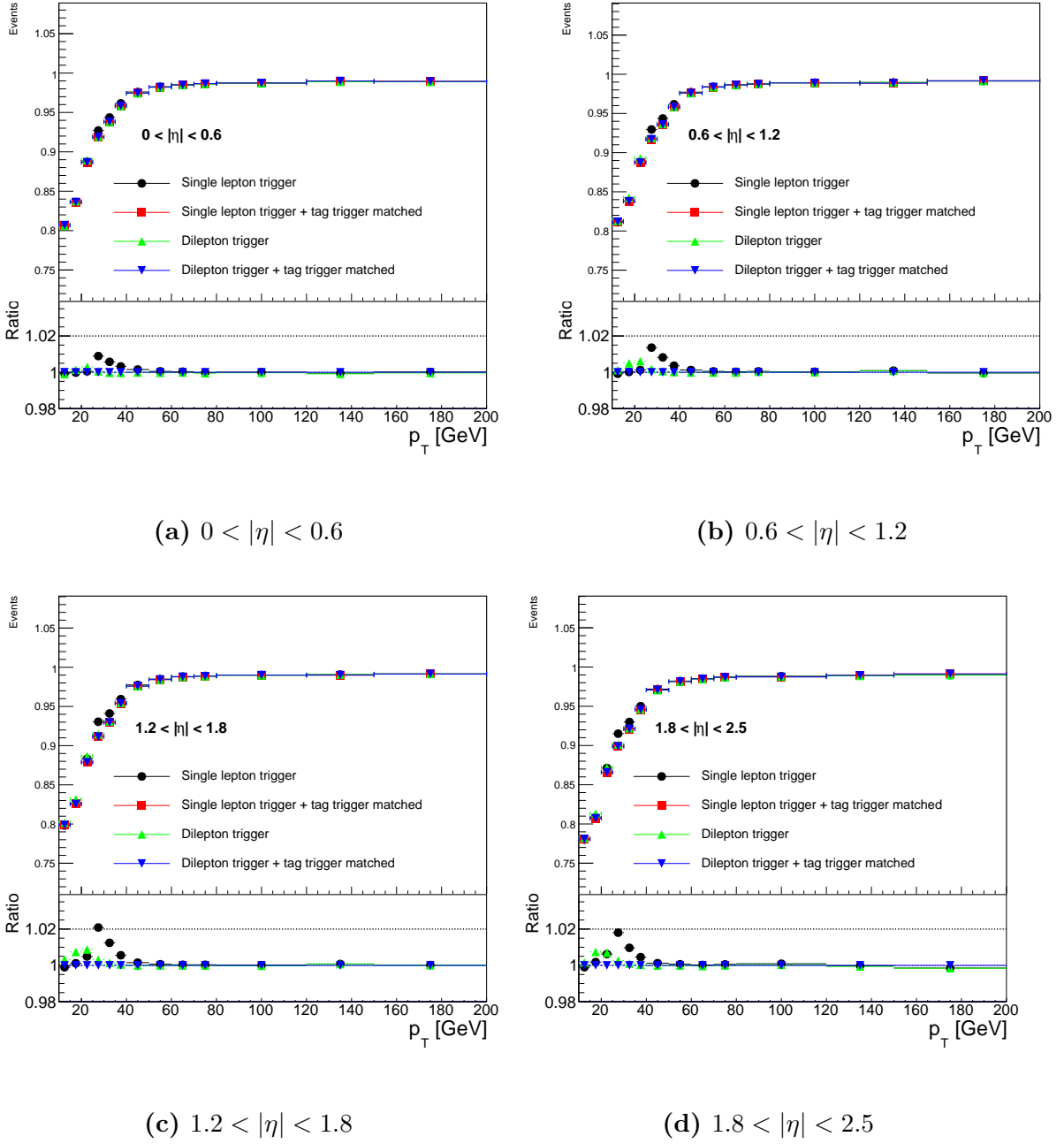


Figure E.11: The real muon efficiencies as a function of p_T in 4 $|\eta|$ regions. Four different trigger strategies are applied. The nominal values are obtained using the single lepton trigger with tag trigger matched. The differences between the nominal values and the values measured using other strategies are assigned as the systematic uncertainties.

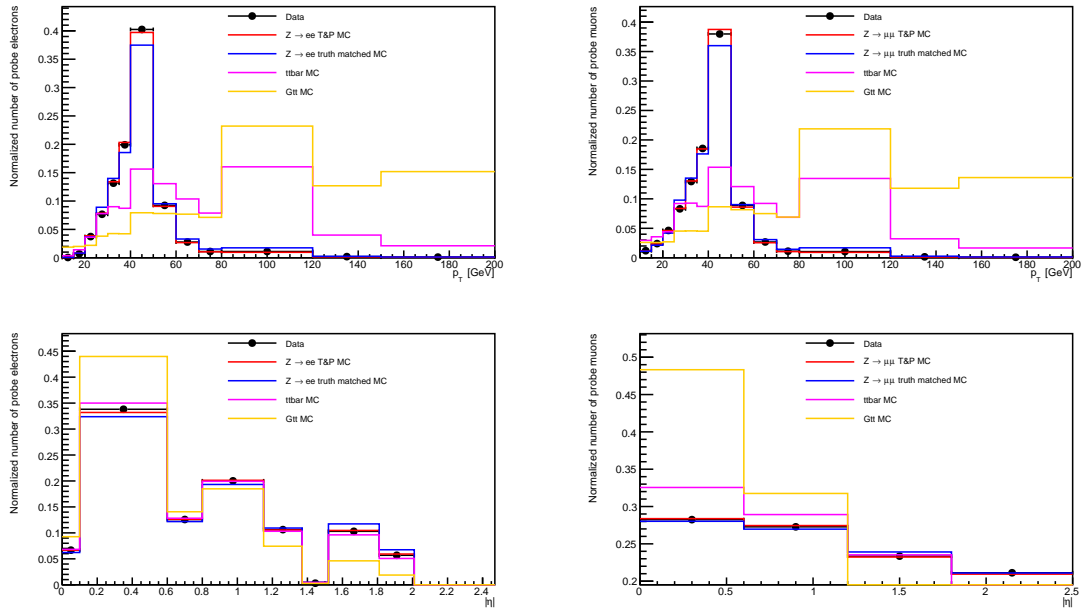


Figure E.12: The kinematic distributions of the baseline leptons for $Z \rightarrow \ell\ell$, $\tilde{g} \rightarrow t\bar{t}\tilde{\chi}_1^0$, and $t\bar{t}$ processes. The top row is the p_T distributions and the bottom row is the $|\eta|$ distributions. The electron case is on the left hand side and the muon case is on the right hand side. The $\tilde{g} \rightarrow t\bar{t}\tilde{\chi}_1^0$ process is more boosted and centralized than the $Z \rightarrow \ell\ell$ and $t\bar{t}$ processes.

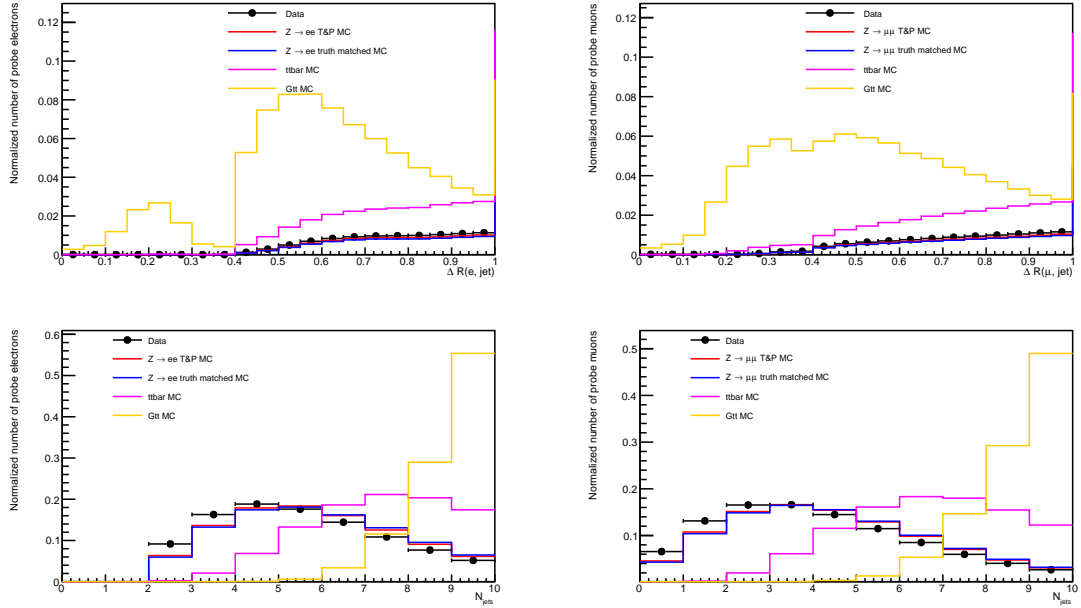


Figure E.13: The $\Delta R(\ell, \text{jet})$ and the N_{jets} distributions of the baseline leptons for $Z \rightarrow \ell\ell$, $\tilde{g} \rightarrow t\bar{t}\tilde{\chi}_1^0$, and $t\bar{t}$ processes. The top row is the $\Delta R(\ell, \text{jet})$ distributions and the bottom row is the N_{jets} distributions. The electron case is on the left hand side and the muon case is on the right hand side. The statistics of $Z \rightarrow \ell\ell$ processes are populated at higher $\Delta R(\ell, \text{jet}) < 1$ region and lower N_{jets} region. The statistics of $\tilde{g} \rightarrow t\bar{t}\tilde{\chi}_1^0$ are located in $\Delta R(\ell, \text{jet}) < 1$ region and higher N_{jets} region.

electrons (busy environments)								
$\Delta R(e, \text{jet})$	[0, 0.1]	[0.1, 0.15]	[0.15, 0.2]	[0.2, 0.3]	[0.3, 0.35]	[0.35, 0.4]	[0.4, 0.6]	[0.6, 4]
$10 < p_T < 20 \text{ GeV}$	-	-	-	-	-	-	25.31%	6.5%
$20 < p_T < 30 \text{ GeV}$	-	-	-	-	-	-	73.37%	10.21%
$30 < p_T < 40 \text{ GeV}$	-	-	-	97.71%	48.22%	15.54%	7.29%	0.58%
$40 < p_T < 50 \text{ GeV}$	-	-	-	52.81%	22.80%	16.73%	7.68%	1.10%
$50 < p_T < 60 \text{ GeV}$	-	-	-	29.96%	21.49%	20.23%	6.99%	2.78%
$60 < p_T < 80 \text{ GeV}$	-	-	55.89%	24.31%	17.40%	24.77%	6.20%	2.87%
$80 < p_T < 150 \text{ GeV}$	-	57.52%	30.24%	16.45%	12.73%	20.92%	4.44%	2.73%
$150 < p_T < 200 \text{ GeV}$	88.54%	40.16%	19.34%	8.45%	14.66%	16.57%	2.57%	1.90%

muons (busy environments)								
$\Delta R(\mu, \text{jet})$	[0, 0.1]	[0.1, 0.15]	[0.15, 0.2]	[0.2, 0.3]	[0.3, 0.35]	[0.35, 0.4]	[0.4, 0.6]	[0.6, 4]
$10 < p_T < 20 \text{ GeV}$	-	-	-	-	-	-	33.59%	5.18%
$20 < p_T < 30 \text{ GeV}$	-	-	-	-	-	-	82.34%	22.27%
$30 < p_T < 40 \text{ GeV}$	-	-	-	98.54%	56.36%	31.89%	14.22%	2.24%
$40 < p_T < 50 \text{ GeV}$	-	-	-	53.10%	21.33%	13.90%	6.81%	1.45%
$50 < p_T < 60 \text{ GeV}$	-	-	-	24.98%	13.72%	9.62%	3.83%	0.79%
$60 < p_T < 80 \text{ GeV}$	-	-	44.41%	13.75%	6.14%	4.76%	2.04%	0.15%
$80 < p_T < 150 \text{ GeV}$	-	29.94%	7.14%	3.16%	1.30%	1.04%	0.07%	0.57%
$150 < p_T < 200 \text{ GeV}$	82.26%	4.14%	1.02%	0.17%	0.29%	0.62%	1.02%	1.13%

Table E.9: The systematic uncertainties of the real lepton efficiency in busy environment using $\tilde{g} \rightarrow t\bar{t}\widetilde{\chi}_1^0$.

Electrons (final uncertainties)			
$ \eta $	[0, 0.8]	[0.8, 1.37]	[1.52, 2.0]
$10 < p_T < 15 \text{ GeV}$	0.047	0.063	0.089
$15 < p_T < 20 \text{ GeV}$	0.027	0.042	0.062
$20 < p_T < 25 \text{ GeV}$	0.018	0.031	0.041
$25 < p_T < 30 \text{ GeV}$	0.029	0.024	0.027
$30 < p_T < 35 \text{ GeV}$	0.023	0.021	0.023
$35 < p_T < 40 \text{ GeV}$	0.014	0.018	0.018
$40 < p_T < 50 \text{ GeV}$	0.007	0.010	0.010
$50 < p_T < 60 \text{ GeV}$	0.008	0.010	0.010
$60 < p_T < 70 \text{ GeV}$	0.007	0.010	0.010
$70 < p_T < 80 \text{ GeV}$	0.008	0.011	0.012
$80 < p_T < 120 \text{ GeV}$	0.010	0.010	0.011
$120 < p_T < 200 \text{ GeV}$	0.005	0.005	0.011
$150 < p_T < 200 \text{ GeV}$	0.005	0.003	0.020

Table E.10: The final uncertainties of the real electron efficiencies. TThe final uncertainties are the quadratic sum of the statistical uncertainties and the systematic uncertainties. The systematic uncertainties include the measurement uncertainty, the trigger uncertainty, the uncertainty comes from the differences between Z tag-and-probe method and truth matching. The uncertainties in the busy environment do not incorporate in the final uncertainties calculation because it is measured as a function of p_T and ΔR . The trigger uncertainties are measured using $p_T > 20 \text{ GeV}$ only.

$ \eta $	Muons (final uncertainties)			
	[0, 0.6]	[0.6, 1.2]	[1.2, 1.8]	[1.8, 2.5]
$10 < p_T < 15 \text{ GeV}$	0.014	0.010	0.008	0.011
$15 < p_T < 20 \text{ GeV}$	0.005	0.006	0.008	0.011
$20 < p_T < 25 \text{ GeV}$	0.003	0.006	0.010	0.010
$25 < p_T < 30 \text{ GeV}$	0.011	0.015	0.022	0.019
$30 < p_T < 35 \text{ GeV}$	0.007	0.009	0.014	0.011
$35 < p_T < 40 \text{ GeV}$	0.004	0.004	0.006	0.006
$40 < p_T < 50 \text{ GeV}$	0.002	0.001	0.002	0.001
$50 < p_T < 60 \text{ GeV}$	0.001	0.001	0.001	0.001
$60 < p_T < 70 \text{ GeV}$	0.001	0.001	0.001	0.002
$70 < p_T < 80 \text{ GeV}$	0.002	0.001	0.001	0.002
$80 < p_T < 120 \text{ GeV}$	0.004	0.002	0.002	0.002
$120 < p_T < 200 \text{ GeV}$	0.006	0.005	0.005	0.005
$150 < p_T < 200 \text{ GeV}$	0.005	0.005	0.005	0.006

Table E.11: The final uncertainties of the real muon efficiencies. TThe final uncertainties are the quadratic sum of the statistical uncertainties and the systematic uncertainties. The systematic uncertainties include the measurement uncertainty, the trigger uncertainty, the uncertainty comes from the differences between Z tag-and-probe method and truth matching. The uncertainties in the busy environment do not incorporate in the final uncertainties calculation because it is measured as a function of p_T and ΔR .

References

- [1] Georges Aad et al. Observation of a new particle in the search for the Standard Model Higgs boson with the ATLAS detector at the LHC. *Phys. Lett.*, B716:1–29, 2012. ([document](#)), [1](#), [2.1.5](#), [2.2](#)
- [2] Serguei Chatrchyan et al. Observation of a new boson at a mass of 125 GeV with the CMS experiment at the LHC. *Phys. Lett.*, B716:30–61, 2012. ([document](#)), [1](#), [2.1.5](#), [2.2](#)
- [3] Steven Weinberg. Implications of Dynamical Symmetry Breaking. *Phys. Rev.*, D13:974–996, 1976. [Addendum: Phys. Rev.D19,1277(1979)]. [1](#)
- [4] Eldad Gildener. Gauge Symmetry Hierarchies. *Phys. Rev.*, D14:1667, 1976. [1](#)
- [5] Leonard Susskind. Dynamics of Spontaneous Symmetry Breaking in the Weinberg-Salam Theory. *Phys. Rev.*, D20:2619–2625, 1979. [1](#)
- [6] J. Wess and B. Zumino. A Lagrangian Model Invariant Under Supergauge Transformations. *Phys. Lett.*, 49B:52, 1974. [1](#)
- [7] J. Wess and B. Zumino. Supergauge Transformations in Four-Dimensions. *Nucl. Phys.*, B70:39–50, 1974. [1](#), [3](#)
- [8] Yu. A. Golfand and E. P. Likhtman. Extension of the Algebra of Poincare Group Generators and Violation of p Invariance. *JETP Lett.*, 13:323–326, 1971. [Pisma Zh. Eksp. Teor. Fiz.13,452(1971)]. [1](#)
- [9] Stephen P. Martin. A Supersymmetry primer. 1997. [Adv. Ser. Direct. High Energy Phys.18,1(1998)]. ([document](#)), [1](#), [2.2.1](#), [3](#), [3.1](#)
- [10] Pierre Fayet. Supersymmetry and Weak, Electromagnetic and Strong Interactions. *Phys. Lett.*, 64B:159, 1976. [1](#)
- [11] Pierre Fayet. Spontaneously Broken Supersymmetric Theories of Weak, Electromagnetic and Strong Interactions. *Phys. Lett.*, 69B:489, 1977. [1](#)
- [12] Glennys R. Farrar and Pierre Fayet. Phenomenology of the Production, Decay, and Detection of New Hadronic States Associated with Supersymmetry. *Phys. Lett.*, 76B:575–579, 1978. [1](#)
- [13] Morad Aaboud et al. Dark matter interpretations of ATLAS searches for the electroweak production of supersymmetric particles in $\sqrt{s} = 8$ TeV proton-proton collisions. *JHEP*, 09:175, 2016. ([document](#)), [1](#), [1.1](#), [1](#)

- [14] Riccardo Barbieri and G. F. Giudice. Upper Bounds on Supersymmetric Particle Masses. *Nucl. Phys.*, B306:63–76, 1988. [1](#)
- [15] B. de Carlos and J. A. Casas. One loop analysis of the electroweak breaking in supersymmetric models and the fine tuning problem. *Phys. Lett.*, B309:320–328, 1993. [1](#)
- [16] Lyndon Evans and Philip Bryant. LHC Machine. *JINST*, 3:S08001, 2008. [1](#), [4](#), [4.1](#), [4.2](#)
- [17] Georges Aad et al. Search for direct production of charginos, neutralinos and sleptons in final states with two leptons and missing transverse momentum in pp collisions at $\sqrt{s} = 8$ TeV with the ATLAS detector. *JHEP*, 05:071, 2014. [1](#)
- [18] Georges Aad et al. Search for direct production of charginos and neutralinos in events with three leptons and missing transverse momentum in $\sqrt{s} = 8$ TeV pp collisions with the ATLAS detector. *JHEP*, 04:169, 2014. [1](#)
- [19] Georges Aad et al. Search for the electroweak production of supersymmetric particles in $\sqrt{s}=8$ TeV pp collisions with the ATLAS detector. *Phys. Rev.*, D93(5):052002, 2016. [1](#)
- [20] Vardan Khachatryan et al. Searches for electroweak production of charginos, neutralinos, and sleptons decaying to leptons and W, Z, and Higgs bosons in pp collisions at 8 TeV. *Eur. Phys. J.*, C74(9):3036, 2014. [1](#)
- [21] Vardan Khachatryan et al. Search for supersymmetry in events with soft leptons, low jet multiplicity, and missing transverse energy in protonproton collisions at $\sqrt{s}=8$ TeV. *Phys. Lett.*, B759:9–35, 2016. [1](#)
- [22] Albert M Sirunyan et al. Search for electroweak production of charginos and neutralinos in multilepton final states in proton-proton collisions at $\sqrt{s} = 13$ TeV. 2017. [1](#)
- [23] Abdus Salam. Weak and Electromagnetic Interactions. *Conf. Proc.*, C680519:367–377, 1968. [2](#), [2.1.4](#), [3](#)
- [24] S. L. Glashow. Partial Symmetries of Weak Interactions. *Nucl. Phys.*, 22:579–588, 1961. [2](#), [2.1.4](#), [3](#)
- [25] Steven Weinberg. A Model of Leptons. *Phys. Rev. Lett.*, 19:1264–1266, 1967. [2](#), [2.1.4](#), [3](#)
- [26] M. Herrero. The Standard model. *NATO Sci. Ser. C*, 534:1–59, 1999. [2](#), [3](#)
- [27] W. N. Cottingham and D. A. Greenwood. *An introduction to the standard model of particle physics*. Cambridge University Press, 2007. [2](#), [3](#)
- [28] Emmy Noether. Invariant Variation Problems. *Gott. Nachr.*, 1918:235–257, 1918. [Transp. Theory Statist. Phys.1,186(1971)]. [2.1](#)
- [29] C. Patrignani et al. Review of Particle Physics. *Chin. Phys.*, C40(10):100001, 2016. ([document](#)), [2.1](#), [2.1.1](#)

- [30] E. Fermi. An attempt of a theory of beta radiation. 1. *Z. Phys.*, 88:161–177, 1934. [2.1.4](#)
- [31] T. Nakano and K. Nishijima. Charge Independence for V-particles. *Prog. Theor. Phys.*, 10:581–582, 1953. [2.1.4](#)
- [32] M. Gell-Mann. The interpretation of the new particles as displaced charge multiplets. *Nuovo Cim.*, 4(S2):848–866, 1956. [2.1.4](#)
- [33] Makoto Kobayashi and Toshihide Maskawa. CP Violation in the Renormalizable Theory of Weak Interaction. *Prog. Theor. Phys.*, 49:652–657, 1973. [2.1.4](#)
- [34] Ziro Maki, Masami Nakagawa, and Shoichi Sakata. Remarks on the unified model of elementary particles. *Prog. Theor. Phys.*, 28:870–880, 1962. [2.1.4](#)
- [35] Peter W. Higgs. Spontaneous Symmetry Breakdown without Massless Bosons. *Phys. Rev.*, 145:1156–1163, 1966. [2.1.4](#)
- [36] Peter W. Higgs. Broken Symmetries and the Masses of Gauge Bosons. *Phys. Rev. Lett.*, 13:508–509, 1964. [2.1.4](#)
- [37] Peter W. Higgs. Broken symmetries, massless particles and gauge fields. *Phys. Lett.*, 12:132–133, 1964. [2.1.4](#)
- [38] F. Englert and R. Brout. Broken Symmetry and the Mass of Gauge Vector Mesons. *Phys. Rev. Lett.*, 13:321–323, 1964. [2.1.4](#)
- [39] G. S. Guralnik, C. R. Hagen, and T. W. B. Kibble. Global Conservation Laws and Massless Particles. *Phys. Rev. Lett.*, 13:585–587, 1964. [2.1.4](#)
- [40] John Ellis. Higgs Physics. In *Proceedings, 2013 European School of High-Energy Physics (ESHEP 2013): Paradfurdo, Hungary, June 5-18, 2013*, pages 117–168, 2015. ([document](#)), [2.1](#)
- [41] Piotr H. Chankowski, John R. Ellis, Keith A. Olive, and Stefan Pokorski. Cosmological fine tuning, supersymmetry, and the gauge hierarchy problem. *Phys. Lett.*, B452:28–38, 1999. [2.2.1](#)
- [42] Maarten C. Brak. The hierarchy problem in the standard model and little higgs theories. Oct 2004. [2.2.1](#)
- [43] C. L. Bennett et al. Nine-Year Wilkinson Microwave Anisotropy Probe (WMAP) Observations: Final Maps and Results. *Astrophys. J. Suppl.*, 208:20, 2013. [2.2.2](#)
- [44] P. A. R. Ade et al. Planck 2013 results. I. Overview of products and scientific results. *Astron. Astrophys.*, 571:A1, 2014. [2.2.2](#)
- [45] Gianfranco Bertone, Dan Hooper, and Joseph Silk. Particle dark matter: Evidence, candidates and constraints. *Phys. Rept.*, 405:279–390, 2005. [2.2.2](#)
- [46] The accelerator complex at cern. <https://i.stack.imgur.com/Ur0o1.gif>. ([document](#)), [2.3](#)
- [47] Graham G. Ross. *GRAND UNIFIED THEORIES*. 1985. [2.2.3](#)

- [48] Peter J. Mohr, David B. Newell, and Barry N. Taylor. CODATA Recommended Values of the Fundamental Physical Constants: 2014. *Rev. Mod. Phys.*, 88(3):035009, 2016. [2.2.3](#)
- [49] Joseph D. Lykken. Introduction to supersymmetry. In *Fields, strings and duality. Proceedings, Summer School, Theoretical Advanced Study Institute in Elementary Particle Physics, TASI'96, Boulder, USA, June 2-28, 1996*, pages 85–153, 1996. [3](#)
- [50] Manuel Drees. An Introduction to supersymmetry. In *Current topics in physics. Proceedings, Inauguration Conference of the Asia-Pacific Center for Theoretical Physics (APCTP), Seoul, Korea, June 4-10, 1996. Vol. 1, 2*, 1996. [3](#)
- [51] Adel Bilal. Introduction to supersymmetry. 2001. [3](#)
- [52] Philip C. Argyres. An Introduction to Global Supersymmetry. 2001. [3](#)
- [53] Michael E. Peskin. Supersymmetry in Elementary Particle Physics. In *Proceedings of Theoretical Advanced Study Institute in Elementary Particle Physics : Exploring New Frontiers Using Colliders and Neutrinos (TASI 2006): Boulder, Colorado, June 4-30, 2006*, pages 609–704, 2008. [3](#)
- [54] Ian J. R. Aitchison. Supersymmetry and the MSSM: An Elementary introduction. 2005. [3](#)
- [55] Y. Shadmi. Introduction to Supersymmetry. In *Proceedings, 2014 European School of High-Energy Physics (ESHEP 2014): Garderen, The Netherlands, June 18 - July 01 2014*, pages 95–123, 2016. [3](#)
- [56] Howard Baer, Vernon Barger, Peisi Huang, Dan Mickelson, Azar Mustafayev, Warintorn Sreethawong, and Xerxes Tata. Radiatively-driven natural supersymmetry at the LHC. *JHEP*, 12:013, 2013. [Erratum: JHEP06,053(2015)]. [3.3, 3.4, 5.2.2](#)
- [57] Howard Baer, Vernon Barger, Peisi Huang, Azar Mustafayev, and Xerxes Tata. Radiative natural SUSY with a 125 GeV Higgs boson. *Phys. Rev. Lett.*, 109:161802, 2012. [3.3](#)
- [58] Howard Baer. Radiative natural supersymmetry with mixed axion/higgsino cold dark matter. 2012. [AIP Conf. Proc.1534,39(2012)]. [3.3](#)
- [59] Howard Baer, Vernon Barger, Peisi Huang, Dan Mickelson, Azar Mustafayev, and Xerxes Tata. Radiative natural supersymmetry: Reconciling electroweak fine-tuning and the Higgs boson mass. *Phys. Rev.*, D87(11):115028, 2013. [3.3](#)
- [60] Howard Baer, Vernon Barger, and Dan Mickelson. How conventional measures overestimate electroweak fine-tuning in supersymmetric theory. *Phys. Rev.*, D88(9):095013, 2013. ([document](#)), [3.2](#)
- [61] John R. Ellis, Keith A. Olive, and Yudi Santoso. The MSSM parameter space with nonuniversal Higgs masses. *Phys. Lett.*, B539:107–118, 2002. [3.4](#)
- [62] John R. Ellis, Toby Falk, Keith A. Olive, and Yudi Santoso. Exploration of the MSSM with nonuniversal Higgs masses. *Nucl. Phys.*, B652:259–347, 2003. [3.4](#)

- [63] Howard Baer, Azar Mustafayev, Stefano Profumo, Alexander Belyaev, and Xerxes Tata. Neutralino cold dark matter in a one parameter extension of the minimal supergravity model. *Phys. Rev.*, D71:095008, 2005. [3.4](#)
- [64] Howard Baer, Azar Mustafayev, Stefano Profumo, Alexander Belyaev, and Xerxes Tata. Direct, indirect and collider detection of neutralino dark matter in SUSY models with non-universal Higgs masses. *JHEP*, 07:065, 2005. [3.4](#)
- [65] Howard Baer, Vernon Barger, Michael Savoy, and Xerxes Tata. Multichannel assault on natural supersymmetry at the high luminosity LHC. *Phys. Rev.*, D94(3):035025, 2016. [\(document\)](#), [3.3](#)
- [66] G. Aad et al. The ATLAS Experiment at the CERN Large Hadron Collider. *JINST*, 3:S08003, 2008. [\(document\)](#), [4](#), [4.2](#), [4.2](#), [4.3](#), [4.4](#), [4.2.3](#), [4.1](#), [4.2.4](#), [4.6](#)
- [67] S. Chatrchyan et al. The CMS Experiment at the CERN LHC. *JINST*, 3:S08004, 2008. [4](#)
- [68] K. Aamodt et al. The ALICE experiment at the CERN LHC. *JINST*, 3:S08002, 2008. [4](#)
- [69] A. Augusto Alves, Jr. et al. The LHCb Detector at the LHC. *JINST*, 3:S08005, 2008. [4](#)
- [70] G. Anelli et al. The TOTEM experiment at the CERN Large Hadron Collider. *JINST*, 3:S08007, 2008. [4](#)
- [71] O. Adriani et al. The LHCf detector at the CERN Large Hadron Collider. *JINST*, 3:S08006, 2008. [4](#)
- [72] James Pinfold et al. Technical Design Report of the MoEDAL Experiment. 2009. [4](#)
- [73] Fabienne Marcastel. CERN's Accelerator Complex. La chane des accrateurs du CERN. Oct 2013. General Photo. [\(document\)](#), [4.1](#)
- [74] L. Rossi. The LHC superconducting magnets. *Conf. Proc.*, C030512:141, 2003. [4.1](#)
- [75] Cern courier. <http://cerncourier.com/cws/article/cern/35864>. [4.1](#)
- [76] P. Strizenec. Performance of the ATLAS Liquid Argon Calorimeter after three years of LHC operation and plans for a future upgrade. *JINST*, 9:C09007, 2014. [\(document\)](#), [4.5](#)
- [77] S. Palestini. The muon spectrometer of the ATLAS experiment. *Nucl. Phys. Proc. Suppl.*, 125:337–345, 2003. [337(2003)]. [4.2.4](#)
- [78] E. Diehl. ATLAS Muon Detector Commissioning. In *Particles and fields. Proceedings, Meeting of the Division of the American Physical Society, DPF 2009, Detroit, USA, July 26-31, 2009*, 2009. [4.2.4](#)
- [79] K. Kordas et al. The ATLAS Data Acquisition and Trigger: Concept, design and status. *Nucl. Phys. Proc. Suppl.*, 172:178–182, 2007. [4.2.5](#)

- [80] A. Ruiz Martnez. The Run-2 ATLAS Trigger System. *J. Phys. Conf. Ser.*, 762(1):012003, 2016. ([document](#)), 4.7
- [81] Morad Aaboud et al. Luminosity determination in pp collisions at $\sqrt{s} = 8$ TeV using the ATLAS detector at the LHC. *Eur. Phys. J.*, C76(12):653, 2016. 5.1
- [82] S. Agostinelli et al. GEANT4: A Simulation toolkit. *Nucl. Instrum. Meth.*, A506:250–303, 2003. 5.2, D
- [83] ATLAS Collaboration. The simulation principle and performance of the ATLAS fast calorimeter simulation FastCaloSim. 2010. 5.2, D
- [84] Torbjorn Sjostrand, Stephen Mrenna, and Peter Z. Skands. A Brief Introduction to PYTHIA 8.1. *Comput. Phys. Commun.*, 178:852–867, 2008. 5.2
- [85] Summary of ATLAS Pythia 8 tunes. 2012. 5.2
- [86] A. D. Martin, W. J. Stirling, R. S. Thorne, and G. Watt. Parton distributions for the LHC. *Eur. Phys. J.*, C63:189–285, 2009. 5.2, D.1
- [87] T. Gleisberg, Stefan Hoeche, F. Krauss, M. Schonherr, S. Schumann, F. Siegert, and J. Winter. Event generation with SHERPA 1.1. *JHEP*, 02:007, 2009. 5.2.1
- [88] D. J. Lange. The EvtGen particle decay simulation package. *Nucl. Instrum. Meth.*, A462:152–155, 2001. 5.2.1, D.1
- [89] Howard Baer, Frank E. Paige, Serban D. Protopopescu, and Xerxes Tata. ISAJET 7.48: A Monte Carlo event generator for p p, anti-p, p, and e+ e- reactions. 1999. 5.2.2
- [90] W. Beenakker, M. Klasen, M. Kramer, T. Plehn, M. Spira, and P. M. Zerwas. The Production of charginos / neutralinos and sleptons at hadron colliders. *Phys. Rev. Lett.*, 83:3780–3783, 1999. [Erratum: *Phys. Rev. Lett.* 100, 029901 (2008)]. 5.2.2
- [91] Pierre Artoisenet, Rikkert Frederix, Olivier Mattelaer, and Robbert Rietkerk. Automatic spin-entangled decays of heavy resonances in Monte Carlo simulations. *JHEP*, 03:015, 2013. 5.2.2
- [92] W. Beenakker, R. Hopker, and M. Spira. PROSPINO: A Program for the production of supersymmetric particles in next-to-leading order QCD. 1996. 5.2.2
- [93] A. Djouadi, M. M. Muhlleitner, and M. Spira. Decays of supersymmetric particles: The Program SUSY-HIT (SUspect-SdecaY-Hdecay-InTerface). *Acta Phys. Polon.*, B38:635–644, 2007. 5.2.2
- [94] The susytoolsv8 twiki. <https://twiki.cern.ch/twiki/bin/view/AtlasProtected/SUSYToolsV8>. 6.1
- [95] The analysis release twiki. <https://twiki.cern.ch/twiki/bin/viewauth/AtlasProtected/AnalysisRelease>. 6.1
- [96] The ATLAS collaboration. Electron efficiency measurements with the ATLAS detector using the 2015 LHC proton-proton collision data. 2016. 6.1.1

- [97] Georges Aad et al. Muon reconstruction performance of the ATLAS detector in protonproton collision data at $\sqrt{s} = 13$ TeV. *Eur. Phys. J.*, C76(5):292, 2016. [6.1.2](#)
- [98] The ATLAS collaboration. Measurement of the tau lepton reconstruction and identification performance in the ATLAS experiment using pp collisions at $\sqrt{s} = 13$ TeV. 2017. [6.1.3](#)
- [99] Expected photon performance in the ATLAS experiment. 2011. [6.1.4](#)
- [100] Matteo Cacciari, Gavin P. Salam, and Gregory Soyez. The Anti-k(t) jet clustering algorithm. *JHEP*, 04:063, 2008. [6.1.5](#)
- [101] Expected performance of the ATLAS b -tagging algorithms in Run-2. Technical Report ATL-PHYS-PUB-2015-022, CERN, Geneva, Jul 2015. [6.1.5](#)
- [102] Optimisation of the ATLAS b -tagging performance for the 2016 LHC Run. Technical Report ATL-PHYS-PUB-2016-012, CERN, Geneva, Jun 2016. [6.1.5](#)
- [103] Expected performance of missing transverse momentum reconstruction for the ATLAS detector at $\sqrt{s} = 13$ TeV. Technical Report ATL-PHYS-PUB-2015-023, CERN, Geneva, Jul 2015. [6.1.6](#)
- [104] M. Baak, G. J. Besjes, D. Cte, A. Koutsman, J. Lorenz, and D. Short. HistFitter software framework for statistical data analysis. *Eur. Phys. J.*, C75:153, 2015. ([document](#)), [7.1](#)
- [105] Tagging and suppression of pileup jets with the ATLAS detector. Technical Report ATLAS-CONF-2014-018, CERN, Geneva, May 2014. [E.1](#)